



저작자표시-비영리-변경금지 2.0 대한민국

이용자는 아래의 조건을 따르는 경우에 한하여 자유롭게

- 이 저작물을 복제, 배포, 전송, 전시, 공연 및 방송할 수 있습니다.

다음과 같은 조건을 따라야 합니다:



저작자표시. 귀하는 원저작자를 표시하여야 합니다.



비영리. 귀하는 이 저작물을 영리 목적으로 이용할 수 없습니다.



변경금지. 귀하는 이 저작물을 개작, 변형 또는 가공할 수 없습니다.

- 귀하는, 이 저작물의 재이용이나 배포의 경우, 이 저작물에 적용된 이용허락조건을 명확하게 나타내어야 합니다.
- 저작권자로부터 별도의 허가를 받으면 이러한 조건들은 적용되지 않습니다.

저작권법에 따른 이용자의 권리는 위의 내용에 의하여 영향을 받지 않습니다.

이것은 [이용허락규약\(Legal Code\)](#)을 이해하기 쉽게 요약한 것입니다.

[Disclaimer](#)

**A Study on the Fault Diagnosis Technology and  
Application for Industrial Equipment using Deep  
Learning**

for the Degree of

**Doctor of Philosophy**

(Computer Engineering)

Jaeyoung Kim

Feb. 2021

**A Study on the Fault Diagnosis Technology and  
Application for Industrial Equipment using Deep  
Learning**

**Dissertation**

Submitted in partial fulfillment of the requirements  
for the degree of

**Doctor of Philosophy**  
(Computer Engineering)

at the

**University of Ulsan**

by

**Jaeyoung Kim**



Feb. 2021

Publication No. \_\_\_\_\_

## DECLARATION OF AUTHORSHIP

I, JAEYOUNG KIM, declare that this thesis titled “A Study on the Fault Diagnosis Technology and Application for Industrial Equipment using Deep Learning” and the work presented herein are my own. I confirm that:

- This work was done wholly while in candidature for a research degree at the University of Ulsan.
- Where I have consulted the published work of others, it has always been clearly attributed to its original sources, and I have acknowledged all the sources.
- Where I have quoted from the work of others, the source is always mentioned. Except for such quotations, this thesis is entirely my work.



---

Jaeyoung Kim

UNIVERSITY OF ULSAN

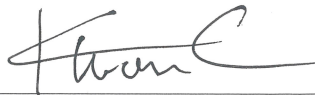
Feb. 2021

©2021 – Jaeyoung Kim

All rights reserved

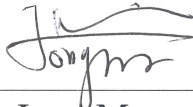
# A Study on the Fault Diagnosis Technology and Application for Industrial Equipment using Deep Learning

Approved by Supervisory Committee:



---

Prof. Kwon, Yung-Keun, Committee Chair



---

Prof. Kim, Jong-Myon, Advisor, Prof.



---

Prof. Yoon, Seok-Hoon, Committee Member



---

Dr. Chung, Hyun-Sang, Committee Member



---

Dr. Kim, Ki-Hong, Committee Member

Department of Electrical, Electronics, and Computer Engineering  
University of Ulsan, Republic of Korea

Date: Feb. 2021

## VITA

**Jaeyoung Kim** did his B.Sc and M.Sc in Computer Engineering from University of Ulsan, 2012 and 2015. His interest in Masters was computer vision. Since March 2015 he has been enrolled in the doctoral program in computer engineering at School of Electrical, Electronics, and Computer Engineering under the supervision of Prof. Jong-Myon Kim. His research interests span over deep-learning, signal processing, and applications for condition monitoring, fault diagnosis and prognosis of industrial equipment.

## ACKNOWLEDGMENTS

Beginning in 2015, I am happy to learn a lot, grow and graduate after completing my six-year PhD. There were many difficult days, but I wouldn't have been able to come this far without the help of adviser Prof. Kim, Jong-Myon and my colleagues in the lab.

A doctorate degree means more than a degree because it has grown my potential and made me realize the appreciation of the people around me. I would like to express my deep gratitude to Prof. Kim Jong-Myon for always leading me and giving me meaningful guidance. I am deeply grateful to Prof. Kwon Young-Keun, Prof. Yoon Seok-Hoon, Dr. Jung Hyun-Sang, and Dr. Kim Gi-Hong, who carefully reviewed my thesis and gave generous advice. In addition, I would like to express my deep gratitude to the late Kang Myung-Soo for actively guiding me at the beginning of my Ph.D. life and providing the driving force to bring me to this point. I would like to express my gratitude to Jeong Inkyu, Son Donkoo, Dr. Im Ki-Chang, Duong Bach Phi, Prosvirin Alexander, Tra Viet, Buy Qui Thang, and the other lab members, who have provided valuable feedback and support to me during my degree. I also would like to express my gratitude to Ms. Ha Jae-Kyung, Ms. Lee Jeong, and Ms. Nam Seung-Ja for supporting me to focus on my research. I am very grateful to my parents, brothers, and my beloved family who trusted and supported me in my way.

Kim Jaeyoung  
Ulsan, Republic of Korea  
January 2021

## 감사의 글

2015년을 시작으로 6년간의 박사 생활을 마치며 많은 것을 배우고 더욱 성장하여 졸업할 수 있게 되어 기쁩니다. 힘든 날들이 많았지만 지도 교수님이신 김종면 교수님과 연구실 동료들의 도움이 없었다면 여기까지 올 수 없었을 것입니다. 저에게 있어 박사 학위는 저의 잠재력을 성장시켜주고 주변 사람들의 고마움을 깨닫게 해주었기에 학위 이상의 의미를 갖습니다.

제가 힘들고 지쳤을 때 항상 저를 이끌어 주시고 뜻 깊은 지도해주신 김종면 교수님께 깊은 감사의 말씀을 드립니다.

저의 논문을 세심하게 심사해주시고 아낌없는 조언을 해주신 권영근 교수님, 윤석훈 교수님, 정현상 박사님, 김기홍 박사님께 깊이 감사드립니다.

또한, 박사 생활 초에 저를 적극적으로 지도해주시고 저를 여기까지 올 수 있는 원동력을 제공해 주신 故강명수 선배님께 깊은 감사의 말씀을 전하고 싶습니다.

학위 생활 동안 서로에게 힘이 되어주고 지켜있을 때 많은 위로가 되어준 정인규, 손동구 선배님, 임기창 박사님과, 함께 생활해온 여러 연구실 동료분들께도 감사의 말씀을 드리며, 제가 연구에 집중할 수 있도록 적극적으로 지원해주신 하재경 선생님과 이정 선생님, 남승자 선생님께서도 감사의 말씀을 전합니다.

저의 길을 끝까지 믿어주시고 응원해주신 부모님과 형, 사랑하는 우리 가족들에게 정말 고맙습니다.

앞으로도 연구실 생활을 통해 향상된 저의 능력을 적극 발휘하여 사회에 공헌할 수 있는 참된 사회인이 될 것입니다.

김재영

2021년 1월 14일

**ABSTRACT****A Study on the Fault Diagnosis Technology and Application for  
Industrial Equipment using Deep Learning**

by

**Jaeyoung Kim****Supervisor: Prof. Jong-Myon Kim**

Submitted in partial fulfillment of the requirements for the Degree of Doctor of  
Philosophy (Computer Engineering)

Feb. 2021

With the recent progress of the 4th industrial revolution, many manufacturing industries focus on implementing a smart factory that can maximize the effect of increasing productivity and reducing labor costs. For maintaining stable operation of the smart factory, countermeasures must be prepared according to the increased uncertainty and complexity of the advanced system. To do this, it is necessary to extend the life of each equipment by utilizing an appropriate maintenance strategy. In this dissertation, deep learning-based algorithms are studied for reliable fault diagnosis of bearings and induction motors of a rotating equipment as well as circulating fluidized bed combustion boiler (CFBC) boiler tubes.

First, a bearing fault diagnosis technology is introduced based on a convolutional neural network (CNN). To improve classification performance of the CNN, a normalized bearing characteristic component (NBCC) is used generated by extracting bearing defect frequencies from spectrum of the acoustic emission signal. In addition, importance weights of features are extracted by using gradient-weighted class activation mapping (Grad-CAM) to enable CNN interpretation. Experimental results show that the proposed method achieves high

classification accuracy and CNN successfully learns bearing's characteristic frequency for each type of the bearing failure.

To further improve performance of the deep learning-based fault diagnosis method, two-dimensional CNN-based fault diagnosis methods have been studied by converting one-dimensional signal into two-dimensional data and learning it. In this study, a CNN-based fault diagnosis method is proposed using stacked envelope spectral image (SESI) to find a 2D representation of the AE signal based on the fault characteristic frequency of the bearing. SESI is designed to include general-purpose fault characteristics of bearings by extracting and stacking bearing fault frequencies from the envelope spectrum. When learning a 2D CNN using SESI, the learned CNN can directly learn fault frequency of the bearing. To verify performance of the proposed method, Experimental results show that fault diagnosis for each type of bearing with high performance is possible by mutually learning the data acquired from two different testbeds and performing a diagnostic test.

In addition to SESI, another new method, called “defect signature wavelet image (DSWI)”, is established to construct the 2-D fault diagnosis representation of multiple bearing defects from 1-D acoustic emission signals. This technique starts by applying envelope analysis to extract the envelope signal. A novel strategy is propounded for the deployment of the continuous wavelet transform with damage frequency band information to generate DSWI, which describes acoustic emission signal in time-frequency-domain, reduces the nonstationary effect in the signal, shows discriminate pattern visualization for different types of faults, and associates with the defect signature of bearing faults. Using the resultant DSWI, CNN architecture is designed to identify the fault in the bearing. To evaluate the proposed algorithm, the performance of this technique is scrutinized by a series of experimental tests acquired from a self-designed testbed and corresponding to different bearing conditions. Experimental results demonstrate that the proposed methodology outperforms conventional approaches in terms of classification accuracy. The result of combining CNN with DSWI input yields an accuracy of 98.79% for classifying multiple bearing defects.

Although deep learning-based fault diagnosis methods show excellent performance, machine learning-based fault diagnosis methods are still being studied. Since machine

learning-based fault diagnosis methods use features designed by experts, performance is excellent even when a small amount of data is learned compared to deep learning-based fault diagnosis, and features can also be analyzed. This thesis proposes a technique for diagnosing incipient bearing defects under variable speed conditions, by extracting features from different sub-bands of the inherently non-stationary AE signal, and then classifying bearing defects using a weighted committee machine, which is an ensemble of support vector machines and artificial neural networks. The proposed method also improves the generalization performance of neural networks to enhance their classification accuracy, particularly with limited training data.

In addition to bearings, induction motors are also very important parts that transmit power to drive equipment. Therefore, not only bearing fault diagnosis but also fault diagnosis of induction motors is vital in terms of maintenance of the equipment. In this thesis, a Mahalanobis distance-based classifier is proposed, which can diagnose various defects of induction motors including bearing failures, rotor unbalance, broken rotor bar, bowed rotor shaft, and rotor misalignment. The proposed method extracts an effective feature vector using the difference in harmonic components related to the failure of the vibration signal. After generating features from harmonic components for defects, diagnostic performance is improved with a classifier using Mahalanobis distance. Experimental results demonstrate that the proposed method has higher classification performance than the conventional method in both noiseless and white Gaussian noise environments.

Finally, a technique for estimating the tube leakage location of a CFBC boiler for thermal power generation is proposed. Since the fluid medium, which is the fuel of the CFBC boiler, is a small but hard solid like pulverized coal, it may cause abrasion of the waterwall tube as well as leakage due to the blow of the fluid medium. A method of estimating the leakage location of the CFBC boiler tube for thermal power generation is proposed using an acoustic emission sensor. The proposed method uses an acoustic emission sensor that can effectively detect the acoustic waves generated by the movement of a medium molecular unit, and uses a sensor sensitivity estimation algorithm for each location that considers the attenuation rates of the membrane welds and non-welded parts of the boiler water wall tube.

# Contents

<b>VITA</b> .....	iii
<b>ACKNOWLEDGMENTS</b> .....	iv
<b>ABSTRACT</b> .....	vi
<b>Contents</b> .....	ix
<b>List of Figures</b> .....	xii
<b>List of Tables</b> .....	xiv
<b>Nomenclature</b> .....	xv
<b>Chapter 1. Introduction</b> .....	1
1.1 Motivation .....	3
1.2 Thesis Outline .....	4
<b>Chapter 2 Bearing Fault Diagnosis using Grad-CAM and Acoustic Emission Signals</b> .....	7
2.1 Introduction .....	7
2.2 Proposed Method .....	8
2.2.1 Envelope Analysis .....	9
2.2.2 Bearing characteristic component analysis .....	10
2.2.3 Training DNN and Classification .....	13
2.2.4 Importance-weight extraction .....	14
2.3 Experimental Setup and Data Acquisition .....	15
2.4 Experimental Results and Discussion .....	18
2.5 Conclusion .....	19
<b>Chapter 3 Deep Learning-based Bearing Fault Diagnosis using Stacked-Envelope Spectral Image of Acoustic Emission Signals</b> .....	20
3.1 Introduction .....	20
3.2 Diagnosis methodology using the Stacked-Envelope Spectral Image and Deep learning algorithm .....	22
3.2.1 Envelope analysis to construct stacked-envelope spectral images .....	23
3.2.2 Training CNN structure for classification .....	27
3.3 Experimental Setup and Data Acquisition .....	29
3.3.1 Rotorkit testbed dataset .....	30
3.3.1 Laboratory designed bearing testbed dataset .....	31
3.4 Experimental Results and Discussion .....	33

3.4.1	Effective of the algorithm on RK-4 testbed dataset.....	33
3.4.2	Effective of the algorithm on laboratory designed bearing testbed dataset.....	34
3.4.3	Effective of training and testing with different datasets .....	35
3.5	Conclusion.....	38
<b>Chapter 4 A Deep-Learning-based Bearing Fault Diagnosis using Defect Signature Wavelet Image Visualization .....</b>		
<b>40</b>		
4.1	Introduction .....	40
4.2	Seed to the Data Acquisition System and Experimental Process .....	45
4.3	Fault Diagnosis Methodology Using the Defect Signature Wavelet Image .....	46
4.3.1	Bearing Fault Signature and Wavelet Analysis.....	47
4.3.2	2-D Data Representation with Defect Signature Wavelet Image Generation .....	50
4.3.3	Deep Convolution Neural Network Structure Specification .....	54
4.4	Methodology Evaluation Results .....	59
4.4.1	Performance Evaluation of DSWI Compared to Vibration Image and Conventional Wavelet Spectrogram .....	59
4.4.2	Performance Comparison with Difference Model for Classification .....	62
4.5	Conclusions .....	64
<b>Chapter 5 Incipient Fault Diagnosis in Bearings under Variable Speed Conditions using Multiresolution Analysis and a Weighted Committee Machine.....</b>		
<b>66</b>		
5.1	Introduction .....	66
5.2	The Acquisition of Acoustic Emission Data .....	67
5.3	The Proposed Methodology for Speed-Invariant Fault Diagnosis .....	68
5.4	Experimental Results and Discussion.....	75
5.5	Conclusions .....	76
<b>Chapter 6 A New Fault Classification Scheme Using Vibration Signal Signatures and the Mahalanobis Distance .....</b>		
<b>77</b>		
6.1	Introduction .....	77
6.2	Fault-Related Harmonics in Vibration Signals.....	79
6.2.1	Rotor unbalance (RU).....	79
6.2.2	Faulty bearings (FB).....	79
6.2.3	Broken rotor bar (BR).....	80
6.2.4	Bowed rotor shaft (BS).....	81
6.2.5	Rotor misalignment (parallel (PM) and angular (AM)) .....	81

6.3	Proposed Method .....	81
6.3.1	Production of fault signatures in vibration signals .....	82
6.3.2	Online detection and classification system.....	85
6.4	Experimental Results.....	86
6.4.1	Experiment and simulation setup .....	86
6.5	Conclusion .....	88
<b>Chapter 7 Heatmap-based Leakage Localization Algorithm using Acoustic Emission Sensor for Circulating Fluidized Bed Combustion Boiler Tube .....</b>		<b>90</b>
7.1	Introduction .....	90
7.2	Proposed Methodology.....	91
7.2.1	Sensor localization method.....	91
7.2.2	Leakage localization method using heatmap.....	92
7.3	Experimental Setup .....	92
7.4	Experimental Result .....	95
7.5	Conclusions .....	96
<b>Chapter 8 Summary of Contributions and Future Works .....</b>		<b>97</b>
8.1	Introduction .....	97
8.2	Summary of Contributions .....	97
8.3	Future Works.....	99
<b>Publications .....</b>		<b>101</b>
<b>References .....</b>		<b>105</b>

## List of Figures

<b>Figure 2.1</b> Flowchart of the proposed approach .....	9
<b>Figure 2.2</b> The flowchart of envelope analysis. Hilbert-transform is applied to AE signal to calculate 90-degree phase-shifted signal. Then, analytical signal is calculated by sum of the original signal and its Hilbert-transform as an imaginary number. Next, the envelope signal is calculated by applying absolute operation to the previously computed analytical signal. Finally, the fast Fourier transform of the envelope signal provides envelope spectrum.....	10
<b>Figure 2.3</b> Examples of the ideal signals for each type of bearing fault .....	11
<b>Figure 2.4</b> The extraction process of bearing characteristic components.....	12
<b>Figure 2.5</b> DNN structure for bearing fault diagnosis .....	13
<b>Figure 2.6</b> The flowchart of Grad-CAM with an example of CNN structure .....	14
<b>Figure 2.7</b> Illustration of the bearing fault simulator .....	15
<b>Figure 2.8</b> Photographs of the experimental setup .....	16
Figure 2.9 Illustration of bearing, FAG NJ206-E-TVP2.....	16
<b>Figure 2.10</b> The seeded bearing faults: (a) Outer race way with a crack on its surface (ORCS); (b) Inner race way with a crack on its surface (IRCS); (c) rolling element with a crack on its surface (RECS). .....	17
<b>Figure 2.11</b> The examples of AE signals for each bearing conditions listed as: (a) The AE signal of healthy bearing; (b) The AE signal of ORCS; (c) The AE signal of IRCS; (d) The AE signal of RECS. ....	17
<b>Figure 2.12</b> Confusion matrix of classification result.....	18
<b>Figure 2.13</b> Importance weights from Grad-CAM for DNN .....	19
<b>Figure 3.1</b> The proposed method for segment data.....	25
<b>Figure 3.2</b> The overall scheme of SESI extraction and CNN classification .....	26
<b>Figure 3.3</b> CNN structure for bearing fault diagnosis .....	29
<b>Figure 3.4</b> The rotorkit testbed setup.....	31
<b>Figure 3.5</b> The laboratory designed testbed setup.....	32
<b>Figure 3.6</b> The result of the proposed method for RK-4 testbed dataset .....	33
<b>Figure 3.7</b> The result of the proposed method for laboratory testbed dataset.....	34
<b>Figure 3.8</b> The result of the proposed method for the scenarios (1) test: .....	35
<b>Figure 3.9</b> The result of the proposed method for the scenarios (2) test: .....	36
<b>Figure 3.10</b> Example of inner SESI which is blurred by high level of noise.....	36
<b>Figure 3.11</b> Vibration image from the RK-4 dataset and Laboratory testbed dataset .....	37
<b>Figure 4.1</b> The self-defined testbed setup for measuring signals of bearing faults .....	45
<b>Figure 4.2</b> 2-D representation of the signal corresponding to the outer fault: (a) DSWI, (b) envelope signal, (c) envelope spectrum with FO defect frequency, and (d) outer defect frequency FO, respectively .....	48
<b>Figure 4.3</b> 2-D representation of the signals corresponding to the inner and roller faults: (a) DSWI for inner fault, (b) envelope signal for inner fault, (c) envelope spectrum with FI defect frequency for inner fault, (d) inner defect frequency FI, (e) DSWI for roller fault, (f) envelope signal for roller fault, (g) envelope spectrum with SF defect frequency for roller fault, and (h) roller (ball spin) defect frequency SF, respectively. ....	50

**Figure 4.4** Generating the DSWI representation and process for fault diagnosis..... 52

**Figure 4.5** The proposed deep convolution neural network architecture diagram for the 128 × 128 size images ..... 58

**Figure 4.6** The generated image of bearing fault signal from different methods: (a) Vibration image (b) Conventional Wavelet spectrogram image (c) DSWI ..... 61

**Figure 4.7** The generated image of bearing fault signal from different methods: (a) Vibration image (b) Conventional Wavelet spectrogram image (c) DSWI. .... 62

**Figure 5.1** The proposed method for incipient fault diagnosis under variable speed conditions using a WCM..... 68

**Figure 5.2** The proposed method for incipient fault diagnosis under variable speed conditions using a WCM..... 69

**Figure 5.3** The algorithm for optimizing the ANN committee ..... 74

**Figure 5.4** The decision values of SVMCMs in SVMCG 1 ..... 75

Figure 5.5 The performance of different number of sub-bands for datasets 1 and 2..... 76

**Figure 6.1** Proposed online fault classification system..... 82

**Figure 6.2** Fault signatures in the vibration signal generation process ..... 82

**Figure 6.3** Performance under different conditions ..... 87

**Figure 7.1** A block diagram of sensor localization algorithm ..... 91

**Figure 7.2** A scheme of CFBC testbed for imitating tube leakage ..... 93

**Figure 7.3** Photographs of CFBC testbed for imitating tube leakage ..... 94

**Figure 7.4** A concept of CFBC testbed for imitating tube leakage ..... 95

## List of Tables

<b>Table 2.1</b> Bearing characteristic frequencies.....	12
<b>Table 2.2</b> The specification of the target bearing, FAG NJ206-E-TVP2.....	17
<b>Table 3.1</b> Details of data acquisition system .....	32
<b>Table 3.2</b> Classification result of the proposed method compare with vibration image method.....	38
<b>Table 4.1</b> Specifications of measuring sensors and data acquisition card .....	46
<b>Table 4.2</b> The classification report of the test dataset for different types of input and different classification methodology .....	64
<b>Table 5.1</b> Classification result of the proposed method compare with vibration image method.....	68
<b>Table 5.2</b> The three statistical features of the frequency-domain AE sub-band signal. Here, $S(f)$ is the magnitude response of the FFT of $x(n)$ and $N_{\text{tfreqbin}}$ is the total number of frequency bins.....	71
<b>Table 5.3</b> The 16 statistical features of the time-domain AE sub-band signals. Here, $x$ is an input signal, $N$ is the total number of samples.....	71
<b>Table 5.4</b> Average classification accuracies and sensitivities for single and multiple combined bearing defects using different levels of decomposition of the original AE signal.....	72
<b>Table 6.1</b> Details of fault conditions .....	86

## Nomenclature

1-D	One Dimensional
2-D	Two Dimensional
AE	Acoustic Emission
AM	Angular Misalignment
ANN	Artificial Neural Network
ANNC	Artificial Neural Networks as a Combiner
BCC	Bearing Characteristic Component
BCIO	Cracks on the Inner and Outer Raceways
BCIOR	Cracks on the Inner Raceway, Outer Raceway, and Roller
BCIR	Cracks on the Inner Raceway and Roller
BCOR	Cracks on the Outer Raceway and Roller
BNC	Bearing in Normal Condition
BPFI	Ball Pass Frequency on the Outer Race
BPFO	Ball Pass Frequency on the Outer Race
BR	Broken Rotor Bar
BS	Bowed Rotor Shaft
BSF	Ball Spin Frequency
CFBC	Circulating Fluidized Bed Combustion Boiler
CNN	Convolutional Neural Network
CWT	Continuous Wavelet Transform
DAQ	Data Acquisition
DNN	Deep Neural Network
DSWI	Defect Signature Wavelet Image
DWPT	Discrete Wavelet Packet Transform
FB	Faulty Bearing
FC	Fully Connected
FFT	Fast Fourier Transform
GRAD-CAM	Gradient-Weighted Class Activation Mapping
HB	Healthy Bearing
HI	Health Index
HT	Hilbert Transform
IEPE	Integrated Electronics Piezo-Electric
IRCS	Inner Race Way with a Crack on its Surface
k-NN	k-Nearest Neighbors
LM	Levenberg-Marquardt
LPC	Linear Predictive Coding

MCSVM	Multi-class SVM
MOMEDA	Multipoint Optimal Minimum Entropy Deconvolution Adjusted
MRA	Multiresolution Analysis
NBCC	Normalized Bearing Characteristic Component
NO	One Healthy Condition
OAA	One-Against-All
ORCS	Outer Race Way with a Crack on its Surface
PM	Parallel Misalignment
RBF	Gaussian radial basis function
RBM	Risk-Based Maintenance
RCM	Reliability-Centered Maintenance
RECS	Rolling Element with a Crack on its Surface
ReLU	Rectified Linear Unit
RMS	Root Mean Square
RPM	Revolution per Minute
RU	Rotor Unbalance
RUL	Remaining Useful Life
SESI	Stacked Envelope Spectral Image
SNR	Signal-to-Noise Ratio
SVM	Support Vector Machine
SVMCG	Support Vector Machine Committee Groups
WCM	Weighted Committee Machine

## **Chapter 1**

### **Introduction**

With the recent progress of the 4th industrial revolution, many manufacturing industries are promoting the introduction of smart factories that can maximize the effect of increasing productivity and reducing labor costs. Smart factory refers to an evolved factory that integrates the entire production process such as planning, design, production, distribution, and sales with information and communication technology (ICT) to produce customized products with minimal cost and time. However, for the stable operation of smart factories, countermeasures must be prepared according to the increase in the uncertainty and complexity of the advanced system, and for this, it will be necessary to extend the life of the equipment by utilizing an appropriate maintenance strategy. In the case of an automated manufacturing plant where economic losses due to sudden operation disruption are very large, it can be said that securing an appropriate maintenance strategy is important in implementing a smart plant. Representative maintenance strategies include period-based maintenance, which is regularly maintained at regular time intervals, and post-maintenance that performs maintenance after a failure, but wastes costs by unnecessary replacement regardless of the presence or absence of defects and prevents sudden equipment failure. There are limitations. Reliability-Centered Maintenance (RCM) and Risk-Based Maintenance (RBM) have been studied and introduced to solve the problems arising from such post-maintenance and preventive maintenance. RCM analyzes data generated during operation and secures reliability through conservation policies to ensure that replacement occurs at an appropriate lifetime. RBM plans maintenance by calculating the degree of risk based on the frequency of failure and the cost of post-treatment [1]. In recent years, due to the development of big data and artificial intelligence technology, research has been actively conducted to improve diagnostic performance by applying artificial intelligence technology to data collected in real time and RCM and RBM technology [2]–[5].

Fault diagnosis is to detect and identify faults in facilities and extract specific fault-related information such as fault type, fault severity, fault location, etc. [6]. Failure prediction is a technology that estimates the remaining useful life (RUL) within a specific confidence interval, and it requires additional information that cannot be measured with sensors alone, such as past

failure and maintenance history, and changes in operating environment [7]. Diagnosis and prognosis methods are classified into model-based and data-based approaches, and hybrid approaches that combine the two [6]–[9]. The model-based approach is a method of predicting potential failures and remaining life based on a mathematical model calculated physically and mechanically. To apply the model-based approach to fault diagnosis and prediction of remaining life, a well-established model is needed in mechanical physics that can explain the relationship between the measured signal and the equipment defect. The strength of the model-based method is that if the correct parameters for the target machine can be entered into the designed diagnostic model, the machine can be diagnosed with high accuracy even in various operating environments or operating conditions. However, since a lot of expertise is required to construct such a diagnostic model, it is difficult to find suitable parameters when the target machine has high complexity, and considerable expertise and effort are required to design an accurate diagnostic model [10]. Due to the shortcomings of such a model-based approach, most recent fault diagnosis and prediction techniques are being studied through data-based approaches. The data-driven approach proceeds in three main steps:

- Step 1-Acquisition of signals: Measure signals to be used for fault diagnosis and prediction, such as vibration acceleration [11]–[13], acoustic emission[14], [15], or stator current signal [16] using a measuring device.
- Step 2-Feature extraction: From the collected signals, features of normal and fault conditions are extracted to be used for input of the diagnostic model. In addition, the extracted features are also used as a health indicator (HI) of a failure prediction model for failure prediction.
- Step 3-Diagnosis of faults: Various types of defects are identified by inputting features extracted using machine learning-based classifiers such as k-Nearest-Neighbour (k-NN), Support Vector Machine (SVM), or Artificial Neural Network (ANN). Classify. In addition, in failure prediction, a health index is learned, and RUL is predicted using a linear or nonlinear regression model.

The advantage of the data-based approach is that unlike the model-based approach, system parameters are not required, and if enough data is secured, it can be used without detailed

mechanical information. In addition, since the machine learning model is trained based on data, it is possible to perform fault diagnosis and prediction by detecting data changes even in a complex system through a periodic learning process. In this dissertation, fault diagnosis and prediction studies were introduced for bearing, induction motor, and CFBC boiler tube using acoustic emission and vibration signals.

## **1.1 Motivation**

Nowadays, electrical machines are profoundly used in the industries to carry out numerous tasks. These machines consist of two main parts; 1) stator and 2) rotor [17]. The rotor part of the machines contains bearings that are vital to reduce the friction among different components of the machines [18]. Different cracks and spalls appear on the bearing due to harsh working conditions that can lead to the failure of the machines [19]. Bearings contribute to the 50-51% of the rotary machine failures [20]. The failure of the machines leads to unwanted downtime, substantial economic losses and put the safety of the workers at risk. To mitigate the problem, the maintenance of the rotating machines is compulsory. There are two main categories of the machine's maintenance. The first one is the reactive maintenance and the second is proactive maintenance [21]. In reactive maintenance, the ineffective or damaged components of the machines are repaired or replaced so that the machine may continue its function smoothly. So, in this kind of maintenance, there is no need to take preventive measures and the issue is addressed when it is reported. On the other hand, in the proactive maintenance preventive measures are taken to mitigate the machine failure. Further, the proactive maintenance is divided into two categories: 1) preventive maintenance 2) predictive maintenance. In preventive maintenance, the maintenance of the machine is carried out on the routinely basis. Whereas, in predictive maintenance, the techniques are developed that can help to assess the health states of the components and predict when maintenance is needed for the machine. In this way, unnecessary downtime of the machine can be avoided and cut off the economic losses and improves the safety measures within the industry. So, fault diagnosis can be categorized as predictive maintenance of the electric machines, as it predicts the health states of the machine's bearing.

There are numerous studies present that have been conducted to develop fault diagnosis techniques for rotating machines bearings. These traditional bearing fault diagnosis techniques mainly rely on the classical machine learning algorithms; for instance, ANN, SVM, and k-NN [22]–[24]. These algorithms are shallow in nature and are inefficient while dealing with the complex signals obtained from the bearings where there is shaft speed fluctuation.

In recent years deep learning is making its mark in many fields including image processing [25], [26], speech recognition [27], natural language process [28], medical image processing [29], etc. Such deep networks have the capability of extracting meaningful information through their deep architectures and by using nonlinear transformation in the hidden layers from the provided inputs which can be further used as higher-level features for classification purposes.

The objective of this dissertation is to perform fault diagnosis of mechanical equipment that includes (i) deep-learning-based fault diagnosis for bearings, (ii) machine-learning-based fault diagnosis for bearings and induction motor, (iii) Leakage detection and localization of CFBC Boiler tube.

## **1.2 Thesis Outline**

The dissertation is composed of 8 Chapters including introduction, i.e., Chapter 1. Deep-learning-based fault diagnosis of bearings under inconsistent working conditions is presented in Chapter 2, 3, and 4. Machine-learning-based fault diagnosis of bearings and induction motors is introduced in Chapter 5. Leakage detection and localization of CFBC boiler tube are given in Chapter 7. Finally, Chapter 8 concludes contribution and further research.

Chapter 2 discusses the mechanism of reliable fault diagnosis of rotary machine bearings with the help of a deep neural network. NBCC was proposed to extract the bearing defect frequency from the spectrum of the acoustic emission signal was used. To enable CNN interpretation, the importance weights of features were extracted using Grad-CAM.

In Chapter 3, two-dimensional CNN-based fault diagnosis methods have been studied by converting a one-dimensional signal into two-dimensional data and learning it. To solve such a problem, a study was conducted to extract a consistent and understandable image

pattern by extracting and stacking the defect frequency that appears when a defect occurs from the spectrum. In this chapter, a CNN-based fault diagnosis method was explained, which uses SESI to find a 2D representation of the AE signal based on the fault characteristic frequency of the bearing. SESI is designed to include general-purpose fault characteristics of bearings by extracting and stacking bearing fault frequencies from the envelope spectrum. When learning a 2D CNN using SESI, the learned CNN can directly learn the fault frequency of the bearing.

Chapter 4 is about a novel strategy which generates DSWI using the continuous wavelet transform with damage frequency band information. DSWI describes the acoustic emission signal in time-frequency-domain, reduces the nonstationary effect in the signal, shows discriminate pattern visualization for different types of faults, and associates with the defect signature of bearing faults. Using the resultant DSWI, the CNN architecture is designed to identify the fault in the bearing

Chapter 5 introduces a technique for diagnosing incipient bearing defects under variable speed conditions, by extracting features from different sub-bands of the inherently non-stationary AE signal, and then classifying bearing defects using a weighted committee machine, which is an ensemble of support vector machines and artificial neural networks. The proposed method also improves the generalization performance of the neural networks to enhance their classification accuracy, particularly with limited training data.

In Chapter 6, a Mahalanobis distance-based classifier was introduced, which can diagnose various defects of induction motors including bearing failures, rotor unbalance, broken rotor bar, bowed rotor shaft, and rotor misalignment. The proposed method extracts an effective feature vector using the difference in harmonic components related to the failure of the vibration signal. After generating features from harmonic components for defects, diagnostic performance was improved with a classifier using Mahalanobis distance.

Chapter 7 is about a technique for estimating the tube leakage location of a circulating CFBC boiler for thermal power generation. Since the fluid medium, which is the fuel of the CFBC boiler, is a small but hard solid like pulverized coal, it may cause abrasion of the waterwall tube as well as leakage due to the blow of the fluid medium. A method of estimating

the leakage location of the CFBC boiler tube for thermal power generation is proposed using an acoustic emission sensor. The proposed method utilizes an acoustic emission sensor that can detect the acoustic waves generated by the movement of a medium molecular unit. sensor sensitivity estimation algorithm is performed for each location that considers the attenuation rates of the membrane welds and non-welded parts of the boiler water wall tube. The amplitude of each location is expressed as a heatmap.

Finally, chapter 8 concludes the thesis and presents a summary of the contributions and discusses future work.

## **Chapter 2**

### **Bearing Fault Diagnosis using Grad-CAM and Acoustic Emission Signals**

#### **2.1 Introduction**

Bearings are vital components of heavy rotating machines that reduce friction between a rotating shaft and fixed components such as bearing housings. It is known that 45-55% of failures of rotating machines are caused by bearing faults [30]. Hence, it is important to detect the arising bearing faults at early stages to prevent the secondary failure of the manufacturing equipment. In the past decades, many bearing fault diagnosis techniques have been developed based on acoustic emission (AE). AE is the process of generation of transient elastic waves from sudden cyclic fatigue, fracture, impacting, etc. [31]–[34]. Regarding bearings, the acoustic waves can be generated when the rolling elements of bearing hit the cracked surface on inner race, outer race, and rolling element. The advantage of AE-based analysis is its capability of detecting very low-energy signals caused by bearing failures at an early-stage or during slow-speed operation [31]. However, since the sampling rate used for AE signal collection is usually higher than 1 MHz, it is difficult to analyze the AE signal because of the tremendous amounts of data in the collected time-series (due to high signal sampling rates) and computational time required for analysis. Model-based feature extraction is one of promising approaches to overcome these issues because it converts big raw data instances into small feature vectors. Multipoint optimal minimum entropy deconvolution adjusted (MOMEDA) is introduced to extract informative features in several papers [35]–[37]. In these studies, the MOMEDA has been utilized to extract fault period impulse component as features which is demodulated signal. Other papers developed deep neural network (DNN)-based bearing fault diagnosis methods [38]–[43]. DNN-based bearing diagnosis methods are powerful tools to extract informative features by learning feature representations from a large amount of raw data. Recently, some papers compared the performance of CNN and DNN-based approaches. These papers concludes that the CNN-based techniques are much better than DNN-based methods in terms of fault diagnosis performance [32], [41], [44], [45]. Although DNN or CNN-based methods have achieved high classification accuracy, there are still two issues that must be resolved to make these methods highly applicable to real

applications. The first issue is that the trained neural network, in general, can be only reliable on the specific machine since the patterns of the raw signals strongly depend on the operating conditions of the machinery such as load, installation, external vibration, etc. The second concern is that the trained feature representation is uninterpretable due to the black box-like operation of the neural networks.

This research proposes a new CNN-based rolling element bearing fault diagnosis approach to resolve the aforementioned problems. To address the first issue, the proposed method utilizes NBCC as the input data of CNN rather than raw AE signal itself. Since the bearing characteristic frequencies are induced by appearing bearing failures, NBCC is a more effective representation for diagnosing the bearing failure symptoms. To resolve the second issue, this research applies Grad-CAM to visualize important regions in NBCC. According to the literature, Grad-CAM is a promising method that provides visual explanations of the classification result of a CNN in object detection and recognition [46].

The remainder of this chapter is organized as follows. Section 2 introduces the proposed methodology for diagnosing rolling element bearing faults using AE signals. In Section 3 the bearing fault simulator used for collecting AE signals is presented. The fault diagnosis results demonstrated and discussed in Section 4. Finally, Section 5 contains the concluding remarks.

## **2.2 Proposed Method**

Figure 2.1 illustrates the process of diagnosing bearing faults by the proposed method as a flowchart. In step 1, the envelope power spectra are calculated from pre-acquired AE signals containing healthy and faulty conditions. In step 2, frequency magnitudes are extracted from the characteristic frequency range of the bearing and used as features. In step 3, the CNN is trained using the extracted features. Here, the envelope power spectra of new AE signals are classified into healthy or faulty condition using the trained CNN. Finally, in step 4, the importance weights with frequency are generated including valuable regions in the envelope

spectrum using Grad-CAM for the acquired AE signals.

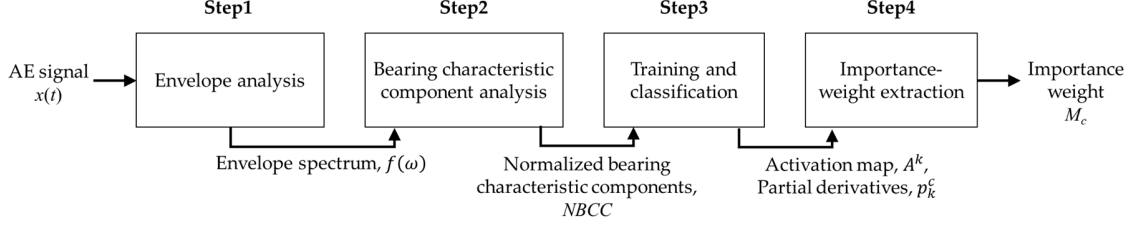


**Figure 2.1** Flowchart of the proposed approach

### 2.2.1 Envelope Analysis

Since the impulses generated by bearing failures are amplitude-modulated, AE signals should be first demodulated to extract pure burst signals. As shown in Figure 2.2, Hilbert-transform-based envelope analysis is used to demodulate the AE signal [14], [47]. First, the Hilbert-transform is applied to the AE signal as follows [47]:

$$\hat{x}(t) = \frac{1}{\pi} \int_{-\infty}^{\infty} \frac{x(\tau)}{t - \tau} d\tau, \quad (2.1)$$

where  $t$  is the time,  $x(\tau)$  is a sample of the input signal at  $\tau$ , and  $\hat{x}(t)$  is a sample of the Hilbert transformed signal at time  $t$ . Hilbert-transform shifts the phase of the input signal by 90 degrees.

To obtain the analytical signal,  $z(t)$ , the Hilbert-transformed signal,  $\hat{x}(t)$ , and input signal,  $x(t)$  are combined as complex numbers [47]:

$$z(t) = x(t) + i\hat{x}(t), \quad i = \sqrt{-1}. \quad (2.2)$$

Then, the envelope signal,  $e(t)$  is computed as  $|z(t)|$ . Finally, the envelope spectrum,  $f(\omega)$  is calculated as the square root of the fast Fourier transform of  $e(t)$  as follows:

$$f(\omega) = \int_{-\infty}^{\infty} x(t) e^{-j\omega t} dt. \quad (2.3)$$

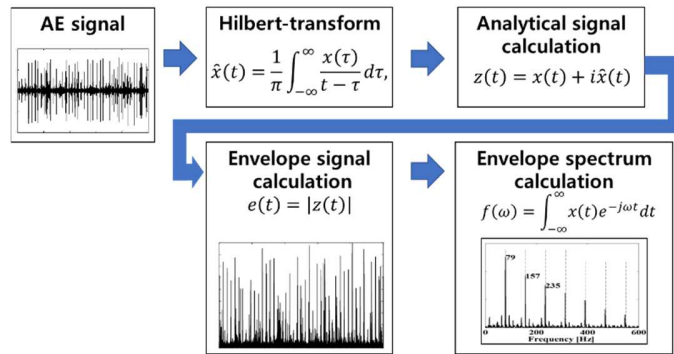


**Figure 2.2** The flowchart of envelope analysis. Hilbert-transform is applied to AE signal to calculate 90-degree phase-shifted signal. Then, analytical signal is calculated by sum of the original signal and its Hilbert-transform as an imaginary number. Next, the envelope signal is calculated by applying absolute operation to the previously computed analytical signal. Finally, the fast Fourier transform of the envelope signal provides envelope spectrum.

**2.2.2 Bearing characteristic component analysis**

Bearing failures generate periodic burst signals that are represented as the bearing characteristic frequency harmonics in the spectrum [48]. Outer race way with a crack on its surface (ORCS) emits a periodic pulse each time when the rolling element passes over the cracked surface. Since the outer race is a static component of the bearing and the applied load to cracked surface is always stable, the amplitude of the impulses does not change. Inner race way with a crack on its surface (IRCS) generates a series of impulses when each rolling element hits the crack on the inner race of the bearing. By rotating the inner ring with the shaft, the response of impulses grows up periodically when the inner race passes loaded zone which is oriented to the direction of gravity. Since this phenomenon modulates the impulses by rotating speed, the sideband of rotating speed appears nearby the characteristic frequency of inner race. Rolling element with a crack on its surface (RECS) generates impulses by hitting inner and outer races. Magnitude of the impulse is affected whether the contact occurred in the loaded or unloaded zones. Similarly, the sideband of RECS is fundamental train frequency [48]. Figure 2.3 illustrates the examples of the ideal signals for ORCS, IRCS, and RECS.

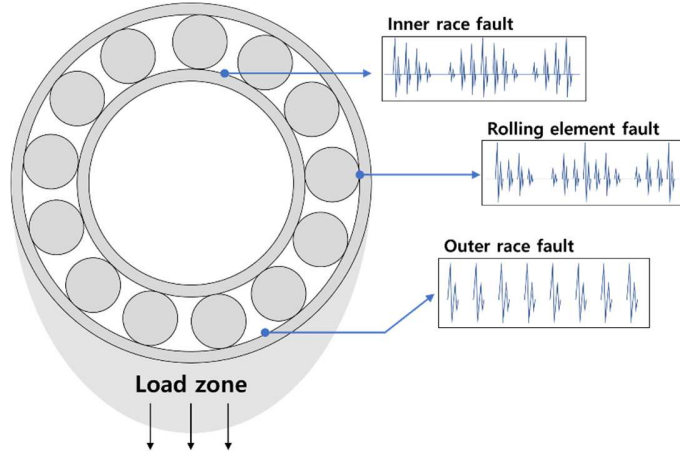


**Figure 2.3** Examples of the ideal signals for each type of bearing fault

Accordingly, the bearing characteristic (or defect) frequencies are categorized into ball pass frequency on the outer race (BPFO), ball pass frequency on the inner race (BPFI), and ball spin frequency (BSF). BPFO, BPFI, and  $2 \times \text{BSF}$  are caused by the bearing failures of outer race, inner race, and rolling element, respectively. The bearing characteristic frequencies are defined as follows [48]:

$$BPFO = \frac{Nb}{2} \times S \times \left[ 1 - \left( \frac{Bd}{Pd} \times \cos\theta \right) \right], \quad (2.4)$$

$$BPFI = \frac{Nb}{2} \times S \times \left[ 1 + \left( \frac{Bd}{Pd} \times \cos\theta \right) \right], \quad (2.5)$$

$$BSF = \frac{Pd}{2Bd} \times S \times \left[ 1 - \left( \frac{Bd}{Pd} \times \cos\theta \right)^2 \right], \quad (2.6)$$

where  $Nb$  is the number of rolling elements,  $S$  is the shaft speed,  $Bd$  is the diameter of the rolling element,  $Pd$  is the pitch diameter, i.e., the distance between the center of a rolling element and the center of the inner race, and  $\theta$  is a contact angle of the rolling element with respect to the shaft.

The bearing characteristic components (BCCs) are extracted as an input vector of the CNN. BCCs are defined as follows:

$$BCC(k) = f(\omega), \omega = 0, \dots, F_{max}, \tag{2.7}$$

where  $f$  are the values of the envelope spectrum and  $F_{max}$  is the frequency which is higher than all the harmonics of bearing characteristic frequencies as below:

$$F_{max} = \max(BPFO, BPFI, BSF) \times n + f_{side}, \tag{2.8}$$

where  $n$  is the number of frequency harmonics and  $f_{side}$  is the sideband of the highest characteristic frequency. Table 2.1 shows  $f_{side}$  for each type of bearing characteristic frequency. In this chapter,  $F_{max}$  is equal to BPFI which is the highest among the bearing characteristic frequencies. Figure 2.4 depicts the extraction process of BCCs.

**Table 2.1** Bearing characteristic frequencies

Bearing characteristic frequency	Sideband ( $f_{side}$ )
BPFO	No sideband
BPFI	Shaft speed
BSF	Fundamental train frequency <sup>1</sup>

<sup>1</sup> This frequency is generated when the roller cage enters the load zone [49] (3.3Hz in this study).

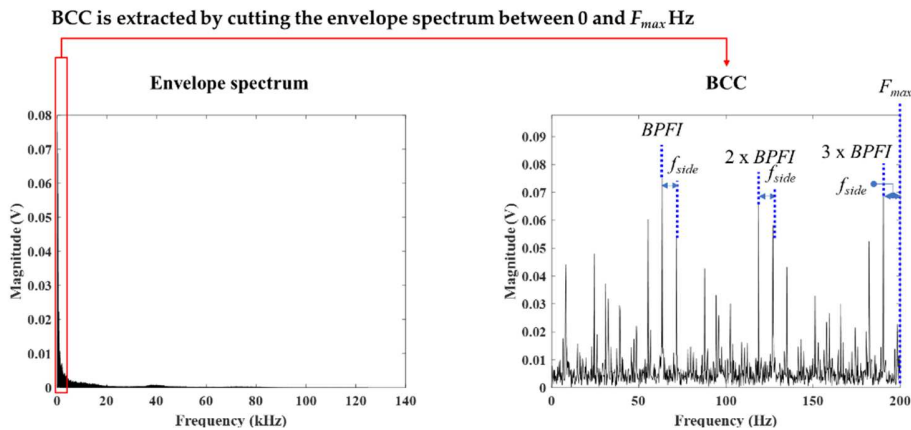


**Figure 2.4** The extraction process of bearing characteristic components

Since the variation of magnitude makes the training CNN unstable, BCCs are min-max normalized to be used for input data of CNN as follows:

$$NBCC(i) = \frac{BCC(i) - \min(BCC)}{\max(BCC) - \min(BCC)}, i = 0, \dots, F_{max}. \quad (2.9)$$

### 2.2.3 Training DNN and Classification

The structure of CNN is represented in Figure 2.5. The proposed CNN has six convolutional layers and two fully-connected (FC) layers. Each convolutional layer consists of a one-dimensional (1-D) convolutional layer, a batch-normalization layer, and a rectified linear unit (ReLU). All convolutional layers are connected to each other using a max pooling layer with down-sampling factor of 2. The input size of each convolutional layer is half of the input size of the previous convolutional layer, except for the first layer. The FC layers and softmax role classification are the last layers [50]. For the training process, multiclass categorical cross-entropy is used as the loss function, and Adam optimization algorithm is used for backpropagation [51].

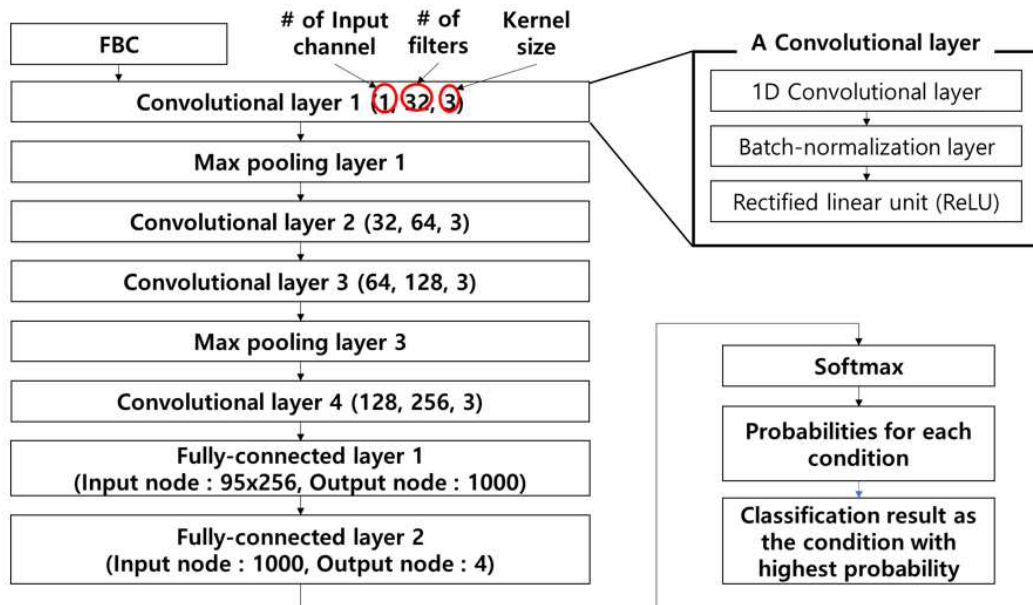


Figure 2.5 DNN structure for bearing fault diagnosis

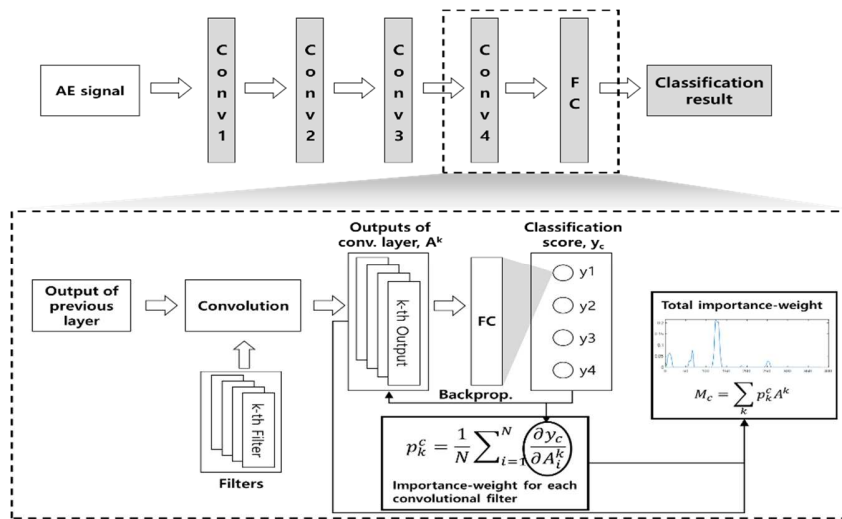
### 2.2.4 Importance-weight extraction

Figure 2.6 illustrates the flowchart of Grad-CAM with an example of CNN structure. Each convolutional layer consists of several filters with trainable filter coefficients. CNN applies these filters to the input data for extracting the informative features from the data. In Grad-CAM, the outputs of final convolutional layers are used to calculate the importance-weight for each characteristic frequency in *NBCC*. To obtain the importance-weight, a partial derivative of the score for class  $c$  is calculated of the  $k$ -th activation map. The following equation represents the definition of  $p_k^c$  [52]:

$$p_k^c = \frac{1}{N} \sum_{i=1}^N \frac{\partial y_c}{\partial A_i^k} \quad (2.10)$$

where  $p_k^c$  indicates the importance-weight of the  $k$ -th filter for class  $c$ ,  $y_c$  is a classification score of class  $c$ , and  $A_i^k$  is  $i$ -th element in  $k$ -th activation map. When CNN is being trained,  $\frac{\partial y_c}{\partial A_i^k}$  is calculated in back-propagation step. Finally, the importance-weight of class  $c$  is calculated as follows [52]:

$$M_c = \sum_k p_k^c A^k. \quad (2.11)$$



**Figure 2.6** The flowchart of Grad-CAM with an example of CNN structure

### 2.3 Experimental Setup and Data Acquisition

To validate the proposed method, a bearing fault simulator is used for measuring healthy and faulty-state AE signals of the rolling element bearing. The established bearing fault simulator is illustrated in Figures 2.7 and 2.8. On the drive-end shaft, a three-phase induction motor is connected to a gearbox by flexible coupling. The gearbox transfers the torque of the induction motor to the non-drive-end shaft with a gear reduction ratio of 1.52:1. A tachometer is installed to measure the rotating speed of the non-drive-end shaft. A cylindrical roller bearing (FAG NJ206-E-TVP2), which is the target bearing of the experiment, is installed in the bearing housing of the non-drive-end shaft. To apply radial and axial load, a fan with adjustable blades is connected to the non-drive-end shaft via a belt. The shaft speed is 500 revolutions per minute (RPM) in this study. An AE sensor is attached on the bearing housing of the target bearing. The measurement device for obtaining AE signals is a PCI-2-based system. A general-purpose wideband AE sensor, whose frequency response is between 100 kHz and 1000 kHz, is used to capture resonance frequency signals containing modulated bearing signals.

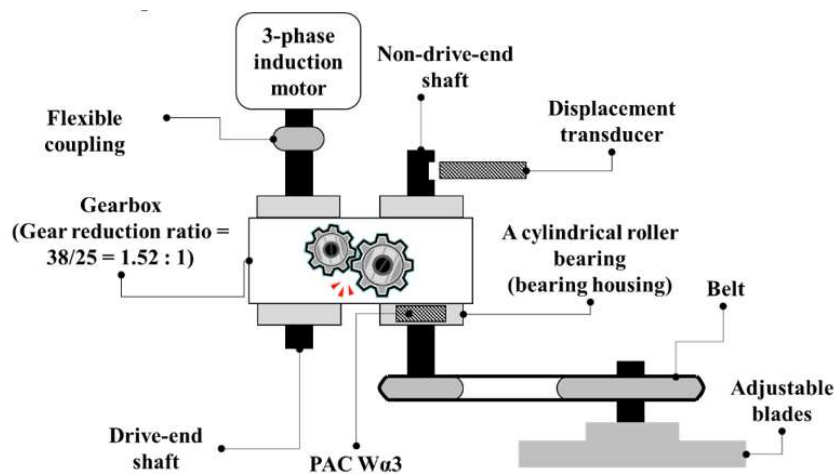


**Figure 2.7** Illustration of the bearing fault simulator

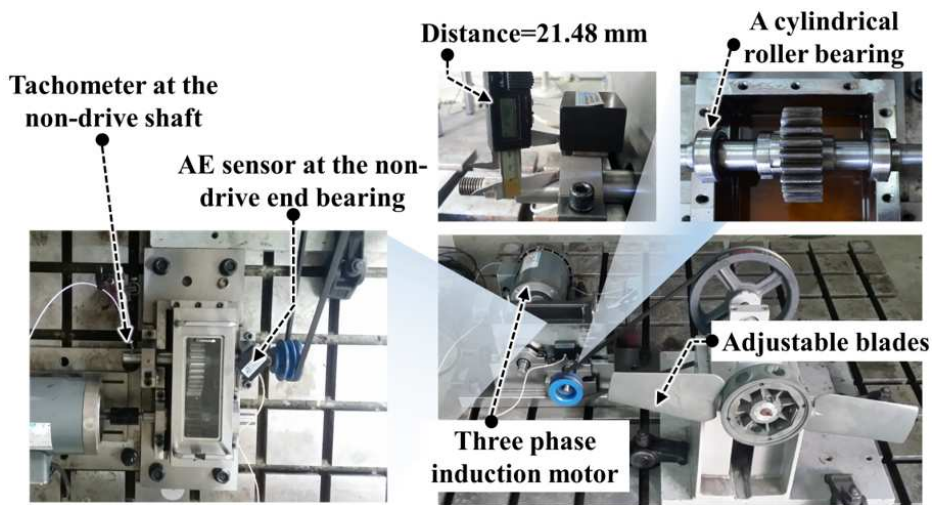


**Figure 2.8** Photographs of the experimental setup

Figure 2.9 and Table 2.2 shows the specification of the target bearing. Contact angle is 0 because the target bearing is a radial bearing. By using the Equations (2.4-2.6) with the bearing parameters and shaft speed, the bearing characteristic frequencies of BPFO, BPFI, and BSF are equal to 43.68 Hz, 20.72 Hz, and 64.65 Hz, respectively.

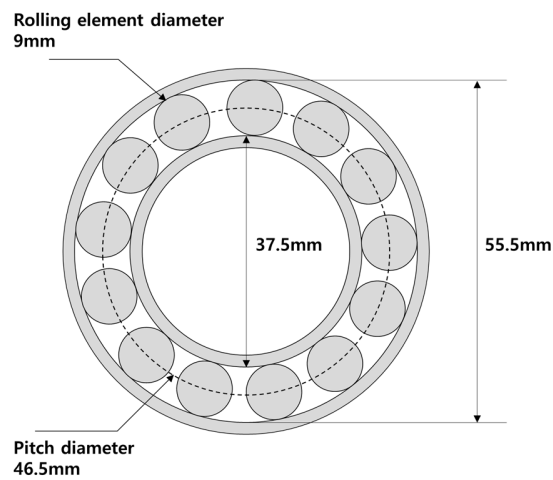


**Figure 2.9** Illustration of bearing, FAG NJ206-E-TVP2

**Table 2.2** The specification of the target bearing, FAG NJ206-E-TVP2

Category	Symbol in equations	Value (mm)
Pitch diameter	$Pd$	46.5
The diameter of rolling element	$Bd$	9
Contact angle of rolling element	$\theta$	0
The number of rolling elements	$Nb$	13
Pitch diameter	$Pd$	46.5

The seeded bearing faults, which are outer race way with ORCS, IRCS and RECS, are shown in Figure 2.10. The crack dimension of bearing failures is 6mm x 0.5mm x 0.5 mm. In addition, Figure 2.11 illustrates an example of AE signals for each bearing condition in dataset. As shown in Figure 2.11, healthy bearing (HB) contains less impulses than ones in faulty conditions. On the contrary, the signal of bearing faults such as ORCS, IRCS, and RECS emit more impulses created by the cyclic impacts of faults.

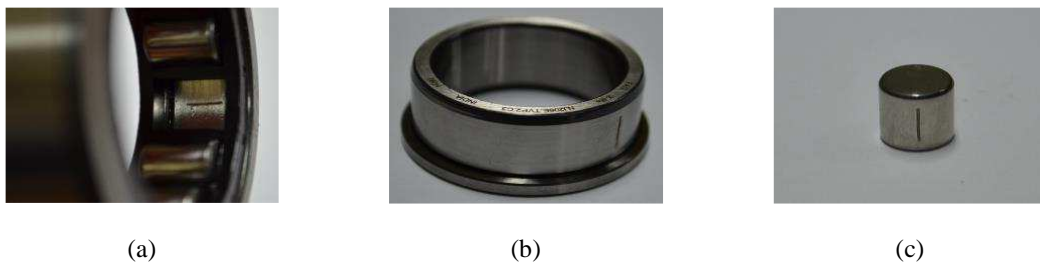


**Figure 2.10** The seeded bearing faults:  
 (a) Outer race way with a crack on its surface (ORCS); (b) Inner race way with a crack on its surface (IRCS); (c) rolling element with a crack on its surface (RECS).

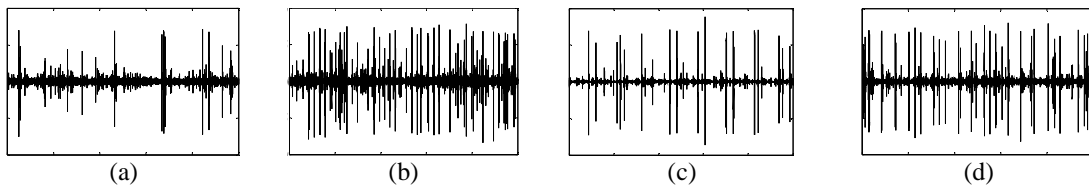


**Figure 2.11** The examples of AE signals for each bearing conditions listed as:  
 (a) The AE signal of healthy bearing; (b) The AE signal of ORCS; (c) The AE signal of IRCS; (d) The AE signal of RECS.

### 2.4 Experimental Results and Discussion

To validate the performance of Grad-CAM for bearing fault diagnosis, AE signals from healthy-state and three types of bearing fault are acquired using the testbed. The length of a measured AE signal is 1 second with a 1 MHz sampling rate and the number of AE signals for each condition is 600. The half of the data instances from the collected dataset were randomly selected for training the CNN. The remaining unseen samples were used for validating the fault diagnosis capabilities of the trained CNN. The trained CNN achieved 99% classification accuracy on the validation dataset, as shown in the confusion matrix depicted in Figure 2.12.

**Accuracy : 99.58%**

<b>Predicted result</b>	Healthy	<b>300</b>	4	0	1
	Outer race fault	0	<b>296</b>	0	0
	Inner race fault	0	0	<b>300</b>	0
	Roller fault	0	0	0	<b>299</b>
		Healthy	Outer race fault	Inner race fault	Roller fault
		<b>True result</b>			

**Figure 2.12** Confusion matrix of classification result

Figure 2.13 demonstrates the importance-weight over frequency component of envelope spectrum. As shown in the figure, the CNN learned that the harmonics of defect frequencies are the important information for classifying the states of the bearing. In this study, BPFO, BRFI, BSF, and the shaft speed are 44, 42, 65, and 8.33 Hz, respectively. For the healthy condition, CNN learned that low frequency band components are important since the low frequency band contains the harmonics of the shaft speed frequency that can be clearly observed in the healthy condition of the bearing. Since the defect and shaft speed frequencies are also valuable in traditional bearing fault diagnosis methods, it seems that the CNN have been trained without any fault-related information. In the case of outer race fault, the values of  $2 \times BSF$  and BPFO harmonics are too similar that makes it difficult to classify the input data based on these characteristic frequencies. Therefore, the CNN chose the sideband of BPFO as useful information instead of BPFO, itself.

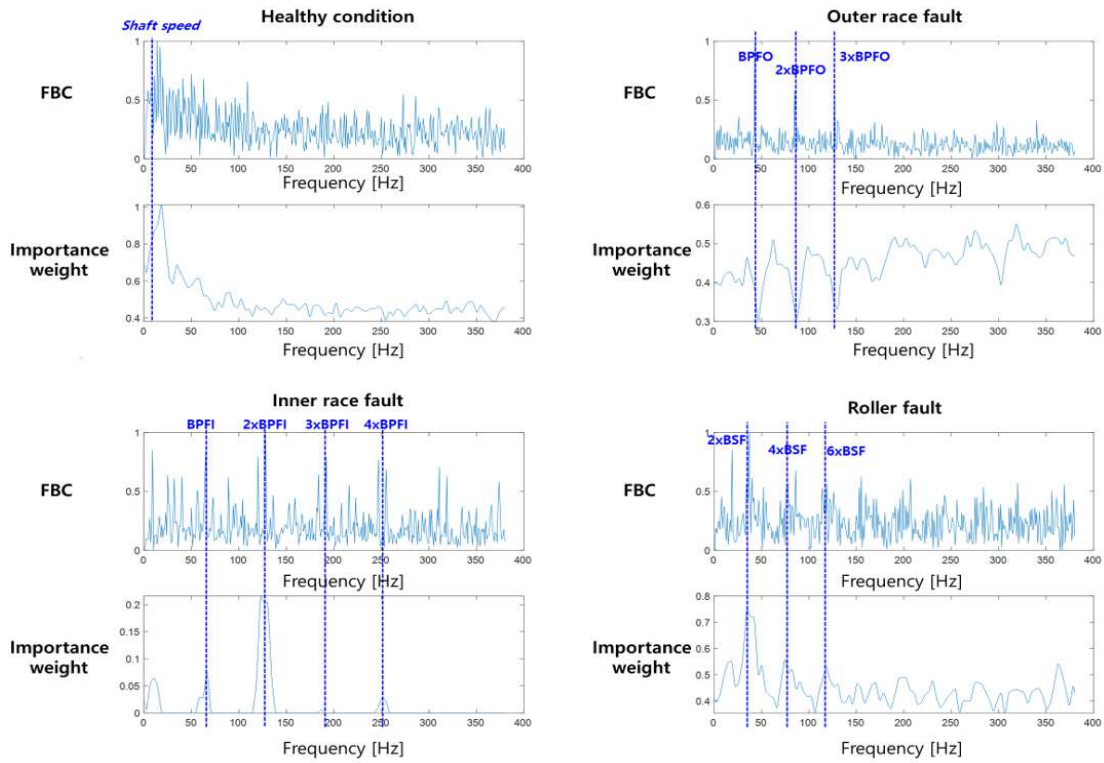


Figure 2.13 Importance weights from Grad-CAM for DNN

## 2.5 Conclusion

In this chapter, NBCC is introduced, which contains bearing characteristic frequencies for training CNNs when used for the task of rolling element bearing fault diagnosis. In addition, this research analyzed the feature representation of the trained CNN for bearing fault diagnosis using Grad-CAM technique. In the experiment, a custom simulator was used to imitate bearing faults. Using the bearing fault simulator, AE signals were measured for healthy state of the bearing and three different types of bearing faults such as outer race way, inner race way, and rolling element with a crack on their surface. In the experimental result, the CNN achieved 99% accuracy when trained with the proposed NBCC. The result also demonstrates that the low frequency components are important for classifying healthy state of the bearing, whereas bearing characteristic frequencies are essential for diagnosing various types of bearing faults. This result indicates that CNN trained with the proposed NBCC properly understood the valuable features of the envelop power spectrum for each bearing condition used in this work. For the application of CNNs in real environment, the proposed approach can be utilized to verify whether CNN learns inappropriate feature representation or not.

## **Chapter 3**

### **Deep Learning-based Bearing Fault Diagnosis using Stacked-Envelope Spectral Image of Acoustic Emission Signals**

#### **3.1 Introduction**

Rolling element bearing is widely used to various rotating machines, which reduces friction between dynamic components and static components. Since rolling element bearing is a vital component, the failure of rolling element bearing affects the operating condition of machines. Therefore, the fault diagnosis of rolling element bearing is extremely predominant to keep the system in effective and safe working state. The fault diagnosis techniques can be categorized to model-based, data-driven, hybrid approaches [8], [9]. The model-based techniques require mechanically well-established model which provides the failure characteristics of rolling-element bearing in terms of signal. Once the failure model is established by mechanical knowledge, no additional data is required. Also, the model-based method is very robust to diagnose rotating machines in various operating conditions if we input the parameters of target machines to the model [53], [54]. However, since it requires many expert-knowledges such as threshold, spectral analysis, characteristic frequency of components, etc., it is only suitable for professional users. Additionally, if the target machine has complex systems, it is too difficult to establish mechanical model because of many unknown parameters such as resonance frequency, external vibration from the other machines, vibration mode, unexpected state of the machine, etc. The hybrid approach is combined of model-based and data-driven based [55].

Specifically, the most case of data-driven methods utilizes machine learning algorithms with a large amount of data for training purpose. The strong advantage of data-driven methods is that they can establish the model of complex system without any priori mechanical knowledge. For this approach, the input data have an important role since it affects to the training process of the machine learning algorithms. Several techniques can be employed to collect the data for bearing diagnosis such as vibration acceleration [11], [12], the stray flux spectra [56], the induction motor's stator-current [16], and AE [14], [57]–[59]. For the low speed rotary

component as bearing, the AE-based technique is sensitive to the low energy impulse signal that release by a developing of crack in the bearing even it is subsurface [57], [60] so that the AE signal is found to be very useful for bearing fault diagnosis. Hence, this research collects the AE signal from bearing to diagnose incipient bearing defect. Then, machine learning trains the historical data which is measured by offline maintenance or online monitoring system. In general, machine learning-based data-driven method processes follow steps: 1) extracting features from measured data, 2) selecting informative features, 3) training historical data with selected features, 4) classifying new data using trained model. In order to extract relevant features, feature engineering is important process. However, it is difficult to verify the designed features are effective for bearing fault diagnosis.

Recently, DNN-based approach is one solution dealing with the feature engineering issue. DNN-based approaches output the comparable results to the traditional machine learning approaches by the using of end-to-end learning. This end-to-end learning can learn automatically discriminative representation features by training directly the raw input data, which could overcome designing relevant features. The alleviation of feature engineering helps the DNN have the computational efficiency and suitable for real-time application. Various DNN-based approaches have been researched to perform fault diagnosis, such as auto-encoder [59], [61], CNN [44], [62], transfer learning [63], [64], etc. However, the features extracted by trained DNN are difficult to be interpreted since they are calculated from raw signal with trained complex weight values. Accordingly, it is difficult to validate the generalized relationship between the features and bearing fault symptoms. Without such validation, the features could affect the accuracy of diagnosis if it is applied to the bearing dataset measured from different machines rather than trained target machine. Among the DNN techniques, the CNN become into prominence with its state-of-the-art power on the perceptual problem of visualization in 2D as image or video. To leverage the power and adapt to 2D-CNN, several studies try to find an 2D representation of AE signal. In [32], Tra et al. used energy distribution map for diagnosis of bearing defect. The bi-spectrum image is used to classify the faults in inconsistent working condition by Sohaib et al. in [65]. In [62] and [48], the authors segment the signal and stacked the segment to generate the vibration image. These 2D-representations of AE signal can give a high classification result for the collect data from the same system. However, they generate the different pattern image when applied to the other

system setup. Therefore, if the researchers using the collected data from one system to train the model and use the data from another system for testing even if they used the same type of bearing and rotation speed, the algorithm will be misclassified and gives low performance. To address this problem, the defect characteristic of bearing, which is seemed to be unchanged for different systems contain the same type of bearing and same operation speed.

In this chapter, a new method to find a 2-D-representation of AE signal is proposed based on the defect characteristic frequencies of bearing. This methodology generates SESI. Envelope spectrum could be utilized as a comprehensive data to diagnose bearing condition by observing bearing characteristic frequencies. The SESI, which is constructed from envelope spectrum of vibration signal and filtered by frequency range covering the bearing characteristic frequencies, is consider as the new signature for different type of faults in bearing and is used to input to the classifier. The author also proposed a structure of CNN for classification different type of bearing defect by learning and extracting the knowledge from the SESI. In experiment, this study compares the classification accuracy of proposed method and traditional methods using dataset measured on two different machines. To validate performance of feature learning, the method is trained for one machine and tested for the other machine without any retraining process.

The rest of this chapter is organized as follows. Section 2 explain details of proposed method for construct the SESI and CNN structure. Section 3 described the experimental setup to collect the dataset in two different machines of RK-4 testbed and laboratory designed testbed. After that, Section 4 presents the experimental result and discussion when applying the algorithm to analyze the datasets. Finally, the conclusion is given in Section 5.

### **3.2 Diagnosis methodology using the Stacked-Envelop Spectral Image and Deep learning algorithm**

The proposed method to convert the 1-D signal to 2-D SESI and deep learning structure consists of the following four steps. (Step 1) Envelope spectra are calculated from pre-acquired AE signals from the bearing datasets. (Step 2) Frequency magnitudes in the characteristic frequency range of the bearing are extracted as a vector of values. (Step 3) The

SESI image is construct based on stack the frequency magnitude vector in the same frequency range to create a matrix and convert the matrix' values to image pixels. (Step 4) CNN is trained using the extracted features and classification. The SESI of new AE signals are classified into healthy or faulty condition using the trained CNN.

### 3.2.1 Envelope analysis to construct stacked-envelope spectral images

Bearing faults, often relate to as a localized fault, such as crack or spall, is caused by long-lasting working factors, such as poor lubrication, overload, corrosion, material fatigue, etc. Bearing fault signals can be modeled as pseudo-cyclo-stationary and always contain series of short transients. The defect point on fault bearing generate periodic burst signals that are represented as the bearing fault signature frequency in the spectrum. The fault characteristic frequency is categorized as BPFO, BPF1, and BSF. Both outer race failure, inner race failure, and rolling element failure of the bearing cause BPFO, BPF1, and  $2 \times$ BSF, respectively. The bearing fault signature frequencies are calculates based on the geometric parameter and operation condition as follows [66]:

$$BPFO = \frac{N_{roll}}{2} \times Sp \times \left[ 1 - \left( \frac{D_R}{D_P} \times \cos \alpha \right) \right], \quad (3.1)$$

$$BPF1 = \frac{N_{roll}}{2} \times Sp \times \left[ 1 + \left( \frac{D_R}{D_P} \times \cos \alpha \right) \right], \quad (3.2)$$

$$BSF = \frac{D_P}{2D_R} \times Sp \times \left[ 1 - \left( \frac{D_R}{D_P} \times \cos \alpha \right)^2 \right]. \quad (3.3)$$

Here,  $N_{roll}$  is the number of rolling elements,  $Sp$  is the rotating speed of shaft,  $D_R$  is the rolling element's diameter,  $Pd$  is the pitch diameter, and  $\alpha$  is a contact angle of the rolling element with respect to the shaft. Consequently, the bearing signature frequency will generate the high peak in the frequency spectrum. If the authors stack the frequency spectra with the same frequency range and convert the matrix value to image pixels, the SESI is obtained with the pattern of strikes respect to the defect frequency positions. For different types of fault, the different pattern can be obtained and the SESI shows a valuated representation of 1-D signal in form 2-D images.

However, these cyclic impulses are generated in the low-frequency domain, and they are amplitude-modulated to higher frequencies, that results the difficulty to observe them in the frequency spectrum with normal fast Fourier transform. Because of the modulation phenomenon, envelope analysis with Hilbert transform is employed as the demodulation technique to isolate the periodic burst signal of bearing fault from the carrier signal. First, the long-length signal is segment to smaller segments which both help to reduce the time for signal processing and increase the number of data sample. By this way, each original sample signal will generate a set of segments and each segment gives an envelope spectrum. The stacked process of the envelope spectra from segments creates an image. So that, each original sample signal will generate one SESI. Moreover, instead of segment the signal side by side as in many researches as [62], [67]. The research proposed a new method to make a segment based on sampling process.

The basic of this method is depicted in Figure 3.1 as below. Assume the original signal is segmented to  $M$  -segments. For each segment  $i^{th}$ , with  $i=1..M$ , the sequent of segments is construct as follow:

$$s(i) = [x(k), x(M + i), x(2M + i), \dots, x((k - 1).M + i)], \text{ with } k = 1..M \quad (3.4)$$

By this way, each segment is created by sampling the original signal at different start point. Therefore, all the data points from the original signal can be used and the loss of information can be reduced.

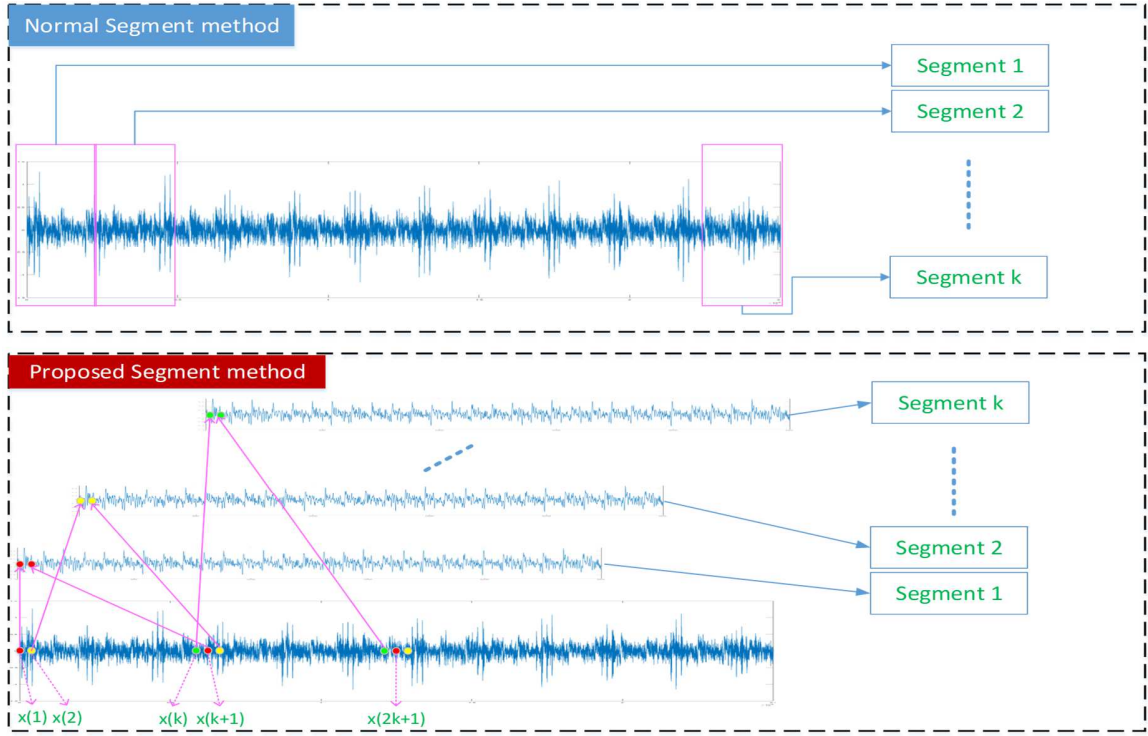


**Figure 3.1** The proposed method for segment data

Since the cyclic impulse signals from bearing failures are amplitude-modulated, AE signals are demodulated to extract pure burst signals from the bearing fault. In this study, Hilbert transform-based (HT) [14], [59] envelope analysis is used for demodulation of the AE signal. First, the HT is applied to the AE signal as follows:

$$\hat{x}(t) = \frac{1}{\pi} \int_{-\infty}^{+\infty} \frac{x(\tau)}{t - \tau} d\tau \quad (3.5)$$

where  $x(\tau)$  is a signal at time  $\tau$ , and  $\hat{x}(t)$  is the HT signal at time  $t$ . Then the analytical signal,  $z(t)$ , is calculated from the HT signal  $\hat{x}(t)$ , and input signal  $x(t)$  by combining in a form of complex numbers  $z(t) = x(t) + j\hat{x}(t)$ , where  $j^2 = -1$ . Then, the envelope signal,  $e(t)$  with instantaneous amplitude is computed as the modulus of  $z(t)$ , with  $e(t) = |z(t)|$ . Finally, the envelope spectrum is calculated as the square root of the fast Fourier transform of  $e(t)$ .

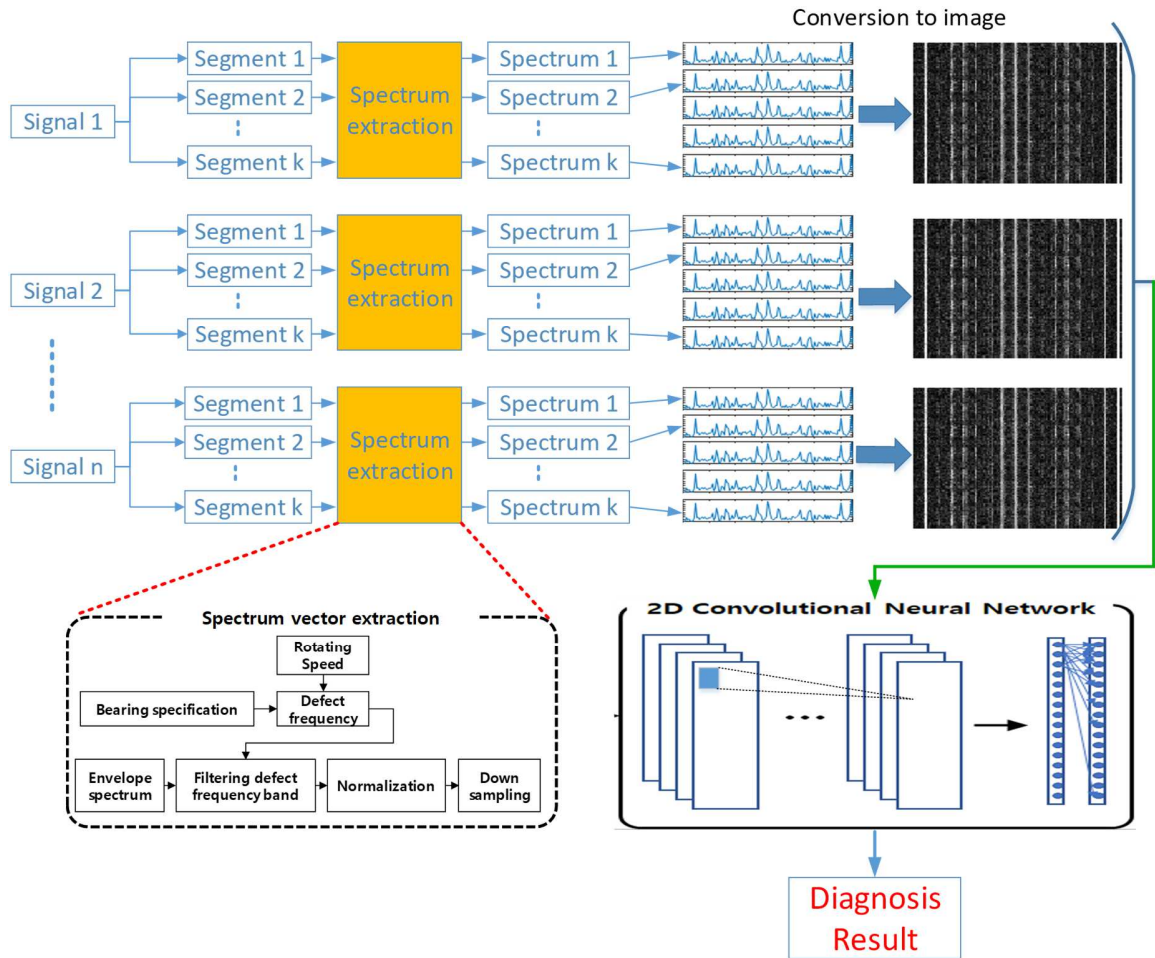


**Figure 3.2** The overall scheme of SESI extraction and CNN classification

Figure 3.2 shows the overall process of the proposed methodology. After the envelop spectrum is extracted, the defect frequency band filtering help to limits the frequency range by using the defect frequency values. The defect frequency range is chosen to ensure the first three harmonic of each defect frequency locate inside this range. Then, the envelop spectrum is normalize and down-sampling to suitable to the pre-define size of image before stacked in matrix and convert to SESI. Finally, the images are input to the CNN classifier to separate different type of fault.

### 3.2.2 Training CNN structure for classification

The convolution neural network has demonstrated the powerful in processing 2D-pixel images for its capability when using the convolutional operation. As the state-of-the-art performances, CNNs have become the de-facto standard in computer vision field with different tasks such as image recognition and object detection. It is used to automate the process of feature extraction and feature selection for a given set of data. This network generates an optimal use of the indigenous connections (instead of the multi-layer perceptron), weight distribution to achieve invariance of scaling, shifting or distortion of the input images [44], [68]. To classification the bearing fault's types, the CNN includes a feature processing and a fault condition classifier. The feature processing seeks to automatically extract and select features, and the fault condition classifier recognizes fault conditions using the extracted features. In this study, the feature processing includes several convolution blocks, in which each block contains a convolution layer, a batch-normalization layer, and a leaky rectified linear unit (leaky-ReLU), in sequence. And fault condition classifier is constructed by last fully connected layers.

Typically, in the convolution block, the convolution layer are variants of multi-layer perceptron, with the difference that the convolution layer's learnable parameters are constructed as a set of filters. The filter convolves with the input pixels to get feature map at the output. The forward pass of convolution layer  $l$  in  $C^{th}$  channel operation can be described as  $o_C^l = \sum_{k=1}^{C^{l-1}} W_{k,C}^l \circ x_k^{l-1} + b_C^l$ , where the ( $\circ$ ) operator denote the 2D convolution between the input  $x_k^{l-1}$  and the kernel filter  $W_{k,C}^l$ , and  $b_C^l$  is the bias parameters of the  $C^{th}$  channel in layer  $l$ . The two main advantages of convolution layers, compare with using fully connected layers, are local interconnection and sharing of parameters. Local interconnection forces the model to consider the spatial structure of the data through a sparse local interconnection pattern between neurons of adjacent layers. Sharing of parameters indicates the fact that all the neurons in the same feature map share the same set of parameters, that allows features to be detected regardless of their positions in the input image, thereby constituting the characteristic of translation invariance. Moreover, through the convolution mechanisms, the number of parameters to be learn can significantly be reduced compare with other fully connected structure. The forward process of convolution block  $l$  is described as below:

$$\begin{aligned}
 o_1^l &\leftarrow \text{conv}(x^{l-1}, \theta^l) \\
 o_2^l &\leftarrow \text{batchnorm}_{\gamma, \beta}(o_1^l) \\
 o^l &\leftarrow \text{leakyReLU}(o_2^l)
 \end{aligned} \tag{3.6}$$

Where  $\theta^l = (W^l, b^l)$  is the weight and the bias need to be learned. Then, all the convolution layers are followed by the batch normalization to make an improvement of convergence process in the training phase while avoiding the regularization requirement which is found in other machine learning algorithms. The batch normalization also helps regularize the model so that the network does not need to employ the dropout method to avoid overfitting. Batch normalization is achieved through a normalization step that fixes the means  $\mu_B = (1/m) \sum_{i=1}^m (o_1)_i$  and variances  $\sigma_B^2 = (1/m) \sum_{i=1}^m ((o_1)_i - \mu_B)^2$  of each layer's inputs with  $m$  is the size of mini-batch. Each dimension of the input will be normalized separately. The output of normalize layer can be obtained by:

$$\begin{aligned}
 (\bar{o}_1)_i &\leftarrow \frac{(o_1)_i - \mu_B}{\sqrt{\sigma_B^2 + \varepsilon}} \\
 (o_2)_i &\leftarrow \gamma(\bar{o}_1)_i + \beta
 \end{aligned} \tag{3.7}$$

Here,  $\varepsilon$  is an arbitrarily small constant;  $\gamma$  and  $\beta$  are the parameter which are subsequently learnt in the optimization process. Finally, the convolutional block gives the output by substitute  $o_2$  to the leaky rectified linear unit which has the form of

$$\text{leakyReLU}(x) = \begin{cases} x, & \text{if } x \geq 0 \\ 0.01x, & \text{otherwise} \end{cases} \tag{3.8}$$

In this study, the network down-samples the input image by the factor stride (i.e., the factor by which the output of the layer is smaller than the input signal of the network) through the convolution step instead of using the pooling layer. This approach shows a better performance when extract the features of image in a deep network [69], [70].

During forward propagation process over several alternated convolutional blocks, the valuable features of input data are extracted, and then feeds to the fully connected layers and

soft-max role classification are the last layers, by which the classifying task is mainly realized. To obtain a well-performed CNN, cross-entropy is used as the loss function, and Adam optimization is used for backpropagation to train the parameters of the network. The optimization strategy seeks to minimize a cost function, which calculate the mismatch between the predictions from the network and the ground true labels for a set of data.

Before the CNN is trained on the set of data samples, the hyperparameters of the model such as the number and size of kernel filters in each convolution layer, and the number of fully connected layers and neurons, batch-size, learning rate, etc., are need to be specified, that defines a hypothesis space. Following some general design principles, the proposed CNN model is initially made as simple as possible to ensure the generalization ability and computational efficiency. The structure of the CNN is represented in Figure 3.3.

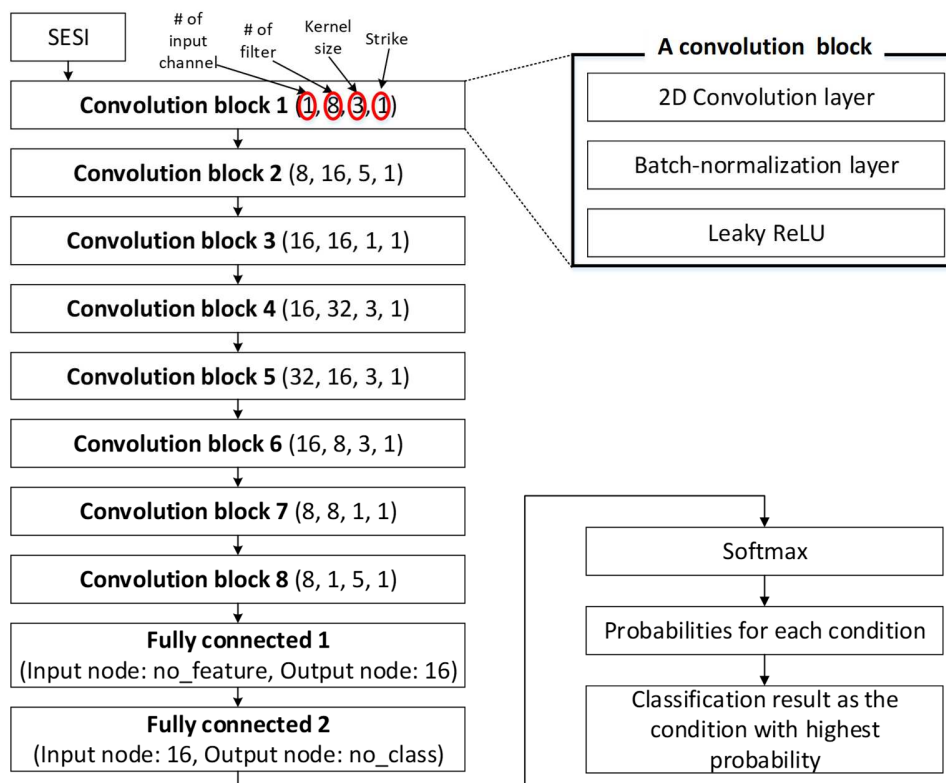


Figure 3.3 CNN structure for bearing fault diagnosis

### 3.3 Experimental Setup and Data Acquisition

To validate the proposed method, a bearing fault simulator is used for measuring healthy and

faulty-state AE signals of the bearing. Two testbeds were used to collect the AE data from bearings. The detail setup of two testbeds is present below.

### **3.3.1 Rotorkit testbed dataset**

The established bearing fault simulator using the rotor-kit RK-4, which is design by Bently-Nevada Asset Condition Monitoring, is illustrated in Figure 3.4. The RK-4 closely simulates actual rotating machine behavior by permitting the researchers to isolate and control individual machine characteristics and make it useful as a laboratory device for theoretical research. On the V-frame, a motor is connected to rotate only one shaft by a coupling. During the experiment process, a key phase sensor was installed near the shaft to acquire the tacho signal which shows the rotating speed. The motor of RK-4 can closely hold the desired speed when loading conditions changes. This operation is executed by incorporating a direct current motor with high-performance control circuitry. A cylindrical roller bearing (FAG NJ206-E-TVP2), which is the target bearing of the experiment, is installed in the bearing housing of the shaft. The shaft speed is 1800 RPM in this research. The radial load of 800-gram disc is applied to the shaft. Both AE and vibration sensors are attached on the bearing housing of the target bearing as depict in Figure 3.4. The RK4 testbed permit to simulate and measure the signal from both normal and faulty condition with low level of mechanical noise by minimizing the vibration from its other components.

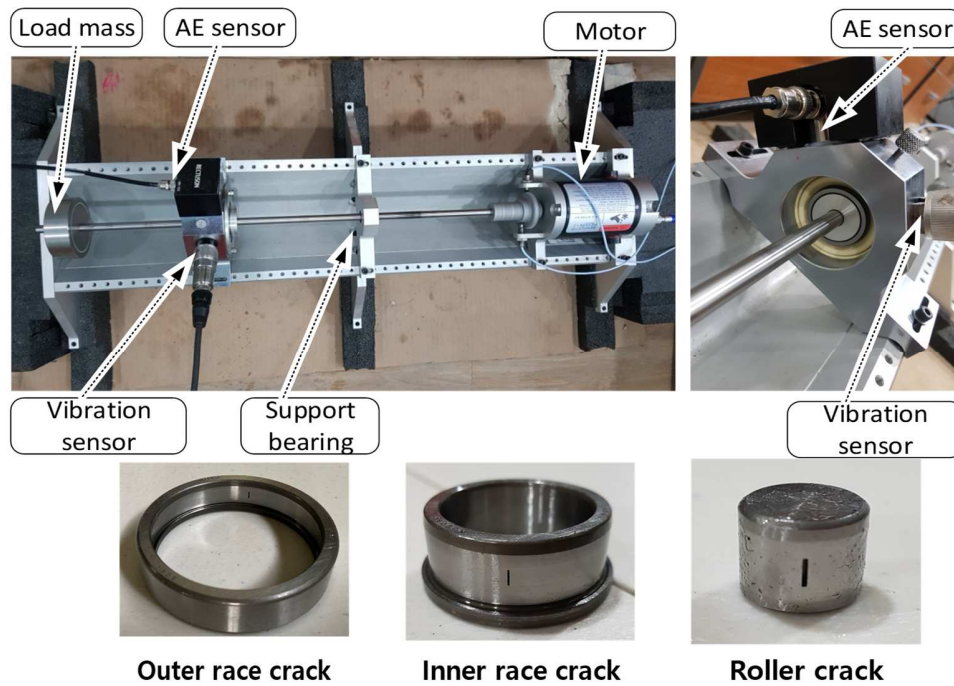


**Figure 3.4** The rotorkit testbed setup

### 3.3.1 Laboratory designed bearing testbed dataset

In the reality industry, the AE signal is strongly affected by the environment which include the noise from motor or the vibration of other devices. Therefore, the collected signal from sensors not only contain the faulty signal from bearing but also the unexpected components from environment. In addition, the industrial fault signal from the real machine is difficult to obtain because of security reasons. Consequently, the laboratory constructs an elaborate experimental apparatus to mimic the working condition in factory. The detail installation of this testbed is depicted in the Figure 3.5. The testbed contains a three-phase motor to drive the main shaft through the belt. On the main shaft, two target bearing housing is install in both sides. Both the axial and radial load is applied to the bearing by hydraulic system. The load was kept constant of 100 kgf for both axial direction and radial direction. The shaft is rotated at constant speed of 1800 rpm during the measuring time. The same bearing type (FAG NJ206-E-TVP2) was used as in the RK-4 testbed. The AE and vibrations sensor were attaches on the bearing house.

In both experiments, the measurement device for collecting AE signals is a NI 9234 Data

Acquisition (DAQ) device [71]. A general-purpose wideband AE sensor in type of R15I-AST [72], whose frequency response is between 50Hz and 400 kHz, is used to capture resonance frequency signals containing modulated bearing signals. The vibration signal is measured by PCB-622B01 piezoelectric sensor [73]. The detail of data acquisition system is detailed in the Table 3.1 below:

**Table 3.1** Details of data acquisition system

Devices	Detailed specification
NI 9234 DAQ	<ul style="list-style-type: none"> <li>- IEPE signal conditioning with AC coupling (2 mA)</li> <li>- Operating condition: -40 °C to 70 °C operating, 50 g shock, 5 g vibration</li> <li>- Resolution: 24-bit</li> <li>- Dynamic range: 102 dB</li> </ul>
R15I-AST	<ul style="list-style-type: none"> <li>- Peak Sensitivity (Ref in V/<math>\mu</math>bar): -22 dB</li> <li>- Resonant Frequency (Ref in V/<math>\mu</math>bar): 150 kHz</li> <li>- Operating Range: 50-400 kHz</li> </ul>
PCB-622B01	<ul style="list-style-type: none"> <li>- Sensor sensitivity: (<math>\pm 5\%</math>) 100 mV/g</li> <li>- Frequency Range: 0.2 to 15000 Hz</li> <li>- Measurement Range: <math>\pm 50</math> g (<math>\pm 490</math> m/s<sup>2</sup>)</li> </ul>

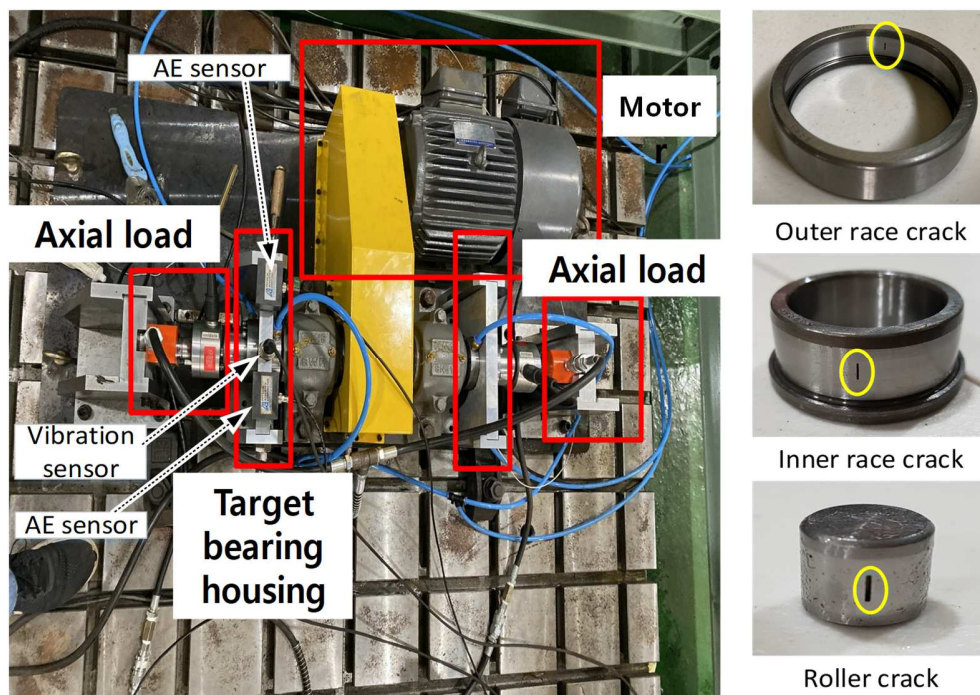


**Figure 3.5** The laboratory designed testbed setup

### 3.4 Experimental Results and Discussion

To validate the performance of SESI extraction for bearing fault diagnosis, AE signals from healthy-state and three types of bearing fault are acquired using the testbeds. The length of a measured AE signal is 1 second with a 256 kHz sampling rate. The AE signals for each condition is continuously measured for 5 minutes. 80% of the dataset is selected randomly for training the CNN. The remaining 20% of the dataset is used for testing.

#### 3.4.1 Effectiveness of the algorithm on RK-4 testbed dataset

Figure 3.6 illustrates the result of the proposed algorithm to the AE signal which is collected from the RK-4 testbed. The extracted SESI from the AE signal is shown in Figure 3.6 (a). Each image has the size of  $25 \times 403$  pixels. The important frequency for each type of fault are shown as the strikes in the image. The normal signal generates an image with the appearance of edge and blob pattern in random position. This image represents as the background noise when the peaks appear randomly in the frequency spectrum. Compare to the faulty signal, the faulty images show the strike at certain location which respect to the defect frequency. For different type of fault, the defect frequency peaks appear at different position in the spectrum. Figure 3.6 (b) depicts the result of classification algorithm which the total average accuracy

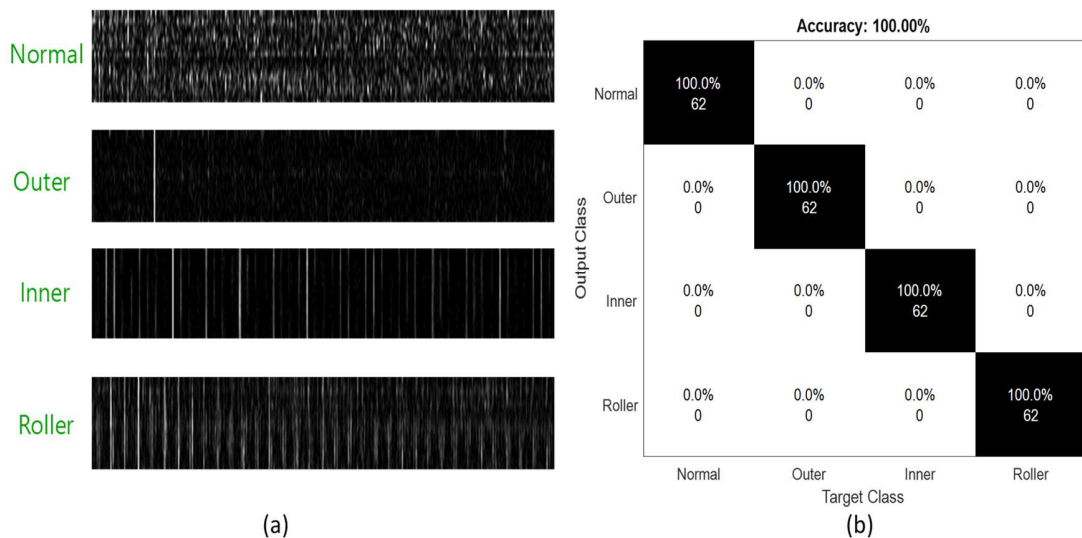


**Figure 3.6** The result of the proposed method for RK-4 testbed dataset

(a) SESI for different type of AE signal (b) Confusion matrix of classification

of 100%. The result shows characteristic bearing frequencies are important for classification of the AE signals from bearing failures.

### 3.4.2 Effective of the algorithm on laboratory designed bearing testbed dataset

The laboratory testbed is designed to mimic the operating condition in the industrial environment. So that the signal from this testbed contains a large amount of noise signals which is mostly from other device such as the motor, the pump to drive oil for lubrication. Therefore, in all of the generated image contain more noise with the random blob and edge. However, the heavy load from both axial and radial direction help to increase the vibration amplitude. This effect makes the first three harmonic in the case of outer raceway fault can be easier to observe in the SESI as in the Figure 3.7 (a). In addition, the image with noise effect reduce the accuracy classification when some of patterns between different signals can be confused. Consequently, the average accuracy decreases in the case with AE signal from laboratory testbed with 99.60% of average accuracy.

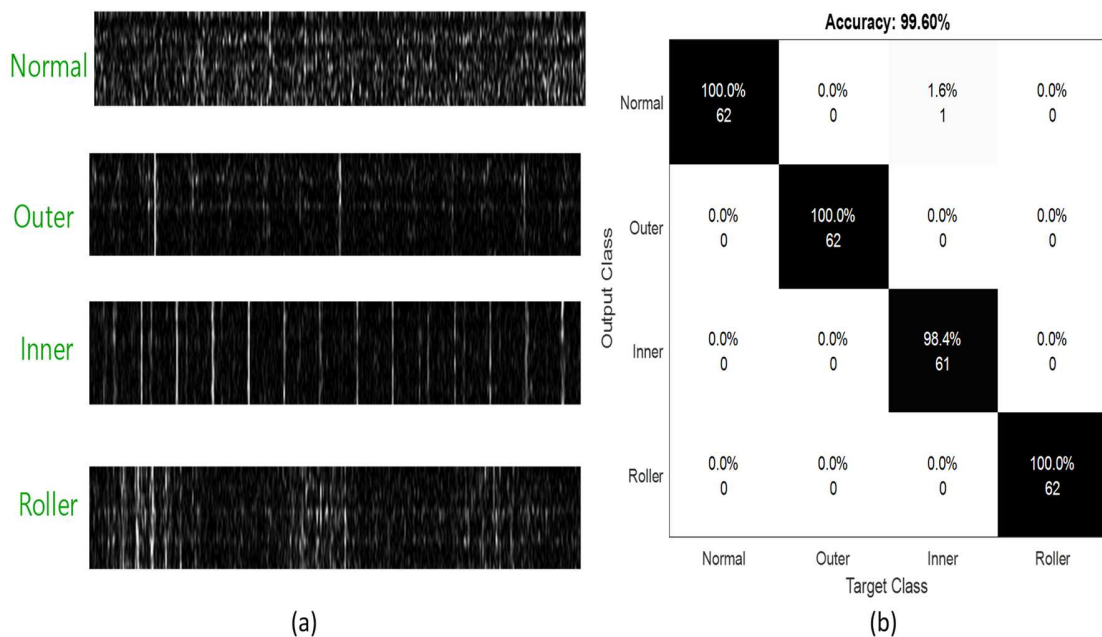


**Figure 3.7** The result of the proposed method for laboratory testbed dataset  
 (a) SESI for different type of AE signal (b) Confusion matrix of classification

### 3.4.3 Effective of training and testing with different datasets

To demonstrate the effective of the proposed algorithm, the research applies the algorithm with different training and testing datasets. There are two scenarios which is proposed respect to two datasets which is described above in section 3: (1) using the dataset from laboratory testbed for training and the RK-4 dataset for testing; (2) using the RK-4 dataset for training and the laboratory testbed dataset for testing. The result is described in Figure 3.8 and Figure 3.9 as below.

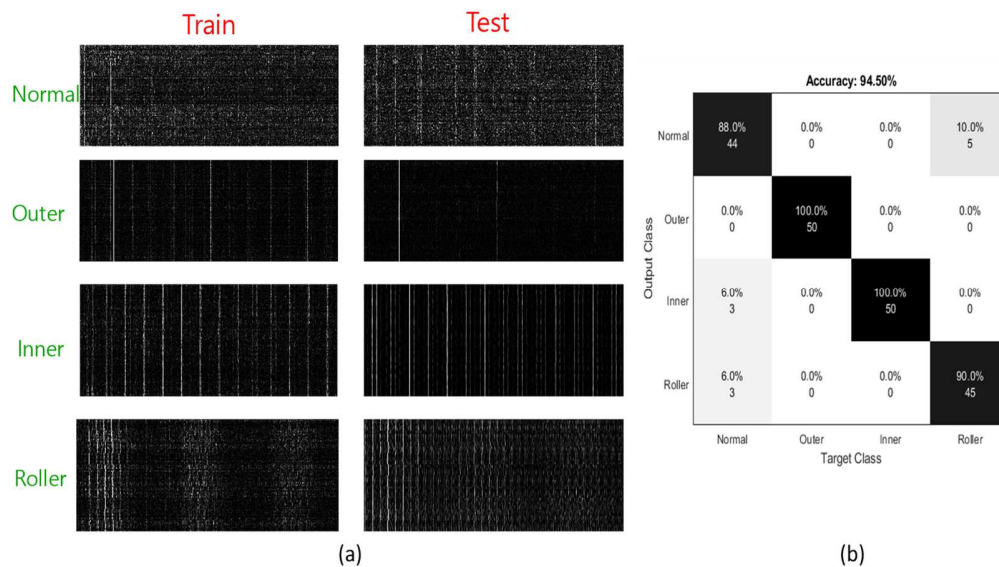


**Figure 3.8** The result of the proposed method for the scenarios (1) test:

(a) SESI for different type of AE signal (b) Confusion matrix of classification

Figure 3.8 depicts the result of using the laboratory testbed bearing dataset for training and the RK-4 testbed bearing datasets for testing. The result illustrates a high accuracy classification of classification with 94.50% of average accuracy. However, there are still some misclassification between the normal class and roller class which is cause by the background noise affect to the pattern of roller fault case as shown in the Figure 3.8a.

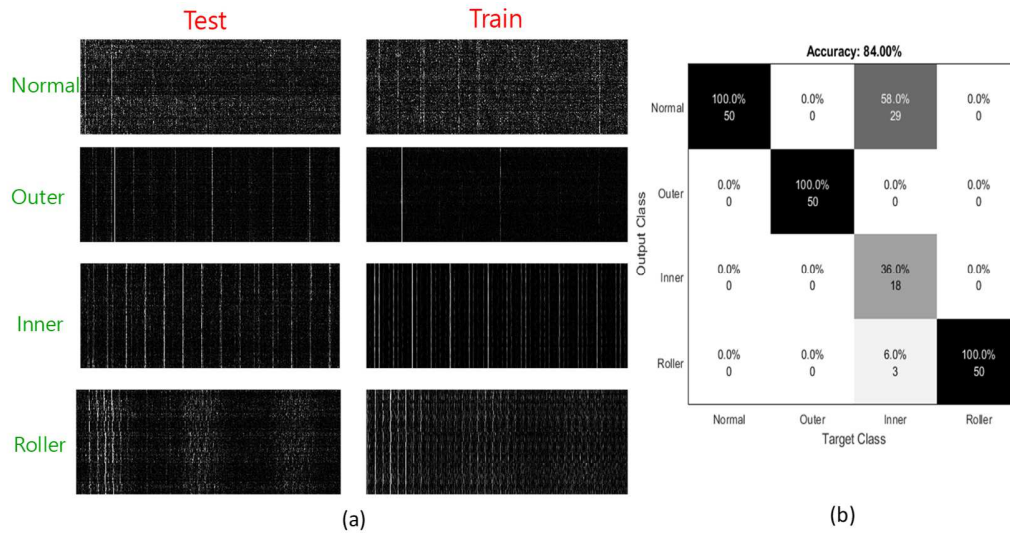


**Figure 3.9** The result of the proposed method for the scenarios (2) test:

(a) SESI for different type of AE signal (b) Confusion matrix of classification

Similarly, Figure 3.9 shows the result for the second scenario. The result in Figure 3.9b show the accuracy of the algorithm with 84% of average accuracy. The most misclassification occurs between inner class of laboratory testbed dataset. This happens because the effect of the high level of noise that blur the strike in the inner pattern of the laboratory testbed testing dataset, and it make the algorithm confuse with the normal case of training dataset from RK-4 testbed. Figure 3.10 below show an example of the inner testing sample is blurred by affecting by noise.

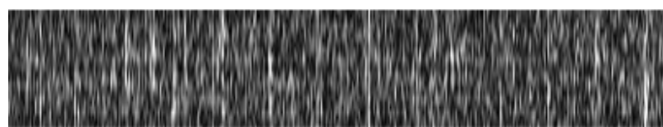


**Figure 3.10** Example of inner SESI which is blurred by high level of noise

Compare with the scenarios (1) in the specific case of inner fault, when the training data using the laboratory testbed dataset, the set of generated images from the AE signal with different level of noise that will include both the clean images with the low level of noise and the blur images with the high level of noise. The testing images from the Rk-4 testbed, which is form laboratory environment and has the lower level of noise, can be easy to recognize by the algorithm. So, it gives the result with better accuracy. However, for the second scenario

when the training with the clean signal from RK-4 testbed, the training model cannot cover all cases of images. And it will misclassification when the image with high level of noise, that look similar as the normal case than the fault case, is used for testing. Consequently, the result in the second scenario is lower. In addition, the proposed algorithm shows its ability for using its knowledge which is extracted from one system and apply to another system for fault diagnosis based on the less changing of bearing characteristic frequencies. These properties make the SESI like to be unchanged for difference systems which contain the same types of bearing.

For illustration, the proposed method with SESI is compared with the vibration image, another algorithm to convert the 1-D signal to 2-D image. This algorithm is also applied by [62], [67]. The extracted vibration image for different type of AE bearing signal from the two datasets, which is described in section 3, is show in Figure 3.11. And the results of classification are described in Table 3.2. The two methods are compared in three scenarios: (1) only use the RK-4 dataset for training and testing; (2) only use laboratory testbed dataset for training and testing; (3) use the laboratory testbed dataset for training and RK-4 dataset for testing.

As illustrated in Figure 3.11, the vibration images show different patterns for different dataset with the same type of defect signal. Thus, the classifier is misclassification in most the

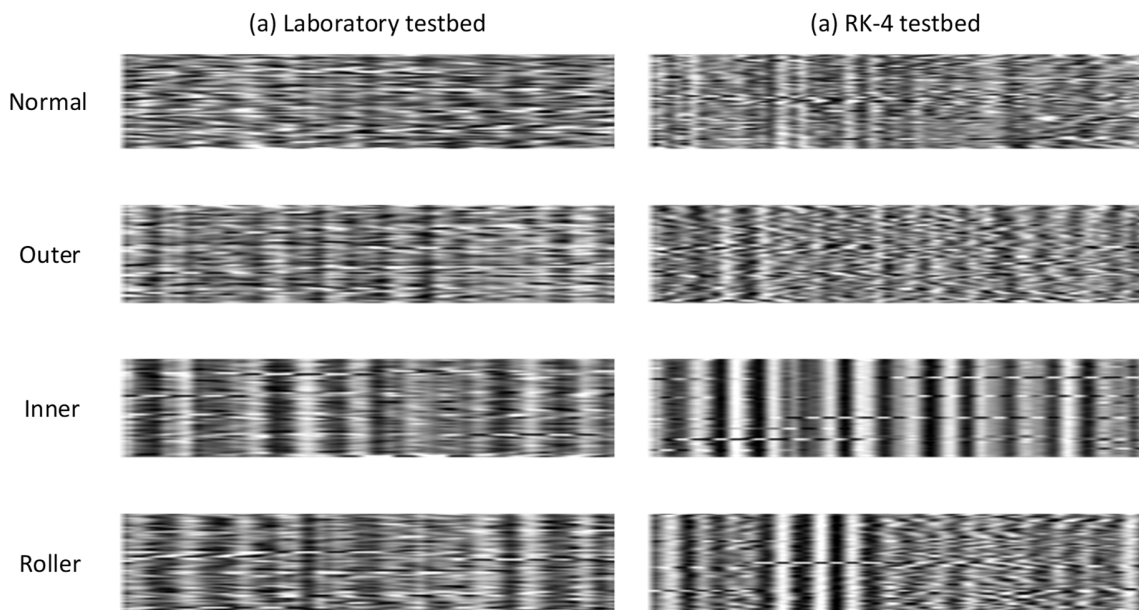


**Figure 3.11** Vibration image from the RK-4 dataset and Laboratory testbed dataset

cases when using one dataset for training and test with another dataset. On the other hand, the proposed method with SESI show a significant high accuracy in this case with the difference in training and testing datasets compare to the vibration image. Moreover, the proposed method with SESI also outperformed to the vibration image method even in other two scenarios when the training set and testing set belong to the same dataset.

**Table 3.2** Classification result of the proposed method compare with vibration image method

Scenarios	Type	SESI method	Vibration image method
(1)	Normal	100%	100%
	Outer	100%	100%
	Inner	100%	75%
	Roller	100%	95.8%
	<b>Average accuracy</b>	<b>100%</b>	<b>92.71%</b>
(2)	Normal	100%	95.80%
	Outer	100%	100%
	Inner	98.40%	100%
	Roller	100%	95.80%
	<b>Average accuracy</b>	<b>99.60%</b>	<b>97.92%</b>
(3)	Normal	88%	62.50%
	Outer	100%	0%
	Inner	100%	16.70%
	Roller	90%	91.70%
	<b>Average accuracy</b>	<b>94.50%</b>	<b>42.70%</b>

### 3.5 Conclusion

Rolling element bearing is vital component of rotating machinery. Bearings reduce the friction of the rotating body and fix the position of the mechanical parts. Since rolling element bearing is a necessary component, the failure of rolling element bearing affects the operating condition of machines. Therefore, the fault diagnosis of rolling element bearing is extremely predominant to keep the system in effective and safe working state. In this study, a new method to find a 2-D representation of AE signal is proposed based on the defect characteristic frequencies of bearing. This methodology generates SESI. The SESI, which is constructed from envelope spectrum of vibration signal and filtered by frequency range covering the

bearing characteristic frequencies, is considered as the new signature for different types of faults in bearing and is used as input to the classifier. The author also proposed a structure of CNN for classification of different types of bearing defects by learning and extracting the knowledge from the SESI. In experiment, this study compares the classification accuracy of the proposed method and traditional methods using a dataset measured on two different machines. To validate the performance of feature learning, the method is trained for one machine and tested for the other machine without any retraining process. 80% of the dataset is selected randomly for training the CNN, and the remaining 20% of the dataset is used for testing. Furthermore, in the cross-testbed experiment in which one testbed dataset is trained and another testbed's dataset is classified, the proposed method achieved high performance compared to the conventional signal-image-based CNN algorithm. In particular, in the experiment of learning the dataset of the laboratory-designed testbed and classifying the dataset of the RK-4 testbed, the existing algorithm achieved 42.7%, while the proposed algorithm achieved 94.5%. Therefore, the proposed method is expected to achieve generalized bearing diagnostic performance for various rotating machines.

## **Chapter 4**

### **A Deep-Learning-based Bearing Fault Diagnosis using Defect Signature Wavelet Image Visualization**

#### **4.1 Introduction**

Indisputably, rotary machinery is broadly utilized across production industries such as in power systems, petrochemicals and means of transportation due to its low cost, rugged high efficiency under a heavy load, reliability, and robust design. Generally, the consequence of rotary machinery obliged to operate for prolonged periods under harsh-condition environments is wear and tear, which is associated with mechanical stresses, which can lead to unexpected failure in bearings and gears, which are crucial components in a rotary machine. Such failures could lead to economic losses or human casualties. As a consequence, the machine's health supervision and fault analysis are vital integral elements of the maintenance procedure in industrial manufacturing. A robustly conditioned monitoring procedure can improve productivity, reduce maintenance expenses, and enhance reliability and safety.

While gear and bearing faults commonly betide the rotary machine, bearing faults prevail in occurrence. Industrial statistics illustrate that 40% of total large machine breakdowns happened due to broken bearings while for small machines, the analogous number reaches up to 90% [74]. Therefore, real-time monitoring and fault diagnosis methods for rolling element bearings have accrued considerable attention from researchers in recent years. Normally, there are three primary categories for fault diagnosis methods including reactive, preventive, and predictive maintenance [75]. Fault diagnosis methods can also be categorized as data-driven-based (knowledge-based), model-based, and hybrid-based with the hybrid-based method considered as the combination of one or several methods of model-based and data-driven-based [76]–[78]. In model-based fault diagnosis, the bearing system is analyzed by constructing an equivalent mathematical model that describes the differences between the normal state and fault states; however, the model-based method can be complicated by the increasing non-linearity of the system. The computational cost increases when the complexity of the system increases [79], [80]. Data-driven-based methods are based on measurements taken over time and with data analysis to yield an assessment about the physical state of the

machine [81], [82]. With the developments in acquisition devices and sensors, communication technology, availability of data such as big data and cloud computing, and effective data processing methods, data-driven-based fault diagnosis has emerged as the most suitable fault diagnosis option.

Bearing fault data can be acquired from acoustic emission measurements, ultrasound, vibration, temperature, thermal images, and current sources, all of which are extensively applied for investigation. Previously, fault analysis by vibration signals attracted more attention for supervising the health of the machine thanks to its potential to transmit the intrinsic information of the rotary machine. Using acoustic emission (AE) signals for fault diagnosis offers some advantages over the vibration signal when applied to rotary machines. For instance, the vibration-based signal is susceptible to presenting degradation of bearings at low rotation speeds, and the signal is not appropriate to detect and isolate faults that are still in the incipient stage. To identify damage before it manifests in the form of small cracks on the metal surface, AE signal-based methods have proven to be effective at comparatively low speeds.

The classification or identification of a fault is impossible when analyzed from the raw fault data. With a diversity of signal processing methods, raw sensor data are processed to extract the information that correlates to the faults. Some well-established approaches for signal processing are analysis with time-domain techniques, frequency-domain techniques, and time-frequency-domain techniques. The algorithms based on signal analysis are inessential to constructing an equivalent mathematic model, so that the performance of the algorithm instead depends largely on the data from different operational conditions of the system. The root mean square, kurtosis, and other high-order statistics moments are some of the popular features often used in time-domain analysis. In addition, Do et al. [83] and Wen et al. [84] suggested a method to efficiently extract features of the faults in a bearing with the vibration image. They converted a segment of time-domain vibration signals into 2-D gray-scale images and got the local texture features from these images by using a transform with a scale-invariant feature. Nevertheless, as the AE signals of a bearing may contain some noise component, such as sensor noise or random environment peaks, the approach using only time-domain characteristics for transforming the vibration signals into 2-D images is not adequately robust

to represent the characteristics of the faults. To tackle this problem, this study proposes a more reliable 2-D representation of the AE sensor signals for high accuracy in recognizing the bearing faults. On the other hand, fast Fourier transform (FFT) and other high-order spectral analyses are generally used in frequency-analysis. In [85], Tra et al. used energy distribution map, and in [86], Sohaib et al. used bi-spectrum as the image representations in 2-D. These representations can illustrate the discrimination between different types of faults in bearings, but they did not show the relation between the image and the fault signature of the bearing. For a signal with natural non-stationary state, which is common, frequency-processing methods are not broadly relevant because of their lack of capacity to disclose the intrinsic information. In general, the rotary machine is constructed from different non-stationary components since the operating environment always varies and faults also vary. Thus, it is crucial to analyze the signals with non-stationary characteristics with the assistance of several time-frequency-analyses, for example, the S-transform [87], [88], the short-time Fourier transform [89], [90], and the wavelet transform [91]–[93]. Employing these techniques yields both the time- and frequency-knowledge needed for the investigation. Due to its exclusive properties, wavelet analysis is frequently used for processing the non-stationary signals in the faults of bearings to localize the faults and determine the crack sizes in different components and structures. To extract features for fault recognition, many studies have reported successful use of the wavelet decomposition. Although many variations of wavelet technique exist, it is important to select a satisfactory wavelet to discover the best matching and give the most appropriate representation for bearing faults. If a crack or spall appears on a contact surface between any components in a bearing, an impact is created when the ball or roller hits the defect, which leads to a peak transient response impulse with damped oscillation at the tail. Since the bearing rotates at a constant speed, the periodic impulse behavior contains important information regarding bearing health. So, exploiting the transient response and meticulously analyzing the signal can effectively predict the early state of bearing faults. These transient responses appear periodically and generate peaks at particular frequencies in the spectrum of the AE signal. The particular frequencies include BPFO, BPFI, and BSF [81], [94]. Determination of the frequency range in which to observe the signal from these particular frequencies allows enhancement of the fault diagnosis algorithm. In this study, a reliable image extraction scheme relating to the characteristic frequencies range in the wavelet

representation is employed to generate robust and more effective features of the rolling element bearing faults.

Subsequent to transforming the AE signals into a compact relevant 2-D representation, the images serve as input of a classifier to generate the decision making. Recently, machine learning-based methodologies for fault analysis have become prevalent and powerful algorithms in the field of bearing health monitoring since they have the capacity to gain valuable knowledge from the considerable amount of recorded data already extant. Among the various processes, K-NN [81], SVM [82], and ANN [95] are popularly implemented for fault detection. Deep learning approaches have recently been considered a new branch of application for fault diagnosis. The deep learning algorithm comprises multiple stages of non-linear operation and shows an ability to automatically learn up to high-abstract features to more intelligently support decision-making. Deep learning algorithms such as CNN [96] and stacked auto-encoders [97] have been investigated in fault detection. Thus, our research also aims to design and employ a deep and capable CNN architecture to obtain high accuracy for bearing fault diagnosis.

The specific contributions of this chapter can be summarized as follows:

- 1) To alleviate the limitations of previous methods used for transformation of 1-D signals into 2-D images, a novel 2-D representation method is created by combining the envelope analysis and continuous wavelet transform (CWT) with filtering by the frequency range covering the bearing defect frequencies to generate DSWI. The constructed DSWI is considered as the new signature, which solves the modulation problem, reduces the nonstationary effect in the signal, demonstrates the distinct patterns for the different types of faults in bearings, and closely relates to the defect frequencies in the envelope spectrum.
- 2) This study also introduces a specific architecture of CNN for classifying multiple fault types that occur in bearings by learning the specific features from the DSWI representations. To estimate the performance of the proposed approach, it has been evaluated using the laboratory dataset collected from the bearing testbed. Finally, the results of the proposed method are compared with other methods presented in the

literature.

The remaining portions of this research are organized as follows: A description of the test rig, experiment setup, and data acquisition system is provided in Section 2. Section 3 describes the overall methodology of this study to construct the DSWI as the 2-D representation of the AE signal from the different types of bearing faults and the structure of the CNN for classification. Section 4 discusses and explains the resultant performance of the proposed methodology using the different evaluations from the dataset, and Section 5 gives the conclusions of the paper.

### 4.2 Seed to the Data Acquisition System and Experimental Process

The dataset used to evaluate this work is acquired from the self-defined bearing testbed of Ulsan Industrial Artificial Intelligent Laboratory (UIAI) at Ulsan University (Ulsan, South Korea). The overall data are collected from bearings which were classified into normal (healthy) condition and bearings with artificial damage. The damaged bearings consisted of those with outer damage, bearings with inner damage, and bearings with roller damage. The test rig setup is described in Figure 4.1 which illustrates the real testbed image, and the different cases of artificial cracks generated on the bearings. During the data collection, the testbed was driven under a constant speed of 1800 r/min by the three-phase motor. The belt

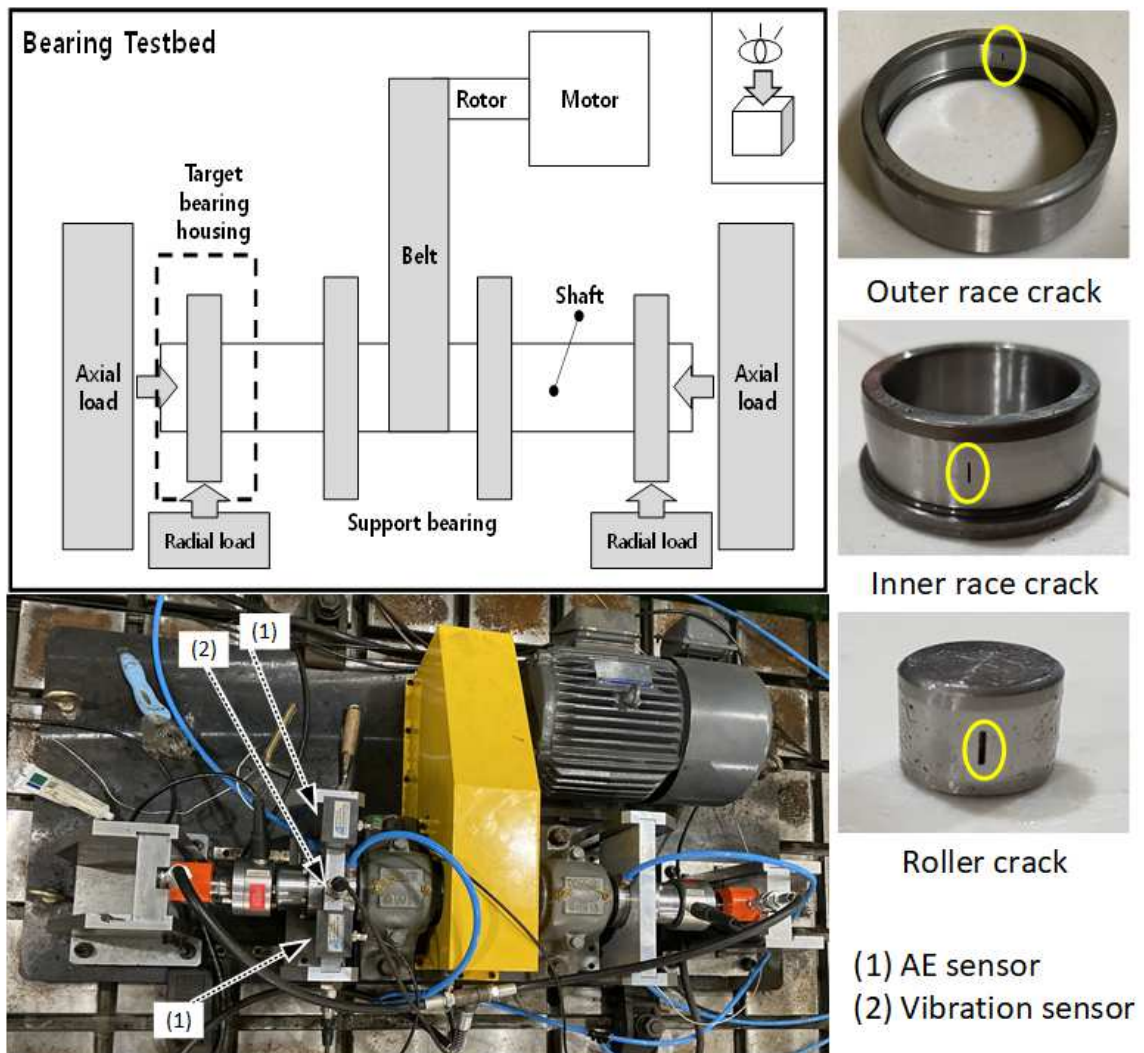


Figure 4.1 The self-defined testbed setup for measuring signals of bearing faults

helps to transmit the motion from the rotor shaft to the main shaft which is installed with two testing bearing housings on both sides. The cylindrical roller-element bearing in type FAG NJ206-3-TVP2 was used in this experiment. The AE signal and vibration accelerometer signal are acquired mostly from the target bearing on the left side. A constant load of 100 kgf was applied in both axial and radial directions to the main shaft and the bearing house.

The AE signal and vibration signal are recorded by the AE sensor of type R15I-AST [25] and accelerometer of type PCB-622B01 [26]. These sensors are both connected with the NI-9234 DAQ device which has four analog input channels and is designed to perform precise measurements from Integrated Electronics Piezo-Electric (IEPE) sensors. The NI-9234 is equipped with built-in anti-aliasing filters that have the ability to automatically regulate the sample rate the user specifies. The signals were collected with a sampling rate of 25 kHz. A detailed description of the dataset acquisition system is shown in Table 4.1. Each type of fault signal in the bearing is measured continuously for about 5 min, then segmented to 1-s signals for analysis. Therefore, each type of fault includes 309 data samples of 1-s signals. Then the testing bearing is replaced with another one and the test is repeated.

**Table 4.1** Specifications of measuring sensors and data acquisition card

Devices	Detailed Specification
AE sensor R15I-AST	<ul style="list-style-type: none"> <li>- Resonant frequency: 150 kHz (Ref in V/<math>\mu</math>bar)</li> <li>- Operating range: 50–400 kHz</li> <li>- Peak sensitivity: -22 dB (Ref in V/<math>\mu</math>bar)</li> </ul>
Vibration sensor PCB-622B01	<ul style="list-style-type: none"> <li>- Frequency range: from 0.2 to 15,000 Hz</li> <li>- Measurement range: <math>\pm 490</math> m/s<sup>2</sup></li> <li>- Sensor sensitivity: 100 mV/g</li> </ul>
DAQ type NI 9234	<ul style="list-style-type: none"> <li>- Operating condition: -40 °C to 70 °C operating</li> <li>- Dynamic range: 102 dB</li> <li>- Resolution: 24-bit</li> <li>- IEPE signal conditioning with AC coupling (2 mA)</li> </ul>

### 4.3 Fault Diagnosis Methodology Using the Defect Signature Wavelet Image

The main purpose of this research is to explore the appropriateness of characteristics of bearing fault signal to generate a 2-D representation which can help to separate different types of faults in bearings. To create a relevant 2-D representation to train the CNN classifiers, the

initial AE signals are fed across an envelope analysis to demodulate and are decomposed using the continuous wavelet transform with a specific frequency band acquired from the bearing characteristics and working conditions. Finally, the classifier model is built to validate the 2-D representation method. Several hyperparameters in the classifier structure are also characterized to ensure optimum performance. An overall workflow is presented below.

### 4.3.1 Bearing Fault Signature and Wavelet Analysis

Bearing faults can occur with many types of damage presenting such as spalling, pitting, misaligned races, waviness that happens due to improper installation, abrasive wearing, manufacturing error, material fatigue, and so on. In general, the fault in each bearing element has a specific representative frequency. When the fault appears on a bearing component, the interaction of defects with other surfaces generates pulses with small duration which lead to an increasing vibrational energy at that specific frequency. These frequencies depend on the geometry characteristics of the bearing such as the number of rolling elements (or balls)  $N_{roll}$ , the rolling element's diameter  $D_R$ , the cage diameter or pitch diameter  $D_p$ , the contact angle of the balls  $\alpha$ , and the rotational frequency  $Sp$ . This phenomenon will generate a high peak at a particular position in the spectrum from the FFT analysis. However, the damage frequency is amplitude-modulated to the high-frequency region that causes indiscriminate visualization when we observe the spectrum with the conventional FFT method. To overcome this drawback, the demodulation method is used with the Hilbert transform and envelope analysis. By these methods, a signal is filtered by the bandpass filter in a frequency band in which the fault impulse is amplified by structure resonances and is applied to remove the carrier signal. The envelope signals of bearing outer, inner, and roller faults are illustrated in Figures 4.2b, 4.3b, and 4.3f, respectively. The obtained envelope signal contains richer diagnostic information both in terms of the repetition frequency of ball-bass and ball-spin frequency about bearing fault. The envelope spectra, obtained by applying the FFT to the envelope signal with specific defect frequencies BPFO, BPFI, and BSF, for respective cases of outer, inner, and roller faults, are illustrated in Figures 4.2c, 4.3c, and 4.3g, respectively. Nevertheless, the envelope analysis still imparts some limitation. If only the FFT is used to calculate the envelope spectrum, that would lead to the loss of the time information of the signal envelope concerning the specified time when these impulses appear. To solve this issue, the authors

proposed another method using the continuous wavelet transform spectrogram with a specific frequency range that covers the three harmonics of the largest defect frequency, to represent the signal envelope in both time and frequency domain.

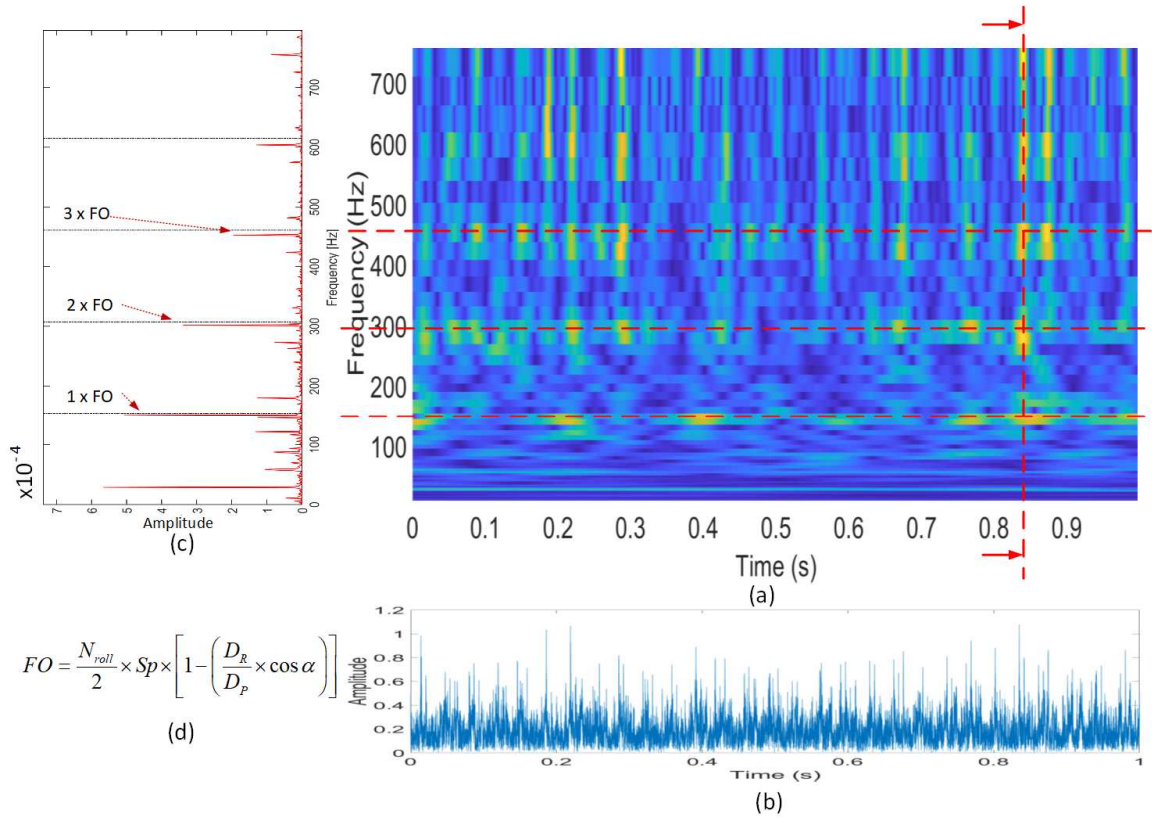


**Figure 4.2** 2-D representation of the signal corresponding to the outer fault: (a) DSWI, (b) envelope signal, (c) envelope spectrum with FO defect frequency, and (d) outer defect frequency FO, respectively

Among the time–frequency decomposition methods, the short-time Fourier transform is constrained by the time–frequency resolution. To obtain an exact time resolution requires an analysis window to be short, whereas a long analysis window involves an accurate frequency resolution. The wavelet analysis is a recommended methodology to process the nonstationary AE signals, and it is acceptable to detect the temporary changes in the signal. In wavelet methods, the AE signals are decomposed in terms of a zero-mean function of a family of wavelets that keep an invariable shape but are able to be dilated and shifted in time. CWT (or an admissible wavelet) projects an AE signal  $s(t)$  onto a family of zero-mean functions  $\psi_{\sigma,\nu}(t)$  (family of wavelets):

$$W_s(\sigma, \nu) = \int_{-\infty}^{+\infty} s(t)\psi_{\sigma,\nu}^*(t)dt, \quad (4.1)$$

where  $\psi_{\sigma,\nu}^*(t)$  represents the complex conjugate,  $\sigma$  stands for a dilation factor, and  $\nu$  is a translation factor. The wavelets remain normalized, such that  $\|\psi_{\sigma,\nu}\| = 1$ , as the mother wavelet is normalized. The factor  $\nu$  has the role of shifting in time such that if the  $\nu$  gets a positive value, the mother wavelet is shifted to the right, and if the  $\nu$  gets a negative value, the mother wavelet is shifted to the left. To comprehend the role of the dilation  $\sigma$  in wavelet analysis, let us use Parseval's theorem to transfer the Equation (4.1) to the frequency domain:

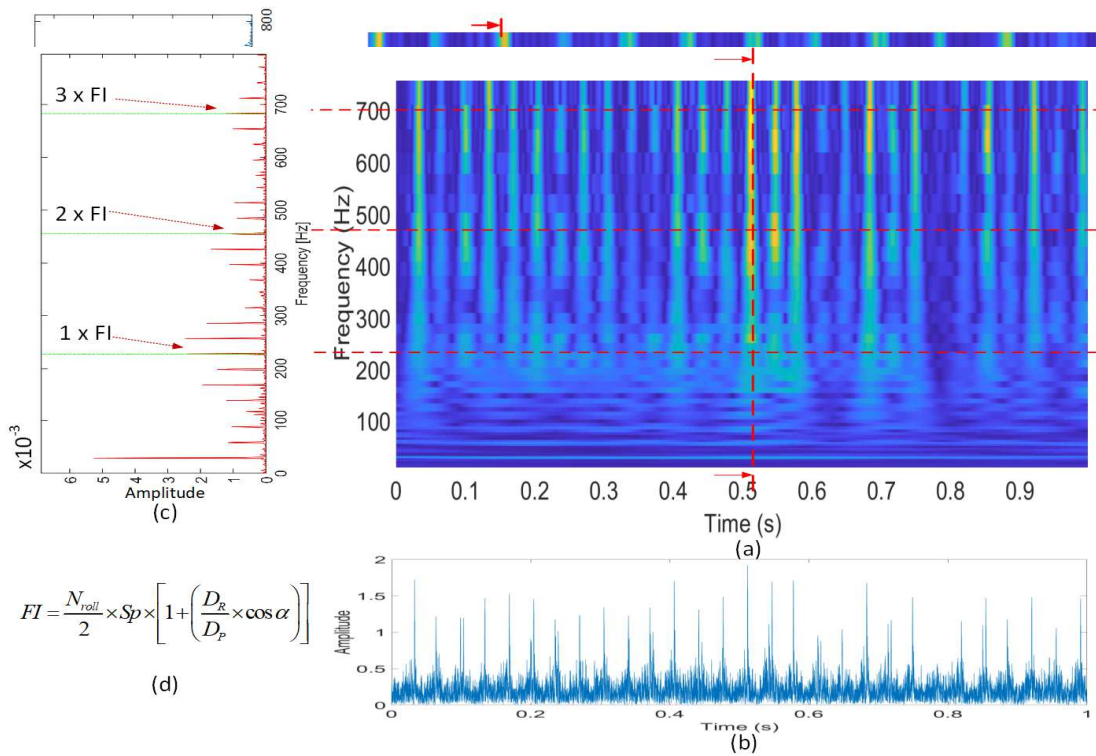
$$W_s(\sigma, \nu) = \frac{1}{2\pi} \int_{-\infty}^{+\infty} \hat{s}(w) \hat{\psi}_{\sigma,\nu}^*(w)dw, \quad (4.2)$$

where  $\hat{s}(w)$  represents the Fourier transforms of  $s(t)$  and  $\hat{\psi}_{\sigma,\nu}^*(w)$  are Fourier transforms of  $\psi_{\sigma,\nu}^*(t)$ . Since  $\hat{\psi}(0) = 0$ , the transfer function of a bandpass filter is represented by  $\hat{\psi}(w)$ , which means the function  $s(t)$  is particularized by the decomposition with wavelet family in the form of a series of different frequency bandwidths. Furthermore, the energy bandwidth can be expressed by:

$$\varepsilon_w^2 = \frac{1}{2\pi E} \int_0^{+\infty} (w - w_c)^2 |\hat{\psi}(w)|^2 dw, \quad (4.3)$$

where  $w_c$  corresponds to the center frequency of  $\hat{\psi}(w)$ , and  $E = (1/2\pi) \int_0^{+\infty} |\hat{\psi}(w)|^2 dw$ . Hence, the center frequency of the wavelet and the energy bandwidth of the wavelet are  $(w_c/\sigma)$  and  $(\varepsilon_w/\sigma)$ , respectively. Thus, since the scaling parameter  $\sigma$  changes, both the energy bandwidth and the center frequency of the wavelet vary. That means if the value of factor  $\sigma$  is large, the mother wavelet has the role of a zoom-in function and vice versa. Moreover, when the value of parameter  $\sigma$  is large, the bandpass width becomes diminutive, which yields an increase of resolution in frequency analysis. In this study, the 2-D representation DSWI with the CWT spectra from the envelope signal of AE signal for the outer, inner, and roller faults are shown in Figures 4.2a, 4.3a, and 4.3e, respectively. These figures depict the pattern considering both the frequency domain described by the defect envelope spectrum and the information from the time domain of the envelope signal which appears in the form of a periodic impulse. These figures also illustrate that depending on the

amplitude of impulse and the attenuation process, these impulses cannot always be seen in the frequency spectrum. At some point, these defect frequencies can be diminished and not be seen even if this is the 1X harmonic which usually has higher energy than the others. This characteristic represents the non-stationarity of the system. Moreover, if the segment signal has a length of less than 0.1 s, the information about the bearing defects is missed. Hence, setting up the sampling rate and segment length appropriately is important to not lose the information.



$$FI = \frac{N_{roll}}{2} \times Sp \times \left[ 1 + \left( \frac{D_R}{D_p} \times \cos \alpha \right) \right]$$

(d)

**Figure 4.3 Cont.**

frequency for inner fault, (a) inner defect frequency FI, (e) DSWI for roller fault, (f) envelope signal for roller fault, (g) envelope spectrum with SF defect frequency for roller fault, and (h) roller (ball spin) defect frequency SF, respectively.

### 4.3.2 2-D Data Representation with Defect Signature Wavelet Image Generation

The overall process of the proposed methodology to construct the DSWI and bearing fault diagnosis is presented in Figure 4.4. Fundamentally, by virtue of the Hilbert transform, the

signal envelope can be computed. The one-second AE signal  $s(t)$  in the time domain is converted to the Hilbert domain  $\tilde{s}(t)$  using the Hilbert transform [98], [99]. The Hilbert transform applies the convolution of  $s(t)$  with the signal of  $1/\pi t$  that produces  $\tilde{s}(t) = s(t) * (1/\pi t)$ . Then the method calculates the analytic signal in a complex number form with both in the real part and in the imaginary part as in quadrature, where  $j$  represents the imaginary unit. Immediately, an advantage is detailed in that the demodulating of the extraction of the spectrum section is effectively executed by an ideal filter, which helps to distinguish it from adjacent components which will be considerably stronger such as the gear mesh frequencies. Following that, the absolute value of  $env(t) = |s_a(t)| = |s(t) + j\tilde{s}(t)|$  is computed to yield the signal envelope. Then, the square root of FFT with signal  $env(t)$  performs the envelope spectrum. In fact, it is more desirable to analyze the square of the envelope signal instead of the envelope itself. A simple argument for that is by comparison of the spectra of a squared signal with that of a rectified signal. In mathematical terms, it should be considered that a rectified signal is the same as the square root of the squared signal. Likewise, the envelope of the signal is calculated as the square root of the squared envelope. When the square root operator is applied, it launches extraneous components which do not appear in the original squared signal, and this is the reason to create the masking of the desired information. Because the entire operation is calculated digitally, it is impossible to erase the high harmonics by using lowpass filtration, and they generate the alias to the measurement range, which causes masking. In addition, when applying the one-sided spectrum, by considering the analytic signals whose squared envelope is constructed by multiplication with its complex conjugate, the spectra of the squared envelope is the convolution of the respective spectra. When this convolution is carried out, the result only yields different frequencies, e.g., sideband spacings. These different frequencies will contain the desired modulation information. Then the

envelope signal is supplied to the continuous wavelet transform.

The continuous wavelet transform with damage frequency filter band is applied after obtaining the envelope signal to generate the DSWI representation. The use of wavelet transforms to detect local faults in bearings has been described by many authors. However, most of the literature on utilization of wavelet decomposition for fault diagnostics makes the error of considering the performance only in the time-domain (mostly for denoising) and on a short-recorded segment of signal, frequently shorter than the longest modulation period. Usually, the assertion is that the wavelet transform is more advanced than envelope analysis. Nevertheless, many authors fail to realize that the wavelet coefficients' squared modulus is helpful for a squared envelope signal, and much diagnostic information can be derived by analyzing the frequency domain of such squared envelope signals. As discussed, frequency-domain analysis of the envelope signal often makes evident fault repetition (in the form of transition peaks) and modulation patterns which are often difficult to recognize in time-domain signals, especially when the modulation phenomenon is so strong that the transient impulse is only stimulated when the fault point is inside the load-zone. These impulses are

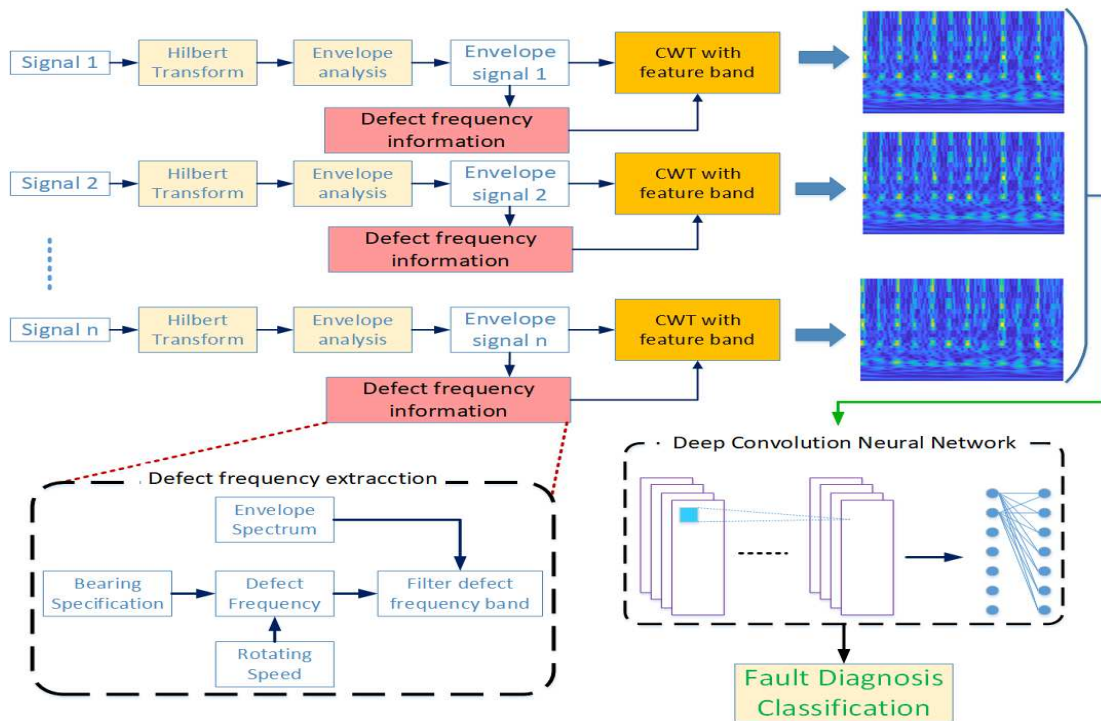


Figure 4.4 Generating the DSWI representation and process for fault diagnosis.

thus created with greatly varied amplitude. For instance, the continuous wavelet transform has a similar skeleton with the Fourier transform. While the Fourier transform yields correlation coefficients between the original signal and a sinusoidal signal, continuous wavelet transform obtains correlation coefficients resulting from an inner product of the mother wavelet and the signal. Unlike the Fourier transform though, where the signal is converted into the frequency-domain, continuous wavelet transform transfers the signal to the time-frequency-domain by managing the shape of the mother wavelet. Here, the research controls the shape of the mother wavelet by adjusting the scaling and shifting parameters. Continuous wavelet transform, using a smooth analytical mother wavelet, is able to identify the dynamic frequency characteristics of the signal at different scales. By employing various dilates and translations to the mother wavelet function, continuous wavelet transform coefficients reflect the resemblance of the signal to the wavelet at the current scale. The bump wavelet is a good choice for the continuous wavelet transform when signals are oscillatory, and when the researchers are more interested in time-frequency analysis than in the localization of transients. Moreover, bump wavelet has the best time resolution permitting separation of the start and the end times for each component of the signal with impressive precision for each of the performed tests. The bump is the symmetric wavelet in frequency and has an immediate relationship between the scale and the center frequency. The bump wavelet is defined by:

$$\hat{\psi}_{bump}(\zeta) = e^{1 - \frac{1}{1 - \sigma^2(\zeta - \nu)^2}} \chi_{(\nu - 1/\sigma, \nu + 1/\sigma)}(\zeta) \quad (4.4)$$

where  $\sigma > 0$ ,  $\nu > 0$  with  $\sigma\nu > 1$ , are the commonly used with continuous wavelets. The parameter  $\sigma$  controls the window widths of the time-frequency localization of the wavelets (plays a role in trans-shaping the mother wavelet  $\psi_{bump}$ ) and has effects on the representation of the transformed signal. In the literature, the wavelet parameter  $\sigma$  is usually treated as a fixed constant. The bump wavelet  $\psi_{bump}$  is bandlimited and hence it has better frequency localization than other wavelet families.  $\zeta_\psi = \nu$  admits the peak frequency which is defined by  $\zeta_\psi := \arg \max_{\zeta} |\psi_{bump}(\zeta)|$  and  $\chi$  denotes the indicator function. The translation parameter  $\nu$  is involved in the mother wavelet's location and specifies the properties of the resulting child wavelets. Therefore, this research also determines the characteristic signature

of faults at various locations of the mother wavelet by controlling the translation. The high-resolution in the frequency of large-scale wavelet permits us to capture the harmonic of the slow-variation elements whenever the fine-resolution of time in small-scale wavelet allows us to catch the fast-variation elements in the AE data. The wavelet decomposition enables detection of the hidden details of transient impulse waveforms, which is significant for inspecting a signal which contains both high frequency and low frequency components. In the case of the bump wavelet, the wavelet representation is almost symmetric with respect to the scale associated with the peak frequency. Since most defect characteristic harmonics stay in the low frequency range, fine-resolution frequency band analysis is essential to exactly interpret the properties of the abnormal indications in the bearing. As mentioned previously, the mother wavelet works in the role of a bandpass filter that permits a special frequency band to pass across a range existing between two limiting frequencies. This research scrutinized the multiple faults which occur in bearings by changing the cutoff frequencies of the bandpass filter with the frequency range which contains defect characteristics. The matrix of wavelet coefficients is established with the wavelet coefficients in a range which is defined as below:

$$P_{i,j} = f(\omega)$$

$$\text{with } \omega = 0 \dots f_{max} \text{ and } f_{max} = \max(FO, FI, SF) \times k + f_{side} \quad (4.5)$$

where  $k$  is the number of considered harmonics and  $f_{side}$  is the sideband of the highest defect frequency. Moreover, the initial low cutoff frequency is set to zero hertz for the fine resolution analyses in frequency. Because the frequency range is the function of rotation speed, it is robust when the rotating speed changes. Therefore, the DWSI always contains the damage frequency harmonics of bearing faults. Using these settings, the 2-D coordinate matrices are constructed, and then the values of coefficients in the matrix are employed to define the vertex colors by scaling the values in the matrix to the full range of the colormap to convert the representation of a 1-D vibration signal as a 2-D spectrogram image. Then, the 2-D which is similar to the spectrogram image is fed to a CNN model which is designed and trained for feature learning and classification.

### 4.3.3 Deep Convolution Neural Network Structure Specification

Convolution neural network has several benefits comparable to other feature-learning

methodologies. Previously, much as the stacked sparse auto-encoder did, the CNN automatically learns numerous levels of abstract representations from the data via their deep architecture layers. The learning process enables signals of high complexity to be learned to create a high-order representation feature. Secondly, the CNN applies an end-to-end structure for the learning model, hence, a single unique structure has to be optimized and the testing phase only needs a one-pass feed-forward process. Finally, the CNN model is utilized to exploit the spatial characteristic in the constructed DSWI from the sensor data. By using the sparse number of attributes, CNN reduces the number of training parameters when compared to the multi-layer perceptron network (a conventional artificial neural network). In the case of a DSWI from the AE signal, the CNN defines a spatial architecture as the set of three channels with respect to three channels of the DSWI. A typical case to note is that due to the rolling and sliding mode combination of the roller or ball in bearing, the expected energy which is contained in a fundamental frequency may not totally appear in the frequency range close to the fundamental frequency. Therefore, deploying this information can ameliorate the performance of the fault detection algorithm. Instead of feature extraction stage with the features being designed by experts, it should be considered that the difference of feature-learning method is in the researched work of this chapter as here, the feature extraction stage is not employed; thus, the CNN model is directly implemented on the DSWI of the AE data so that the CNN has the capacity to learn the features itself. Many optimization constraints, comprising batch normalization, dropout, initialization methods, and leaky rectified linear units, are also used for incorporating into the principal architecture of the CNN to create better classification performance. A CNN operates as follows: given an input image consisting of multiple channels, a convolutional layer computes a transformed output as the function of the input, weights, and bias parameters, with the difference from the normal artificial neural network being that the adjusted variables of the layer are organized as a sequence of filters and are applied to the convolving operator over the input to produce the output of the convolution layer. Each convolutional layer output is a 3D tensor, which includes a stack of 2-D matrices, the so-called feature maps, which will be utilized as input to feed to the next network layer of the CNN model. The weight parameters in the filter bank are distributed and shared over the local region of input, which efficaciously exploits the local spatial characteristics, and diminishes the quantity of optimized parameters. The convolutional

operation can be described as:

$$O_i^{(m)} = \varphi \left( \sum_{c=1}^c W_i^{(c,m)} \circ S_{i-1}^{(c)} + B_i^{(m)} \right) \quad (4.6)$$

In this formula,  $i$  stands for the order of the layer as before. The 2D convolution of the input  $S_{i-1}$  and the weight  $W_i^{(c,m)}$ , which is responsible for yielding  $m^{th}$  output of the map, is presented by the  $(\circ)$  operator in the formula. The term  $B_i^{(m)}$  represents the bias vector. After that, a nonlinear activation function  $\varphi$  on the sum of convolutions plus a bias vector is applied to obtain the final output. By utilizing a deep architecture, a network with several convolution layers, the model is more robust to complex variations in the data. Thus, if the data naturally describe many variations with high complexity, a deep architecture is necessary. In the case of bearing faults, due to the manifestation of the various faults which are considered here that illustrate a little variation, a reasonably designed deep model suffices. In addition, the initial layers of CNNs learn the fastest, so a short training period is adequate to achieve convergence. A lot of variations of the proposed CNN were examined by varying the number of convolutional blocks and fully connected layers, and the number of nodes in each layer. Applying to this particular case with the fault in bearing, an extremely deep version of the network model does not give better results but does increase the time for training. The structure which is applied in this study leverages the capacity of the CNN for exploiting the spatial structure in the DSWI data to sufficiently capture the properties of the AE signals. After the convolutional layer, batch normalization follows to improve the convergence process by regularizing the model to avoid overfitting. Then the output from the batch normalization is fed to the nonlinear activation function. The proposed CNN has a structure including several convolution blocks. Each block indicates one feature learning step with a specific level that includes convolution, batch-normalization, and activation function. Figure 4.5 depicts the designed architecture for each convolution block of the CNN model, which consists of six blocks of convolution with filters 3–8, 8–16, 16–16, 16–8, 8–8, and 8–1. The input image has a size of  $128 \times 128$  pixels with three channels. At the output after the six blocks, the feature maps are flattened and fed to the fully connected layers. There are two fully connected layers and a soft-max layer which has the role of the classifier. The most regularly

applied non-linear activation functions are the sigmoid, hyperbolic tangent, and rectified linear units (ReLU). Among them the ReLU function has been demonstrated to be more powerful than the others. However, during the training phase, ReLU units can die, and this problem can happen when great values of gradient flow across the ReLU function. This inspires the weights to be updated, and later the ReLU neuron fails to activate ever again on any data point. The leaky-ReLU function is an improved version that attempts to address this issue. The leaky-ReLU is used to introduce non-linearity into each stage, permitting the CNN to learn complex models. Normally, the pooling layer is employed to decrease the resolution of the feature maps via the subsampling step to reduce the number of parameters and quicken the computation. In this study, instead of using pooling to reduce the size of spatial representation, the authors proposed using the convolution layer with a large kernel size and stride. This approach shows better performance when extracting the features of the image in a deep network.

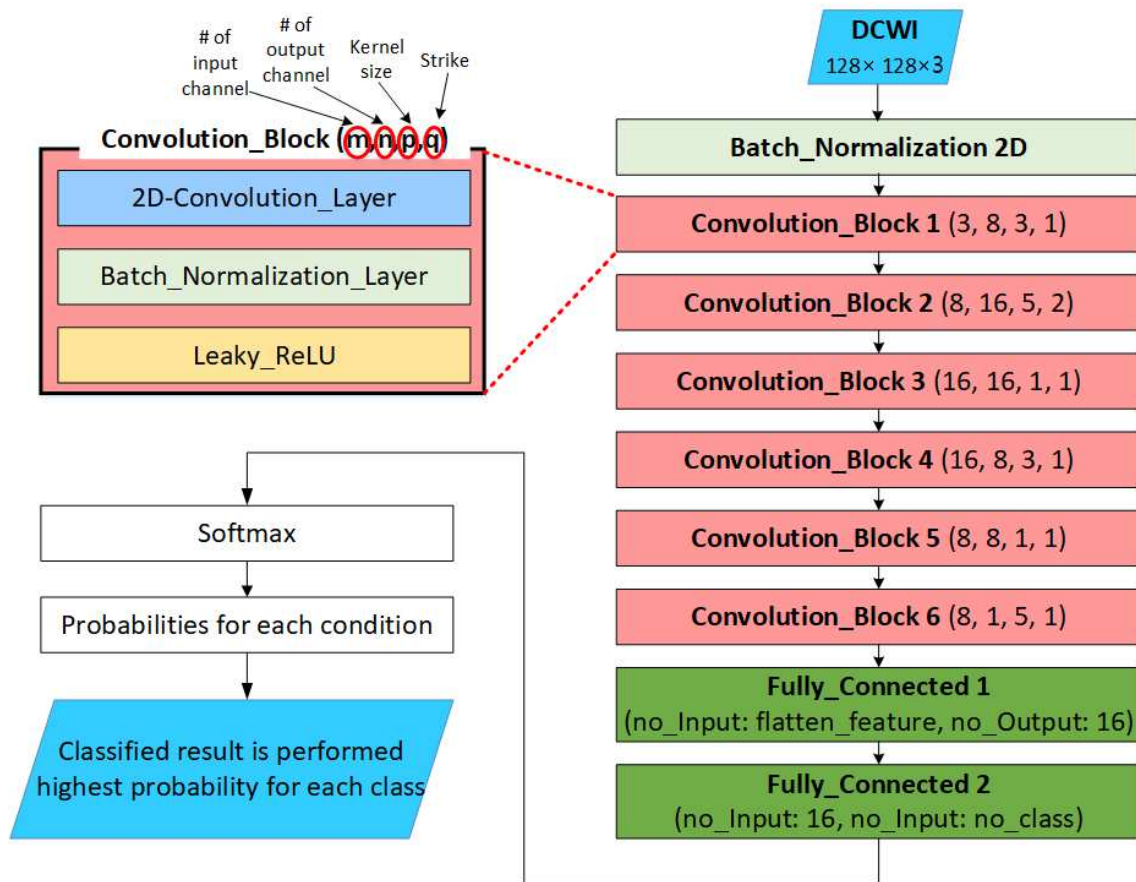


**Figure 4.5** The proposed deep convolution neural network architecture diagram for the  $128 \times 128$  size images

The training phase of the CNN model relates the learning of all the weights and biases, and it is essential to obtain the optimized parameters for a successful feature learning. During the training phase of the network's parameters, it is also necessary for the CNN to optimize the hyperparameters, which include the learning rate and dropout. The dropout holds an important characteristic of CNN, which considerably helps to prevent the overfitting phenomenon by generalizing the model. In the designed model, dropout with a proportion of 0.5 is employed for better regularization of the CNN. The adapted moment estimation, which is defined as a back-propagation strategy, is utilized to control the learning rate and other hyperparameters. The Adam optimization calculates the learning rate scale for different layers and avoids manual assignment to choose a suitable learning rate. Several configurations of the deep network, including LeNet-5 [29] and AlexNet [30], were tested to compare the results with

the proposed. The CNN model was trained with minibatch gradient descent and in each minibatch 100 training examples were used. The proposed CNN model training process is run over 100 epochs to learn the robust features for one normal operating condition and each type of faulty condition.

## **4.4 Methodology Evaluation Results**

In this section, the proposed bearing fault diagnostic method is evaluated using collected data from a real-bearing testbed which is described in Section 2. The AE signal has a duration of one second for each sample. It has been shown that a proper signal processing technique is required for converting the signal to meaningful information with the DWSI before feeding to the CNN. Each DWSI is constructed from a one-second sample signal using the method detailed in Section 3. This processing step is employed to retain the specific properties of different health states. Hence, the invariant signatures of different health conditions can use the full potential of the CNN. Then, the CNN model is trained to automatically extract and learn the features from 988 samples of the training dataset. The CNN is simultaneously validated with 248 samples of the validation dataset during each iteration epoch. The trained CNN model is validated by predicting the class for 248 samples from the test dataset. To evaluate the proposed method by comparing to other methods, two scenarios were employed using different types of 2-D representations as the input and with different CNN structures proposed in the literature.

### **4.4.1 Performance Evaluation of DWSI Compared to Vibration Image and Conventional Wavelet Spectrogram**

The same sample signals are used to create 2-D representations with the vibration image method and the conventional wavelet spectrogram. The vibration image is constructed by segmenting the raw signal in the time-domain into smaller samples and the segments are stacked one by one to generate the 2-D matrix. Then the values of the matrix are normalized in range [0,255] and converted to a grayscale image. This method is also used in [83], [84] to generate the 2-D image from the vibration signal. The second method to compare with the proposed method is the conventional wavelet spectrogram. The AE signal is directly analyzed with the continuous wavelet transform without envelope analysis and the information of the

damage frequency band is used to create the wavelet spectrogram. The detailed visualization of vibration image, wavelet spectrogram, and the DSWI for different types of faults in bearings and the normal case is shown in Figure 4.6. The proposed method with DSWI shows the pattern differences more distinctly between different types of signals compared to other 2-D representations. The other patterns do not show clearly separate visualizations from the different bearing status AE signals. Moreover, the pattern of DSWI illustrates a correlation to the damage frequencies as ascertained in Section 3. Since the AE-based method becomes more sensitive to low energy emissions from the bearing, gathering separate visual information associated with the energy distribution through low amplitudes can supply useful knowledge to further analyze. The DSWI with time-frequency-domain analysis can catch these small changes in signal form of the image by highlighting the powerful energy bands. Therefore, the DSWI includes low energy information in the field of time-frequency-domain. These kinds of images are provided as the input to the CNN to indirectly evaluate the performance of the proposed approach through the classification accuracy. The classification accuracy performance is detailed by the confusion matrices as illustrated in Figure 4.7. The confusion matrix indicates the class distinguishing performance by calculating the actual versus predicted deviation. For validating the diagnostic result, the metrics of sensitivity score (SS) and mean per class of sensitivity score are used. The sensitivity score formula is presented as follows:

$$SS = \frac{\#true\_pos}{\#true\_pos + \#false\_neg} \times 100\% \quad (4.7)$$

Here, the term  $\#true\_pos$  depicts the number of correctly predicted data samples from the provided test dataset which are used to validate the model at each iteration, and the term  $\#false\_neg$  refers to the number of data samples from a class that are wrongly classified. Hence, the average sensitivity can be obtained by  $avgSS = (\sum SS)/\#class$ , where  $\sum SS$  represents a summation of the class-wise sensitivity score for all the test dataset.

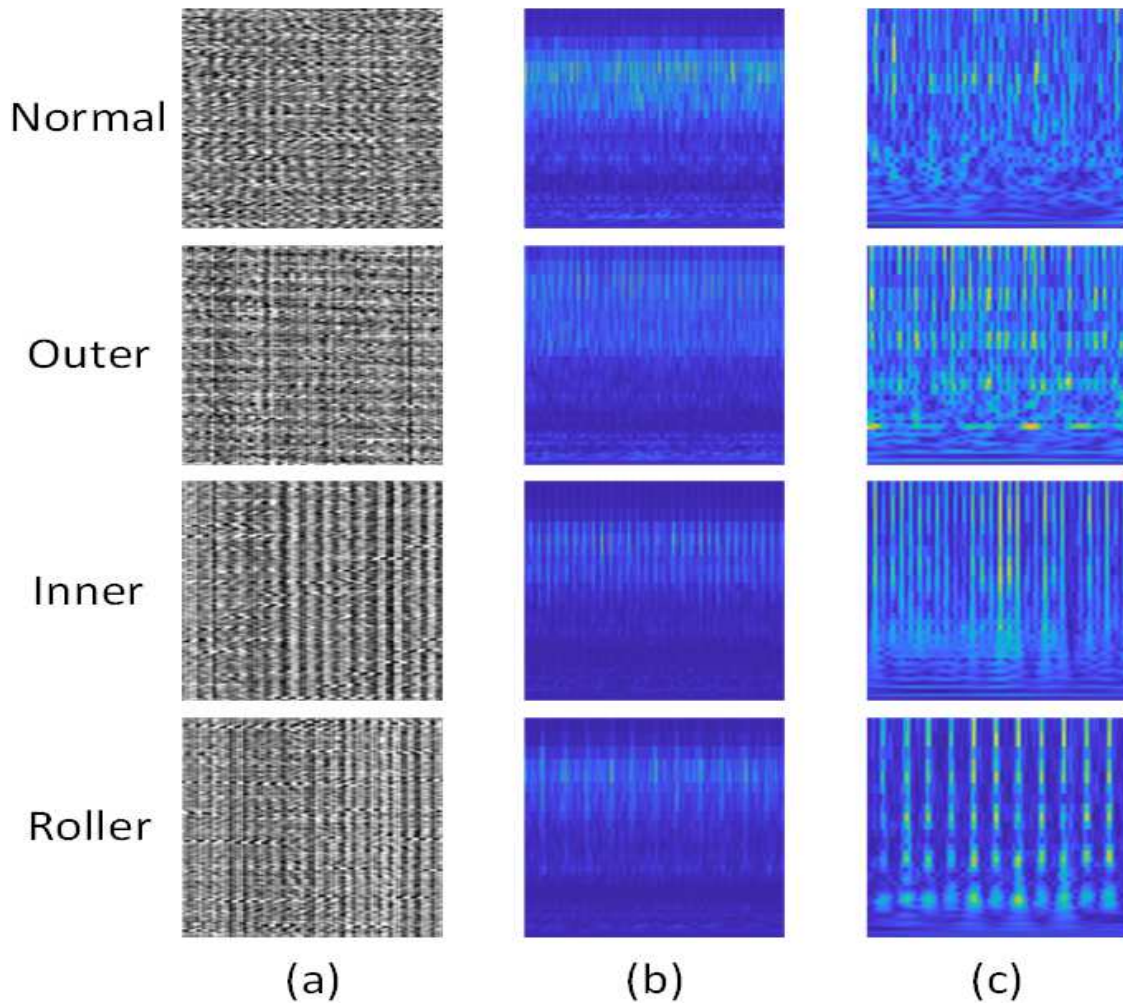


**Figure 4.6** The generated image of bearing fault signal from different methods: (a) Vibration image (b) Conventional Wavelet spectrogram image (c) DSWI

Then, the averages of all the accuracies and losses are collected to observe the accuracy values and loss values during the training stage. The CNN model hit an accuracy of 98.79% on average with the scenario of using the DSWI as the input, while the other scenarios of using the vibration image and conventional wavelet spectrogram had average accuracies of 83.06% and 93.15%, respectively, as described in Figure 4.7. Other devices such as motors and the noisy factory environment create impulses or random fluctuation peaks in the AE signal making the time-domain or frequency-domain analysis inefficient for this kind of AE signal. Processing the AE signal with DWSI can, however, partly alleviate the noisy random fluctuations and environmental stimulation in the AE signal. Apart from the comparison, vibration images obtained from the time-domain analysis are not sensitive enough to weak

incipient damage that may cause less discriminate information. Thus, the proper processing methods are preferred, which can result in discriminating information with conventional wavelet spectrogram and DSWI. From performances that are based on the other methods of the 2-D converted image of the AE signal, which taken together with results in discriminant patterns form for different types of faults in bearings, the conventional wavelet spectrogram can obtain a classification accuracy of more than 90%. However, the proportion of misclassification among different class types is not equal. Most of the misclassification happens in normal class because the pattern is not sufficiently discriminant. From the classification report, it is clearly observable that the proposed CNN model with the DSWI input is able to extract and learn the features from the training dataset and classify the features in the testing dataset for the appropriate faulty and healthy conditions.

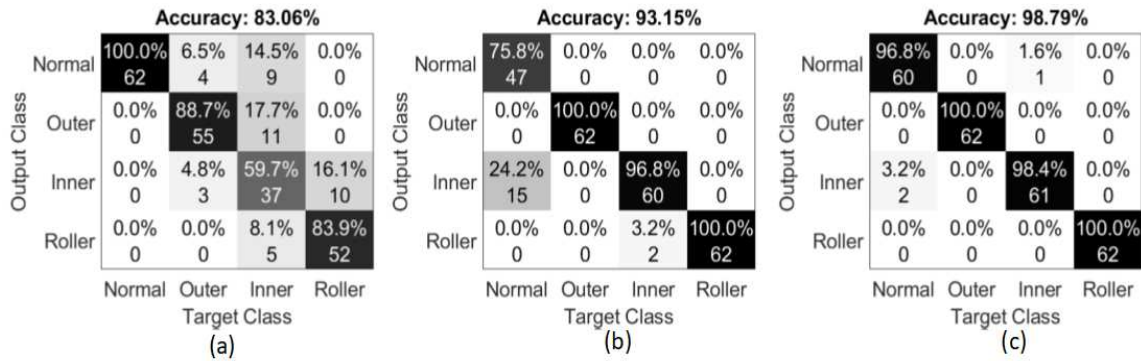


**Figure 4.7** The generated image of bearing fault signal from different methods: (a) Vibration image (b) Conventional Wavelet spectrogram image (c) DSWI.

#### 4.4.2 Performance Comparison with Difference Model for Classification

To further validate the performance of the diagnostic method, the proposed CNN model is compared against several state-of-the-art approaches: (1) K-nearest-neighbor + principal component analysis (KNN+PCA), (2) Multiclass Support Vector Machines + principal component analysis (MCSVM+PCA), (3) LeNet-5, and (4) AlexNet. The KNN and SVM methods using the feature extraction (FE)-based approach where the features are texture features extracted from the images of different types of 2-D representation include vibration image, conventional wavelet spectrogram and the proposed of DSWI. These features are extracted using the uniform local binary pattern method [100]. The method is employed based on the concept of the certain local binary patterns, termed uniform, that are fundamental

characteristics of local image texture. The image's occurrence histogram is indicated to be a very useful texture feature. Then, the KNN or Multi-class SVM (MCSVM) algorithm is utilized to carry out the fault classification after decreasing the feature space's dimensionality by principal component analysis. The LeNet-5 and AlexNet are two well-known CNN structures commonly used in the literature for image processing. The input of the LeNet-5 and AlexNet is the vibration image, the conventional wavelet spectrogram and the DSWI analogous to the input of the proposed CNN. The experiment comparing the CNN with the other approaches in literature is conducted with the same dataset that is used to evaluate the proposed model. The recorded dataset used to evaluate the proposed CNN and other machine learning models is detailed in Section 2. The prediction accuracy for the testing part of the dataset for each implemented method is gathered and presented in Table 4.2. As can be seen from Table 4.2, the other 2-D representation methods (i.e., vibration image and conventional wavelet spectrogram) showed inferior fault diagnostic performance when compared to the DSWI approach employed for the signal processing step. Thus, the comparison results show that the proposed DSWI clearly outperformed the other types of 2-D representations for all experimental scenarios with different classifier methods.

Table 4.2 also presents a collation of the other classifier models that are investigated with the proposed CNN. Therefore, by comparison with the recently researched deep learning architectures, our approach provides a better result. The results show that the proposed CNN approach attains a result superior to that of the other methods. The prediction accuracy is 98.79%, 97.98%, 95.97%, 87.76% and 61.63% for proposed CNN, AlexNet and LeNet-5, MCSVM+PCA, and KNN + PCA, respectively. This result also shows the superior performance of the proposed CNN approach. For the KNN + PCA and MCSVM + PCA which are based on the feature extraction method, the results illustrate lower accuracy because they depend on the characteristic of features, while the design of features needs the help of the experts for different types of application. The results from the LeNet-5 and AlexNet showed high accuracies proximate to the proposed CNN. However, the LeNet-5 is the simplest architecture and is not a strong enough structure for learning the information from the DSWI which is highly complex. AlexNet gives a better result but it is more complex and requires more time spent on training. According to the results reported in Table 4.2, the diagnostic performance of the CNN is best in all scenarios.

**Table 4.2** The classification report of the test dataset for different types of input and different classification methodology

Scenarios	Type	Vibration Image Method	Wavelet Spectrogram	DSWI
(1) KNN + PCA	Normal	35.50%	0%	93.50%
	Outer	41.90%	100%	88.70%
	Inner	30.60%	45.20%	61.30%
	Roller	98.40%	50.00%	0%
	<b>Average accuracy</b>	<b>51.42%</b>	<b>48.99%</b>	<b>61.13%</b>
(2) MCSVM + PCA	Normal	100%	75.20%	85.20%
	Outer	96.80%	84.23%	90.02%
	Inner	91.90%	86.80%	86.70%
	Roller	35.50%	81.40%	89.12%
	<b>Average accuracy</b>	<b>80.97%</b>	<b>81.91%</b>	<b>87.76%</b>
(3) LeNet-5	Normal	32.25%	96.77%	93.54%
	Outer	65.00%	100%	96.77%
	Inner	35.00%	59.67%	93.54%
	Roller	60.00%	100%	100%
	<b>Average accuracy</b>	<b>46.77%</b>	<b>89.11%</b>	<b>95.97%</b>
(4) AlexNet	Normal	64.52%	64.51%	98.38%
	Outer	100%	100%	100%
	Inner	13.33%	98.38%	93.54%
	Roller	96.77%	100%	100%
	<b>Average accuracy</b>	<b>68.54%</b>	<b>90.72%</b>	<b>97.98%</b>
Proposed CNN	Normal	100%	75.80%	96.80%
	Outer	88.70%	100%	100%
	Inner	59.70%	96.80%	98.40%
	Roller	83.90%	100%	100%
	<b>Average accuracy</b>	<b>83.06%</b>	<b>93.15%</b>	<b>98.79%</b>

## 4.5 Conclusions

In the modern era, the high complexity industrial system can ensure reliability and safety thanks to the sensor devices that have become necessary modules in comprehensive systems. Acoustic emission signals have emerged as an intelligent and optimized solution that simplifies the fault diagnostic procedure with a sequence of sensors. In this study, data-driven methodology using an acoustic emission signal analyzed by envelope analysis and an enhanced continuous wavelet transform with the damage frequency band information was used to generate the new 2-D representation image (so-called DSWI) from the 1-D signal. This DSWI shows the discriminate pattern and correlates with the defect frequencies for each type of fault in bearings helping to improve the performance of the machine learning methods for bearing fault diagnosis. The purpose of this study is also to propose a CNN architecture that is suitable for separating the DSWI from different types of faults in bearing. To validate

the diagnostic result of the proposed approach, the data collected from an elaborately self-designed testbed are deployed. Then, the experimental findings imply that the CNN classifiers achieved greater than 98% accuracy and other evaluation parameters also outperformed the current state-of-the-art. By incorporating the deep learning-based structure with the new time-frequency domain-based 2-D representation, the proposed method is efficacious, with great accuracy and no need for the feature selection stage. In addition, a collated comparison with some well-known methods in literature is executed and indicates that the DSWI with the CNN algorithm can become a promising method for bearing fault diagnosis.

## **Chapter 5**

### **Incipient Fault Diagnosis in Bearings under Variable Speed Conditions using Multiresolution Analysis and a Weighted Committee Machine**

#### **5.1 Introduction**

Bearings are the leading cause of failure in induction motors, and 51% of failures are attributed to a defective bearing [101]. These failures can cause unscheduled and costly shutdowns. The early detection of these defects is helpful in preventing such abrupt shutdowns. The initiation and propagation of cracks in the bearing material is associated with the sudden release of energy, which propagates as structure-borne waves or acoustic emissions (AEs). AE activity can be used to detect material defects in bearings; thus, acoustic emissions are commonly used to monitor the condition of bearings, especially for the diagnosis of incipient faults [102].

Localized defects in bearings, including cracks on the roller and inner/outer raceways, can be diagnosed via envelope analysis of the AE signals. This involves the detection of peaks in the power spectrum of the AE envelope signal at the characteristic frequencies associated with each defect type, such as  $2 \times \text{BSF}$ ,  $\text{BPFO}$ , and  $\text{BPFI}$  [103]. However, since these are kinematic quantities, these characteristic frequencies depend on the rotation speed and bearing geometry. Therefore, envelope analysis-based methods are of limited utility in the diagnosis of bearing faults under variable speed conditions. Khan et al. proposed a vibration signal imaging-based method for rotational speed-invariant fault diagnosis in bearings [104]. In their technique, they render the vibration acceleration signal as a grayscale image and use texture descriptors, which are based on the local binary operator, for the diagnosis of different faults. The high rotational speed of bearings and the lower sampling rate (12 kHz) resulted in clearly distinguishable textures and easy to handle image dimensions for the data [104]. However, acoustic emissions are sampled at very high sampling rates (such as 250 kHz for this study) because their frequency content lies within the range of 20 kHz to 1 MHz [102]. Imaging-based methods would result in very large images with sparsely distributed textures. Moreover, AE signals are usually used for incipient fault diagnosis at low rotational speeds [103], resulting in lower

impulses in the AE data; thus, AE signals would be rendered as barely visible textures by an imaging-based method.

Feature extraction based methods usually extract features from the raw condition monitoring signals, i.e., vibration acceleration or AE, and then use those features to develop discriminatory models of the data to classify different bearing defects [13]. However, under variable speed conditions, features extracted from the raw AE signal, result in overlapped feature spaces that result in poor discriminatory models. In this study, an improved feature extraction method is proposed to diagnose incipient bearing defects. The proposed method decomposes the raw AE signal into different sub-band signals using the discrete wavelet packet transform (DWPT), which is more effective for the multiresolution analysis of non-stationary signals [105]. A feature vector is extracted from each subband signal, resulting in multiple feature vectors from the raw AE signal. In contrast, traditional feature extraction methods extract a single feature vector from the raw AE signal. The feature vectors extracted from different sub-bands of the original AE signal result in models of the fault data that are discriminatory, even under variations in the rotational speed, as shown by the results in Section 4. The weighted committee machine (WCM), which is an ensemble of SVMs and ANNs, is employed to build discriminatory models of the feature vectors for different bearing defects.

## 5.2 The Acquisition of Acoustic Emission Data

For this study, acoustic emission data for both normal and defective bearings are captured using a wide-band AE sensor; these are recorded at a sampling rate of 250 kHz using a PCI-2 system. These signals are then divided into two datasets based upon the defect size, as shown in Table 5.1. Each dataset has signals for a BNC and bearings with seven types of localized defects, including ORCS; IRCS; RECS; cracks on the inner and outer raceways (BCIO); cracks on the outer raceway and roller (BCOR); cracks on the inner raceway and roller (BCIR); and cracks on the inner raceway, outer raceway, and roller (BCIOR). For each of these eight bearing conditions, 90 AE signals are recorded at five different rotational speeds each, as given in Table 5.1. The length of each AE signal is five seconds. Each of the two datasets contains a total of  $\sum_{Fault\_classes=1}^8 \sum_{RPM=1}^5 90(AESignals)$ , i.e., 3600 AE signals.

**Table 5.1** Classification result of the proposed method compare with vibration image method

Single and compound seeded bearing failures (90 AE signals for each bearing condition), $f_s=250\text{kHz}$	Rotating speed (RPM)	Crack size (mm)		
		Length	Width	Depth
Dataset 1	300, 350, 400, 450 500	3	0.35	0.3
Dataset 2	300, 350, 400, 450 500	6	0.49	0.5

### 5.3 The Proposed Methodology for Speed-Invariant Fault Diagnosis

Figure 5.1 presents the proposed methodology for incipient fault diagnosis in bearings under variable speed conditions. The proposed method employs DWPT for the effective multiresolution analysis (MRA) of a non-stationary AE signal [106].

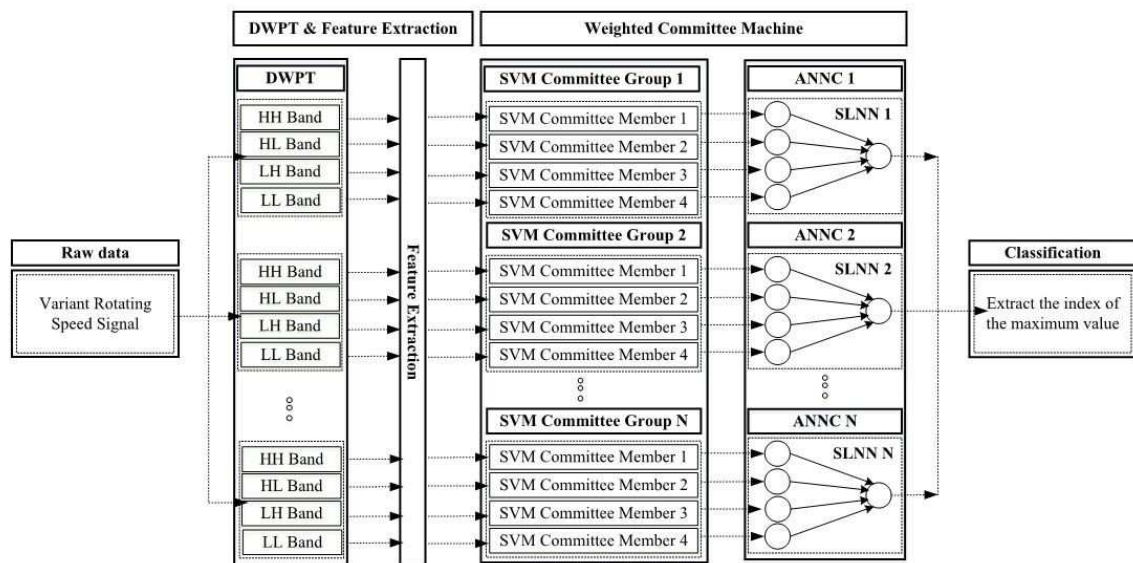


**Figure 5.1** The proposed method for incipient fault diagnosis under variable speed conditions using a WCM

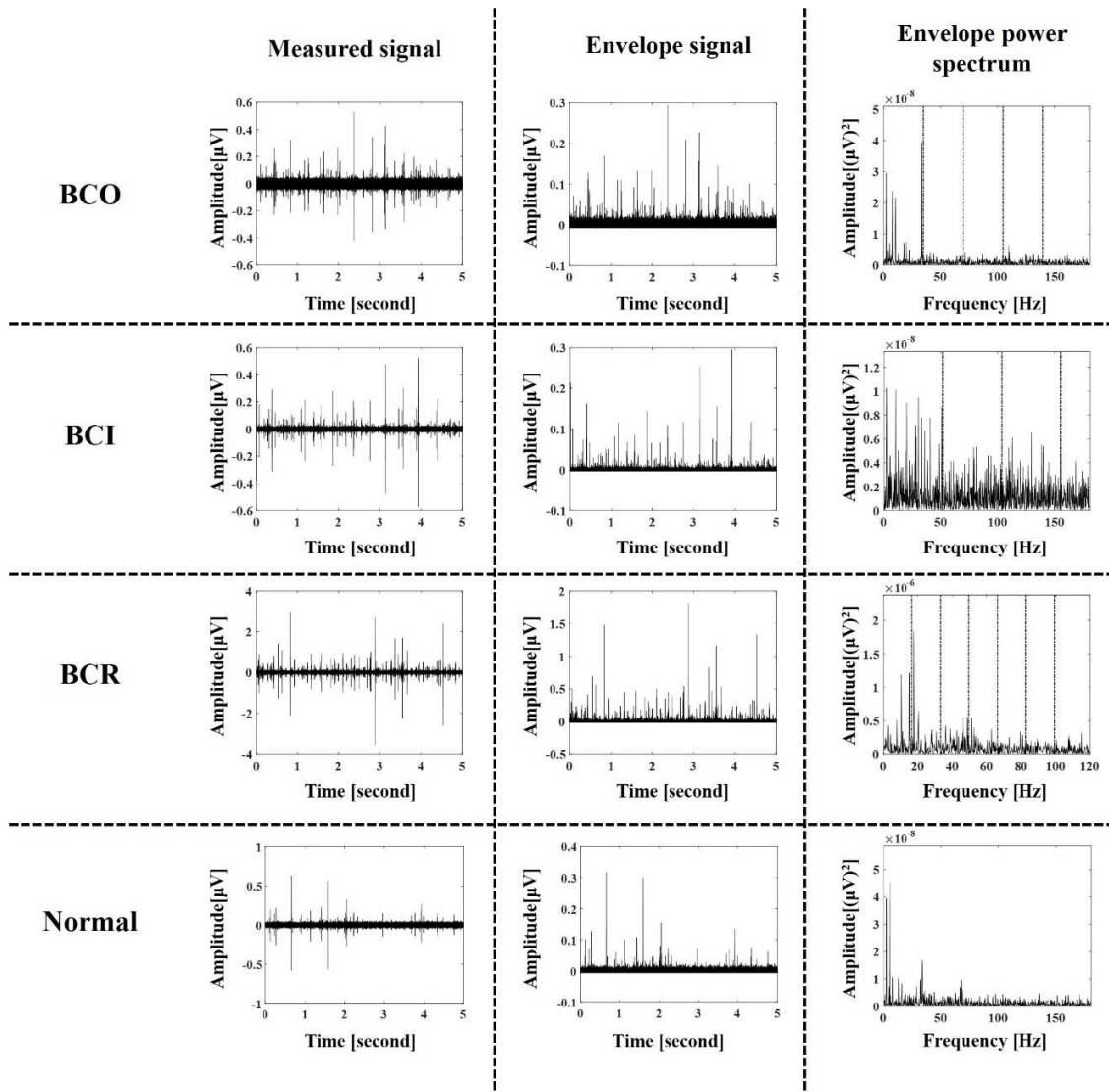


**Figure 5.2** The proposed method for incipient fault diagnosis under variable speed conditions using a WCM

Figure 5.2 shows measured AE signals, envelope signals via analytical analysis, envelope power spectra for a defect-free bearing (i.e., normal) and defective bearings (i.e., a bearing with a crack on its outer race (BCO), a bearing with a crack on its inner race (BCI), and a bearing with a crack on its roller (BCR)). Bearing characteristic frequencies (i.e., BPFO, BPFI, and BSF) can be computed as follows:

$$BPFO = \frac{n_{roller} \cdot f_r}{2} \left( 1 - \frac{B_d}{P_d} \cos \alpha \right), \quad (5.1)$$

$$BPFI = \frac{n_{roller} \cdot f_r}{2} \left( 1 + \frac{B_d}{P_d} \cos \alpha \right), \quad (5.2)$$

$$BSF = \frac{P_d \cdot f_r}{2 \cdot B_d} \left( 1 - \left( \frac{B_d}{P_d} \cos \alpha \right)^2 \right), \quad (5.3)$$

where BPFO is the ball pass frequency of the outer race, BPFI is the ball pass frequency of the inner race, and BSF is the ball spin frequency,  $n_{roller}$  is the number of rolling elements,  $B_d$  is the diameter of rolling elements,  $P_d$  is the diameter of a pitch,  $f_r$  is the rotating speed, and  $\alpha$  is the contact angle between the rolling element line and the inner raceway of the bearing [103].

The proposed method employs DWPT for the effective MRA of a non-stationary AE signal [106]. Using the Daubechies 15 mother wavelet, the AE signals are decomposed into two resolutions to generate four sub-band signals, where the frequency range of each sub-band according to the Nyquist theorem are 0 ~ 31.25 kHz, 31.25 ~ 62.5 kHz, 62.5 ~ 93.75 kHz, and 93.75 ~ 125 kHz in the sampling rate of 250 kHz. For each sub-band signal, 19 statistical quantities are calculated, as given in Tables 5.2 and 5.3. Thus, for each AE signal, a set of four feature vectors is extracted (i.e., one from each of its four sub-bands). The number of sub-bands is determined empirically to extract sufficient discriminatory fault information for rotational speed-invariant fault diagnosis. Traditional feature extraction methods for bearing fault diagnosis, extract features from the raw fault signal only, i.e., vibration acceleration or AE signal. However, as demonstrated by the results in Table 5.4, it results in poor discriminatory models for different fault types, under variable speed conditions. The discriminative performance of these models improves when the raw AE signal is decomposed into different sub-bands, and feature vectors extracted from those sub-bands are used to construct discriminatory models for different types of bearing faults or defects. The AE signals are decomposed into four sub-bands only, as further decomposition does not significantly improve the diagnostic performance of the proposed method and only adds to the complexity of the WCM.

**Table 5.2** The three statistical features of the frequency-domain AE sub-band signal. Here,  $S(f)$  is the magnitude response of the FFT of  $x(n)$  and  $N_{tfreqbin}$  is the total number of frequency bins.

Feature	Equation	Feature	Equation	Feature	Equation
Frequency center (FC)	$\frac{1}{N_{tfreqbin}} \sum_{n=1}^{N_{tfreqbin}} S(f)$	RMS frequency (RMSF)	$\sqrt{\frac{1}{N_{tfreqbin}} \sum_{n=1}^{N_{tfreqbin}} S(f)^2}$	Root variance frequency (RVF)	$\sqrt{\frac{1}{N_{tfreqbin}} \sum_{n=1}^{N_{tfreqbin}} S(f - FC)^2}$

**Table 5.3** The 16 statistical features of the time-domain AE sub-band signals. Here,  $x$  is an input signal,  $N$  is the total number of samples.

Feature	Equation	Feature	Equation	Feature	Equation
Peak ( $x_{peak}$ )	$\max( x(n) )$	RMS frequency (RMSF)	$\frac{x_{rms}}{\frac{1}{N} \sum_{n=1}^N  x(n) }$	Mean ( $\bar{x}$ )	$\frac{1}{N} \sum_{n=1}^N x(n)$
Root-mean-square ( $x_{rms}$ )	$\sqrt{\frac{1}{N} \sum_{n=1}^N x(n)^2}$	Entropy	$-\sum_{n=1}^N p(n) \cdot \log_2 p(n)$	Shape factor square-mean-root	$\frac{x_{smr}}{\frac{1}{N} \sum_{n=1}^N  x(n) }$
Kurtosis	$\frac{1}{N} \sum_{n=1}^N \left(\frac{x(n) - \bar{x}}{\sigma}\right)^4$	Skewness	$\frac{1}{N} \sum_{n=1}^N \left(\frac{x(n) - \bar{x}}{\sigma}\right)^3$	Peak-to-peak (PP)	$\max(x(n)) - \min(x(n))$
Crest factor	$\frac{\max( x(n) )}{x_{smr}}$	Square-mean-root ( $x_{smr}$ )	$\left(\frac{1}{N} \sum_{n=1}^N \sqrt{ x(n) }\right)^2$	Kurtosis factor	$\frac{Kurtosis}{\left(\frac{1}{N} \sum_{n=1}^N x(n)^2\right)^2}$
Clearance factor	$\frac{x_{peak}}{x_{smr}}$	Fifth normalized moment	$\frac{1}{N} \sum_{n=1}^N \left(\frac{x(n) - \bar{x}}{\sigma}\right)^5$		
Impulse factor	$\frac{\max( x(n) )}{\frac{1}{N} \sum_{n=1}^N  x(n) }$	Sixth normalized moment	$\frac{1}{N} \sum_{n=1}^N \left(\frac{x(n) - \bar{x}}{\sigma}\right)^6$		

**Table 5.4** Average classification accuracies and sensitivities for single and multiple combined bearing defects using different levels of decomposition of the original AE signal

Datasets	No of sub-bands	Average sensitivity for each fault type								ACA(%)
		BCI	BCO	BCR	BCIO	BCIR	BCOR	BCIOR	BNC	
Dataset 1	1	100	80	100	91.11	86.66	97.77	86.66	97.77	92.50
	2	95.55	100	97.77	88.88	91.11	91.11	91.11	100	94.44
	4	100	90	100	100	98.88	98.88	95.55	97.77	97.64
	8	96.66	100	100	97.77	98.89	98.88	93.33	96.66	97.77
Dataset 2	1	93.33	97.77	93.33	95.55	82.22	100	91.11	97.77	93.88
	2	97.77	97.77	95.55	100	95.55	97.77	93.33	100	97.22
	4	98.88	98.88	95.55	100	95.55	100	98.88	100	98.47
	8	100	100	100	97.77	95.55	97.77	100	100	98.89

These feature vectors are used to train the WCM and subsequently classify unknown AE signals. The WCM is an ensemble of two classifiers: support vector machine committee groups (SVMCGs) in the first stage and artificial neural networks as a combiner (ANNC) in the second stage. The SVMCGs in the first stage are used as a prior classifier, whereas the ANNC in the second stage combines the outputs of individual members of each SVMCG. In this study, the first stage of the WCM has eight SVMCGs (i.e., one for each fault class). There are four SVM committee members in each SVMCG, which are trained on the feature vectors from the corresponding sub-band signals. All the SVMs in an SVMCG are trained using the one-against-all (OAA) MCSVM framework. Thus, each SVMCG is used to create a discriminatory model that can identify a single fault type, independent of the rotational speed, using feature vectors extracted from the four sub-bands of the original AE signal. The outputs of each SVMCG (i.e., the four decision values of its member SVMs) are then used to train the artificial neural networks in the second stage, which act as a combiner for the first stage outputs. The WCM labels an unknown AE signal using the index of the maximum value in the ANNC outputs.

The SVM is a supervised binary classification algorithm that finds the largest margin hyperplane in the feature space of two classes. This hyperplane is then used to label test samples from both classes. It can solve nonlinear classification problems by mapping them to high-dimensional feature spaces using kernel functions [107]. This study uses the Gaussian

radial basis function (RBF) as a kernel function. Using Lagrange multipliers, the SVM algorithm can be reduced to solve the following optimization problem:

$$\begin{aligned} & \underset{\alpha_i}{\operatorname{argmax}} \left\{ \sum_{i=1}^n \alpha_i - \frac{1}{2} \sum_{i=1}^n \sum_{j=1}^n \alpha_i \alpha_j y_i y_j K(x_i, x_j) \right\}, \\ & \text{subject to } \sum_{i=1}^n \alpha_i y_i = 0, \quad 0 \leq \alpha_i \leq C, \quad \forall i = 1, 2, \dots, n \end{aligned} \quad (5.4)$$

Here,  $x_i$  and  $x_j$  represent samples from the training dataset,  $\alpha_i$  represents the Lagrange multiplier, and  $C$  is a penalty variable for tuning the generalization performance of the SVM. The corresponding classification function for the SVM is as follows:

$$\begin{aligned} & F(x) = \operatorname{sgn}\{f(x)\}, \\ & \text{where } f(x) = \sum_{i=1}^n \alpha_i^* y_i^* K(x_i^*, x) + b, \end{aligned} \quad (5.5)$$

Here,  $\alpha_i^*$  represents the Lagrange multiplier corresponding to the support vector  $x_i^*$ . The decision value  $f(x)$  ranges between  $-\infty$  to  $+\infty$  and represents the signed distance of an unknown observation  $x$  from the decision boundary. A positive decision value for a class indicates that  $x$  is predicted to be in that class, whereas a negative value indicates otherwise [108].

In the second stage of the WCM, single-layer ANNs with only one neuron in the output layer are trained independently as a binary classifier in the OAA strategy; this is done using the Levenberg-Marquardt (LM) backpropagation algorithm [109]. Single-layer ANNs are used due to their simplistic structure and their ability to classify linearly-separable patterns. The output neurons use the sigmoid activation function; thus, the output of each ANNC lies between 0 and +1. The class label for the unknown sample  $\bar{x}$  is determined using the decision function in (4), where  $y_i$  is the output of the  $i^{\text{th}}$  ANNC.

$$F(\bar{x}, y_1, y_2 \dots y_8) = \operatorname{argmax}(y_i) \quad (5.6)$$

Overfitting can reduce the generalization performance of an ANN, but this can be improved through a variety of techniques, including early stopping, regularization, and retraining [110]. This study utilizes these methods to improve the generalization of the ANNC, as illustrated in Figure 5.3. The ANNC is trained using the decision values from SVMCG, which are divided into training and validation subsets at ratios of 0.7 and 0.3, respectively.

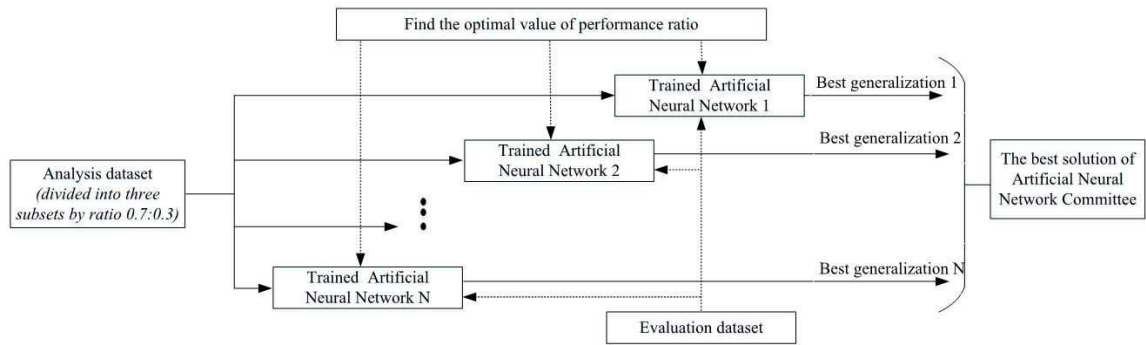


**Figure 5.3** The algorithm for optimizing the ANN committee

The performance function of the ANNC is modified by adding the mean of the sum of squares of the network weights and biases,  $msw$ , as given in Equation (5.7).

$$msereg = \gamma * msw + (1 - \gamma) * mse \quad (5.7)$$

Here,  $\gamma$  is the performance ratio and  $mse$  is the mean of the sum of squares for the network errors. This modified performance function smooths the network response, making it less likely to overfit; this is done by forcing it to have smaller weights and biases. The training and validation steps are repeated multiple times for different values of  $\gamma$  to find the optimal value in the interval [0 1]. The above process is repeated to train several ANNCs and find the one with the best generalization.

### 5.4 Experimental Results and Discussion

The proposed method for speed-invariant fault diagnosis in bearings is validated using the datasets presented in Table 5.1. Each dataset is divided into two subsets: one for analysis and the other for evaluation. For each bearing condition, 50% of the AE data signals are used to construct the analysis dataset, while the remaining 50% are used to set up the evaluation dataset. The AE signals in the analysis set are decomposed into two, four and eight sub-band signals each. For each level of decomposition, 19 features are extracted from each sub-band signal. These feature vectors are used to train the SVMCGs of the WCM using the OAA framework. The SVMCG reduces the 19 features into a single decision value that is more discriminative; this is then used to train the ANNC in the second stage, as discussed in Section 3. Figure 5.4 shows the four decision values from SVMCG 1 for the 240 AE signals in the analysis set, when each AE signal is decomposed into four sub-band signals.

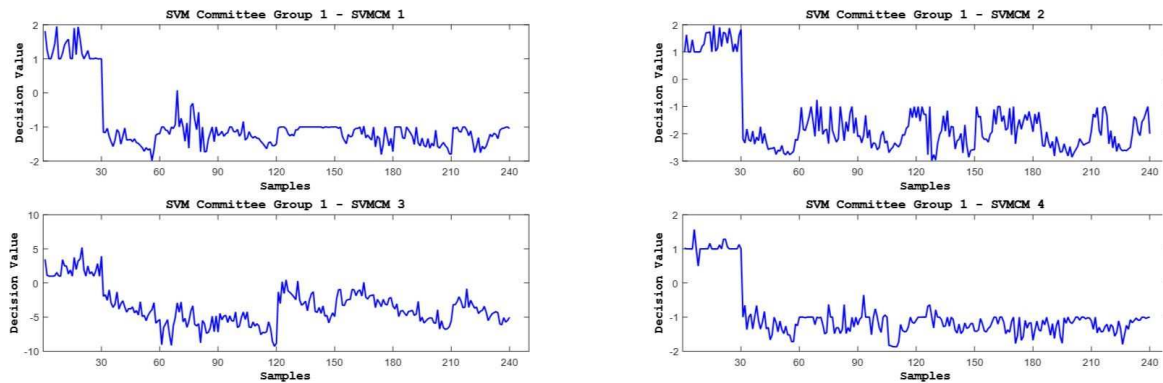


**Figure 5.4** The decision values of SVMCMs in SVMCG 1

The trained WCM is then used to classify the feature vectors extracted from different sub-bands of unknown AE signals in the evaluation dataset. The results in Table 5.4 indicate that the diagnostic performance of the proposed method, in terms of classification accuracy and sensitivity (i.e., the probability of correctly detecting a given fault), improves significantly when the WCM is trained using features vectors that are calculated for the original AE signal at multiple resolutions. The proposed method correctly detects incipient bearing faults of two different dimensions with average classification accuracies of 97.64% and 98.64%, respectively, when the original AE signal is decomposed into four sub-bands. However, further decomposition of the AE signal does not result in any significant improvement in

diagnostic performance, as shown in Figure 5.5.

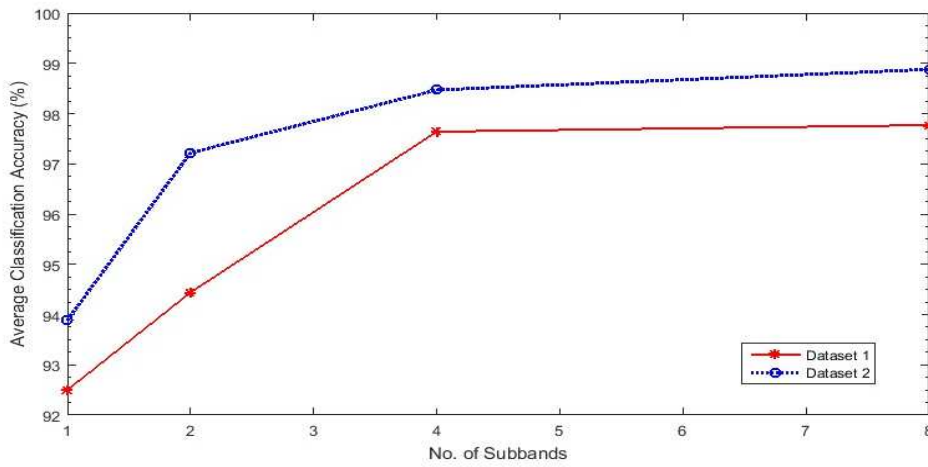


Figure 5.5 The performance of different number of sub-bands for datasets 1 and 2

## 5.5 Conclusions

Existing AE-based methods for the diagnosis of incipient defects in bearings, especially techniques that use envelope analysis, are not invariant to changes in a bearing’s rotational speed. This is the case because they rely on the detection of peaks at characteristic defect frequencies in the envelope power spectrum of the AE signals, and these defect frequencies vary with the bearing’s rotational speed. In this study, an improved feature extraction-based method is proposed for the diagnosis of incipient defects in bearings, under variable speed conditions. The proposed method decomposes the non-stationary AE signal into different sub-bands using DWPT. It extracts 19 statistical features from each sub-band signal to form feature vectors, which are then used to train the weighted committee machine. The WCM is an ensemble of support vector machines and artificial neural networks. Our experimental results show that the proposed method can effectively diagnose both single and combined bearing defects under variable speed conditions. Moreover, the advantages of decomposing the AE signal into different sub-bands are not unlimited, i.e., the improvement in diagnostic performance wanes when the AE signal is decomposed into more than four sub-bands for feature extraction.

## **Chapter 6**

### **A New Fault Classification Scheme Using Vibration Signal Signatures and the Mahalanobis Distance**

#### **6.1 Introduction**

Induction motors are complex electromechanical devices used in most industries in applications such as industrial fans, blowers and pumps, and conveyors and compressors. However, they are susceptible to many types of faults, and malfunctioning motors can cause large economic losses. Although the costs to repair or refurbish the motors themselves might not be substantial, the costs associated with downtime can be enormous [111]–[116]. Thus, condition monitoring systems for electrical machines play important roles in the safe operation of machinery and expand the motors' lifetimes by providing adequate warning of imminent failures, diagnosing present maintenance needs, and allowing workers to schedule future preventive maintenance and repair work, thereby avoiding heavy production losses, and maximizing uptime and optimum maintenance schedules. Early fault diagnosis techniques allow machine operators to have the necessary spare parts on hand before the machine is stripped down, thereby reducing outage times. Furthermore, fault prognosis systems can be integrated into maintenance policies, allowing usual maintenance at specific intervals to be replaced by condition-based maintenance [112], [115]–[117].

Many papers in the literature address the problem of identifying faults in induction motors by monitoring the motor status. Researchers have mainly used stator current, voltage, and vibration signals as the inputs for fault detection systems. Among them, vibration signals are preferable because they link directly to most machines' operational and maintenance stages. Vibrations are consequences of defects in a machine's structure; therefore, identifiable fault signatures can be found in vibration signals. Axial and radial acceleration sensors are used to detect mechanical problems, and tangential acceleration sensors are used to detect electrical problems. Thus, vibration monitoring is the most effective and reliable method for identifying faults in induction motors [118]–[120].

In general, condition-monitoring schemes have been widely used to identify specific failure

modes in one of the three main induction motor components: stator, rotor, and bearings. Several conventional vibration and current analysis techniques exist by which certain faults in rotating machinery can be identified for repair. Many researchers have applied advanced signal processing techniques over the measured physical magnitude to obtain good feature vectors for use as reliable fault indicators.

The existing techniques can be classified into three domains: time-domain analysis (mean, peak, peak-to-peak interval, standard deviation, crest factor, high-order statistics: root mean square (RMS), skewness, kurtosis, etc.) [120]–[124]; frequency-domain analysis (e.g., FFT, envelope analysis, spectral analysis) [118], [120]; and time-frequency domain analysis (e.g., wavelet transform) [119]. Based on the three domains, many features can be generated from vibration data. The original feature set from each of the three domains generally has high dimensionality, which under low variability from healthy and unhealthy states can complicate defect detection and degradation propagation prediction. Therefore, it is important to devise a systematic approach that can extract the most useful information about machine health states. Several methods have been introduced to reduce or select optimal features: linear and nonlinear principal component analysis [125], independent component analysis [120], and singular value decompositions [126], for example.

To the best of our knowledge, most methods follow the same rules. So-called “universal” feature generation and reduction methods are applied to all classes to derive distinctive condition signatures. That is a time consuming and difficult way to find a proper extraction method because the signature of a defective motor occurs within a wide frequency band and can be masked by noise. Instead of looking for highly significant features, this study aims to design and develop an effective method to generate different features to enhance the performance of a diagnosis system that will be able to learn new class signatures.

We select vibration signals, which are inexpensive and easy to measure, as the fault diagnosis system input for detection and classification. We then use spectral envelopes (spectral masks) and fast Fourier transforms to specify the harmonic components of a vibration signal. These signals model a particular motor failure signature such that the system can detect and classify comprehensive fault conditions in induction motors, as indicated in

[83]. With subsequent vibration readings taken under identical conditions, we can determine whether any deterioration that affects the vibration signatures has taken place in the machine's condition. In the classification task, we use the Mahalanobis distances between a test sample and known faulty signatures to measure the similarity between the sample and the signatures, so that the minimum distance indicates the name of the fault.

The remainder of the paper is organized as follows. Section 2 surveys the fault-related frequencies and harmonics of vibration signals from faulty induction motors. Section 3 presents the proposed vibration signature production method and diagnosis model. Section 4 presents a discussion of our experimental results, including comparison with several published algorithms. Section 5 concludes this chapter.

## **6.2 Fault-Related Harmonics in Vibration Signals**

We consider seven different motor conditions in this study, six mechanical faults: rotor unbalance (RU), broken rotor bar (BR), bowed rotor shaft (BS), faulty bearing (FB), angular misalignment (AM), and parallel misalignment (PM); and one healthy condition (NO).

### **6.2.1 Rotor unbalance (RU)**

The motor speed can be identified by a peak in the spectral range, which is determined by the number of poles in the rotor. If a motor is out of balance or misaligned, the fault signature normally takes the form of increased amplitude of the rotating frequency and its harmonics. Vibration analysis can provide a quick and relatively easy way to extract information about a rotor unbalance fault in an induction motor.

### **6.2.2 Faulty bearings (FB)**

The characteristic fault frequencies for FB depend on which bearing surface contains the fault, and they are predictable. In addition, bearing vibrations often occur at very high frequencies. From the geometry of the bearing, various theoretical frequencies can be calculated, such as the inner and outer race element pass frequencies, cage rotational frequency, and rolling-element spin frequency. A defect on the outer race will cause an impulse each time the rolling elements contact the defect. The theoretical ball pass outer

raceway frequency ( $f_{BPOF}$ ) is easily determined as

$$f_{BPOF} = \frac{n \omega_r}{2 \cdot 60} \left[ 1 - \frac{d}{D} \cos \phi \right], \quad (6.1)$$

where  $\phi$  is the ball contact angle with the races;  $D$  is the ball pitch diameter, measured from one ball center to the opposite ball center;  $d$  is the ball diameter;  $n$  is the number of balls in the bearing; and  $\omega_r$  is rotational speed in revolutions per minute (*rpm*). This vibration frequency ( $f_{BPOF}$ ) reflects itself in the current spectrum as follows:

$$f_{BRN} = (f_s \pm m f_{BPOF}), \quad (6.2)$$

where  $m = 1, 2, 3, \dots$ , and  $f_s$  is the electrical supply frequency.

### 6.2.3 Broken rotor bar (BR)

The space harmonics ( $f_{BB}$ ) components indicate a BR defect in an induction motor:

$$f_{BB} = \left[ k \left( \frac{1-s}{p} \right) \pm s \right] f_s, \quad (6.3)$$

where  $s$  is the per-unit motor slip,  $p$  is the number of poles in the motor, and  $k/p = 1, 3, 5, \dots$  denotes the characteristic values of the motor. The sideband components around the supply current frequency  $f_s$  are as follows:

$$f_{BRB} = (1 \pm 2ks) f_s, \quad (6.4)$$

where  $f_{BRB}$  denotes the sideband frequencies associated with the BR. The slip  $s$  is defined as the relative mechanical speed of the motor  $n_m$  with respect to the motor synchronous speed  $n_s$  as follows:

$$s = \frac{n_s - n_m}{n_s}, \quad (6.5)$$

The motor synchronous speed  $n_s$  is related to the electrical supply frequency  $f_s$  as follows:

$$n_s = \frac{120f_s}{P}, \quad (6.6)$$

where  $P$  is the number of poles in the motor, and the constant 120 expresses the motor's synchronous speed  $n_s$  in *rpm* units.

#### 6.2.4 Bowed rotor shaft (BS)

When a motor runs with a bowed shaft, the vibration spectrum appears quite similar to that in an imbalance condition. A bowed shaft can be detected by measuring the separated shaft with a dial indicator. A bowed rotor shaft is an out-of-balance condition and shows up as a 1X-*rpm* and 2X-*rpm* vibration.

#### 6.2.5 Rotor misalignment (parallel (PM) and angular (AM))

Rotor misalignment results in a non-uniform air gap. Misalignment-related faults commonly occur as a result of FB. Higher orders of misalignment can cause rotor-to-stator rub, resulting in damage to the rotor or stator windings or cores.

### 6.3 Proposed Method

Our proposed fault classification system generates different fault-related features to enhance the accuracy of its classification decisions. The system is depicted in Figure 6.1. In Section 2, we discussed the fault-related theoretical harmonics. The proposed approach exploits those different harmonics for online identification of induction motor states. First, we generate the signatures of the condition vibration signals in a training stage, and then we use those signatures as motor condition indicators in online detection and classification of induction

motor defects.

### 6.3.1 Production of fault signatures in vibration signals

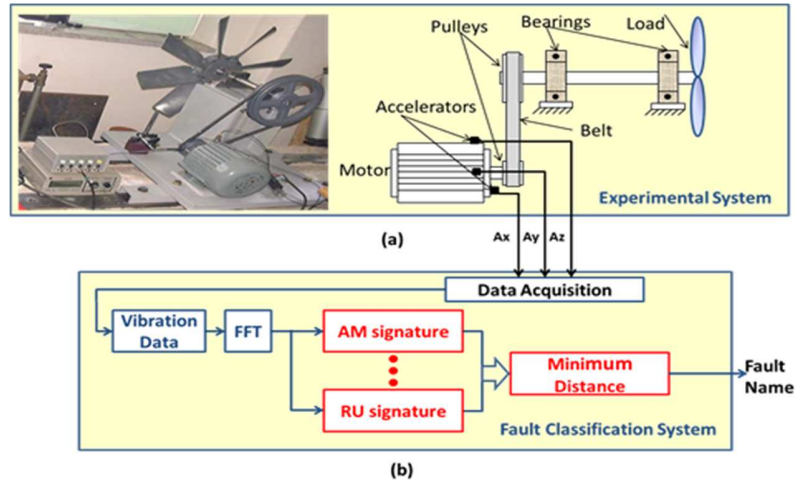


**Figure 6.1** Proposed online fault classification system

Signature production contains two phases, as depicted in Figure 6.2. The first phase specifies the set of relevant frequency bands and weights, where the frequency bands are the harmonic-related frequencies in each kind of vibration signal, and the weights are the values of the spectral envelope at each frequency band. In this study, we use the all-pole model to define the spectral envelope because it directly describes a power spectrum and hence can be easily combined with our harmonics structure model, which is defined on a linear frequency axis.

Figure 6.2 (a) shows the three concise steps we use to generate the frequency bands and weights phase.

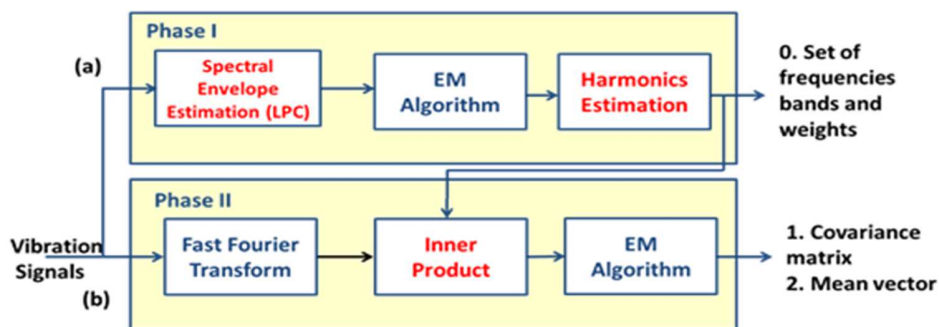


**Figure 6.2** Fault signatures in the vibration signal generation process

◆ Phase I:

- Step 1: Use one-second faulty vibration signals to calculate linear predictive coding (LPC) coefficients  $\{a_k\}$ , where  $k=1,2,\dots$ , and  $P$  is the LPC order. The spectral envelope of the vibration signal is then defined by the frequency response of the all-pole filter,  $H(z)$ :

$$\hat{x}[n] = \sum_{k=1}^P a_k x[n-k], \quad (6.7)$$

$$H(z) = \frac{1}{A(z)} = \frac{1}{1 - \sum_{k=1}^P a_k z^{-k}}, \quad (6.8)$$

- Step 2: Apply the expectation and maximization algorithm to estimate the mean spectral envelope from all the training samples for a specific motor condition.
  - Expectation step: Calculate the expected value of the log likelihood function with respect to the conditional distribution of  $Z$  given  $X$  under the current estimate of parameter  $\theta(t)$

$$Q(\theta|\theta(t)) = E_{Z|X,\theta(t)}[\log L(\theta; X, Z)], \quad (6.9)$$

where  $\theta(t)$  is the current parameter estimation, and  $\theta$  is the unknown actual parameter  $X$ .

- Maximization step: Find the parameters that maximize this quantity

$$\theta(t+1) = \underset{\theta}{\operatorname{argmax}} Q(\theta|\theta(t)). \quad (6.10)$$

- Step 3: Determine the frequency bands and weights. The peaks, or local maxima of the mean envelope of a specific motor condition, first defined in step 2 are found by first-order optimization techniques (gradient ascent method) on the frequency axis in

steps proportional to the positive of the envelope gradient at the current point.

$$f_{n+1} = f_n + \gamma_n \frac{\partial F(f)}{\partial f}, \quad n \geq 0, \quad (6.11)$$

Therefore:

$$F(f_0) \leq F(f_1) \leq F(f_2) \leq \dots \quad (6.12)$$

The sequence  $\{f_n\}$  converges to the desired local maxima. The interested frequency bands contain the harmonics and neighborhood frequencies of the vibration signals of the specific induction motor faults, defined by the valley frequencies adjacent to the peak frequencies. Weights at the frequencies are values of the spectral envelope if the frequencies are in the band and are zeros if the frequencies are outside the band.

◆ Phase II:

The second phase, shown in Figure 6.2 (b), uses the set of frequency bands and weights calculated in phase I to calculate the covariance matrix and mean vector of the fault signature. This phase contains three steps.

- Step 1: Determine FFT of the vibration signal to obtain the power spectrum

$$Y(m) = \frac{1}{N} \sum_{n=0}^{N-1} x(n) \omega(n) e^{-j \frac{2m\pi}{F} n}, \quad (6.13)$$

where  $N$  is the number of points used to calculate the discrete Fourier transform (DFT),  $0 \leq n \leq N-1$ , and  $\omega(n)$  is the Hamming window function given by:

$$\omega(n) = \beta \left( 0.5 - 0.5 \cos \frac{2\pi n}{N-1} \right). \quad (6.14)$$

- Step 2: Find the inner product of the power spectrum for each frequency band and weight determined in phase I.
- Step 3: Apply the expectation and maximization algorithm to find the covariance

matrix and mean vector of all training samples.

This procedure applies to each fault to generate its own signature. Thus, for our seven motor conditions, we need to run the process seven times to create seven signatures. The vector dimensions are unequal because the number of harmonics in the vibration signals varies from fault to fault, as explained in Section 2.

### 6.3.2 Online detection and classification system

Figure 6.1 (b) shows the schema of our online classification system based on the fault signatures in the vibration signal. The acquisition system receives the vibration signals from sensors attached to the induction motor. The vibration signal in the time domain is transformed to the frequency domain by fast Fourier transform. The power spectrum of the vibration signal then simultaneously feeds to the 7 fault models, which each have 3 components: set of frequency bands and weights, covariance matrix, and mean vector. The set of harmonics and its neighbor frequencies vary from signature to signature in number of bands and weight values within each band. For each model, the power spectrum is divided into a vector by an inner product operation between the spectrum and weight values in each band. The dimension of the output vector is the number of bands, which are defined in the signature production progress. We use the Mahalanobis distance to measure the similarity between the generated vector, represented by its mean value with the covariance matrix, and the fault signatures. In total, we calculate 7 Mahalanobis distances to classify the vibration signal to the corresponding fault category using the reference signature that gives the minimum distance to the vibration signal. Each signature model works as a binary classifier that can detect its own conditions against other motor conditions.

Mahalanobis distance: Given unknown  $x$ , it is assigned to class  $\omega_i$  if

$$d_i = \sqrt{(x - m_i)^T S_i^{-1} (x - m_i)}, \quad (6.15)$$

where  $S_i$  is the covariance matrix, and  $m_i$  is mean point of the  $i^{\text{th}}$  group.

## 6.4 Experimental Results

### 6.4.1 Experiment and simulation setup

To evaluate the performance of our proposed method, we set up an experimental testbed to acquire several different faulty vibration signals, as shown in Figure 6.1 (a). This setup consists of motors, pulleys, a belt, a shaft, and a fan with changeable blade pitch angle. We use 6 0.5kW, 60Hz, 4-pole induction motors to generate data under full load conditions. We collect NO and 6 fault signals: AM, PM, BR, BS, FB, and RU. Table 6.1 describes the different faulty conditions when the acquired vibration signals are sampled at 8 kHz. We use 105 one-second-long vibration signals for each faulty condition. More detailed information about this experiment is available in [120].

**Table 6.1** Details of fault conditions

Fault condition	Fault description
Angular and parallel misalignment	Rearing diameter: 40mm Housing maximum diameter: 40.7mm
Broken rotor bar	12 of 34 rotor bars were broken by holes; depth: 15mm, diameter: 5mm
Bowed rotor shaft	Shaft deflection in Mid-span: 0.075 mm, air gap: 0.025mm
Faulty bearing	Spalling on the outer race: #6203
Rotor imbalance	Unbalanced mass on the rotor: 8.4 g, Distance 40.2mm, position: 0°, 36°, 72°
Phase imbalance	Adding resistance to one phase

In our experiment, we implement a minimum distance classifier for faulty vibration signals from induction machines. We carry out 10 trials to obtain the average result. For each trial, we use 34 randomly selected signals for each fault to generate the vibration signatures and total data for validation. Therefore, the test data contain 735 vibration signals for seven motor condition signal categories (AM, BR, BS, FB, NO, PM, and RU), 105 samples per fault, to validate the approach. A vibration signal in the test data is used to simultaneously generate 7 vectors following steps 1 and 2 from phase II of signature production. Then we calculate 7 Mahalanobis distances to measure the similarity of the vibration signal to all fault categories.

The fault is classified into the category with the minimum Mahalanobis distance.

We consider the acquired vibration signals to be noiseless. To evaluate the efficiency and robustness of our work, we use simulated data with additive white Gaussian noise at Signal-to-Noise Ratio (SNR) = 15 or 20 dB to the vibration signals.

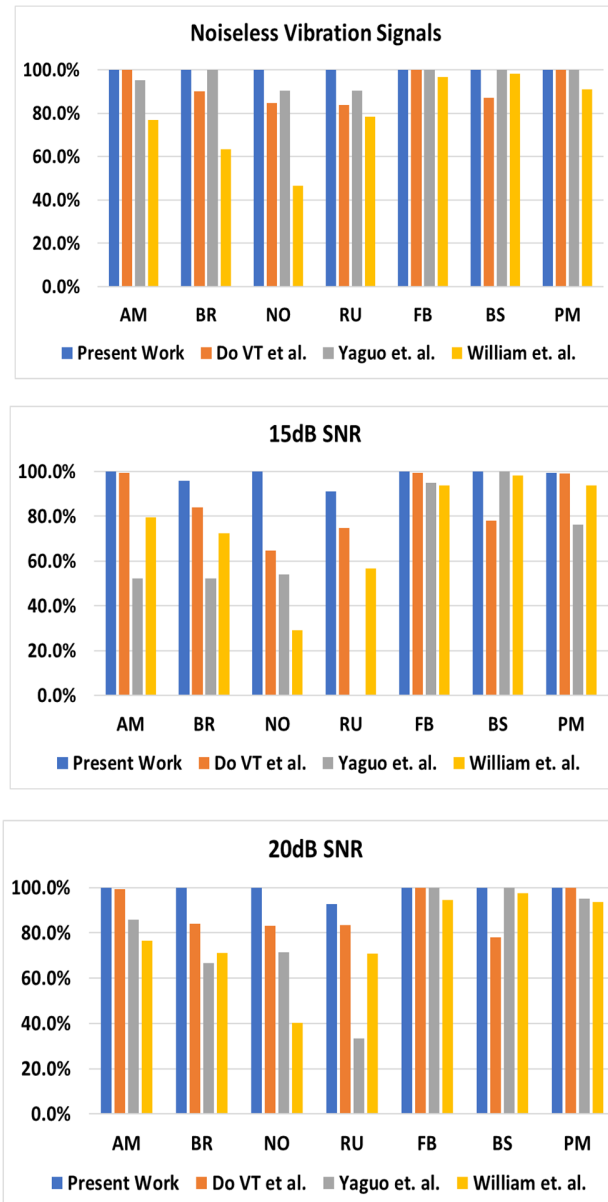


**Figure 6.3** Performance under different conditions

The accuracy values from our proposed approach are the highest for all kinds of conditions

at 100%, compared with the other 3 algorithms, which achieves 100% correct classification only for certain faults: AM, FB, PM, BR, FB, BS, and PM in [83](Figure 6.3). The general classification accuracy of our algorithm and the approaches in [121], [124] are 100%, 92%, 97%, and 79%, respectively. Our approach outperforms the algorithms in [121], [124] in detecting NO and RU conditions with 100% and 91% precise condition indications, whereas the published algorithms have less than 60% and 75% accuracy.

When we test the systems with noisy vibration signals, the accuracy of our approach decreases slightly to 98.18%, whereas the algorithms in [121], [124] show dramatic declines to 85.87%, 61.45%, and 74.78%, respectively.

The strength of our algorithm over the others can be explained by two main reasons. First, our approach can precisely detect the characteristic harmonics of a vibration signal, which helps us detect the motor condition. Second, we extract different features for each condition, represented by the frequency bands and weights, which is far better than the existing extraction methods that apply to all kinds of motor fault categories.

In addition to classification accuracy, the ability to detect an unknown state is an important requirement in an induction motor state monitoring system. The algorithm in [121] is originally designed to detect only bearing faults. With our dataset, we introduce other mechanical faults, such as rotor unbalance and angular misalignment. The approach in [121] seems unable to recognize the RU fault, having the very low accuracy value of 33.33% and 0% when the SNR is 20 and 15 dB, respectively, even though this kind of fault is used to train the diagnosis system. Our approach automatically detects the distinctive fault-related frequencies and then focuses on those frequency bands to generate more discriminant vectors for the introduced classes.

## **6.5 Conclusion**

Fault detection and classification are essential processes for manufactory automation, used mainly for condition-based maintenance. Generally, researchers have tried to find “universal” feature generation and feature reduction methods to derive distinctive fault features. The features then apply to a classification system that recognizes the fault name. This approach

has problems. For example, if a new class is taken into consideration, the extracted features can be ineffective at separating it out from existing classes, which can mean that extraction and selection algorithms need to be redesigned. To overcome those problems, we have found a way, which we believe to be the first of its kind, to accurately identify induction motor faults from vibration signals under noisy conditions; our system can also cope with a new group in the classification system. Our proposed algorithm, a viable alternative to online detection of induction motor defects, considers the differences in the fault-related frequencies in vibration signals. The features extracted from each specific fault differ from those of other faults. We can then use a modified minimum distance classifier to improve classification performance. Our experiments revealed that our technique shows a clear advantage over existing methods in classification accuracy in both noiseless and additive white Gaussian noise circumstances.

## **Chapter 7**

### **Heatmap-based Leakage Localization Algorithm using Acoustic Emission Sensor for Circulating Fluidized Bed Combustion Boiler Tube**

#### **7.1 Introduction**

The importance of efficient energy conversion such as waste and biomass as a new renewable energy source that can replace coal required for thermal power generation is more emphasized as the recent high oil price situation continues, and environmental pollution problems emerge. Thermal power generation using a circulating fluidized bed boiler not only reduces the emission of nitrogen oxides (NO<sub>x</sub>) and sulfur oxides (SO<sub>x</sub>), which are the main causes of environmental pollution, but also can directly burn various fuels such as wastes other than coal and biomass. It is a thermal power generation method that is in the spotlight as [127]. However, the fluid medium, which is the main combustion target of the circulating fluidized bed boiler, is a small but hard pulverized coal-like solid, which hits and wears the water wall tube in the furnace. This causes steam leakage in the tube, which not only reduces the thermal conductivity of the circulating fluidized bed boiler, but also leads to shutdown, resulting in enormous economic losses [128].

In this study, a heatmap-based circulating fluidized bed boiler tube leakage location estimation algorithm was developed, which uses an acoustic emission sensor that can express the leakage location and degree of leakage in a heatmap of a circulating fluidized bed boiler for thermal power generation using an acoustic emission sensor. To verify the performance of the proposed algorithm, after attaching a 4-channel acoustic emission sensor to the testbed of the circulating fluidized bed boiler tube, the leakage location was estimated by collecting the acoustic emission signal of an artificial leakage.

## 7.2 Proposed Methodology

### 7.2.1 Sensor localization method

To estimate the sensor coordinates, the distance between each sensor of 4 channels is measured. The measured distance between sensors is defined as  $d_{ij}$ , which means the distance between the  $i$ -channel sensor and the  $j$ -channel sensor. The ruler of each sensor is calculated by solving the equation between the measured distance between sensors and the distance calculated through the coordinates of the sensors. The flow chart of the sensor coordinate estimation algorithm is shown in Figure 7.1.

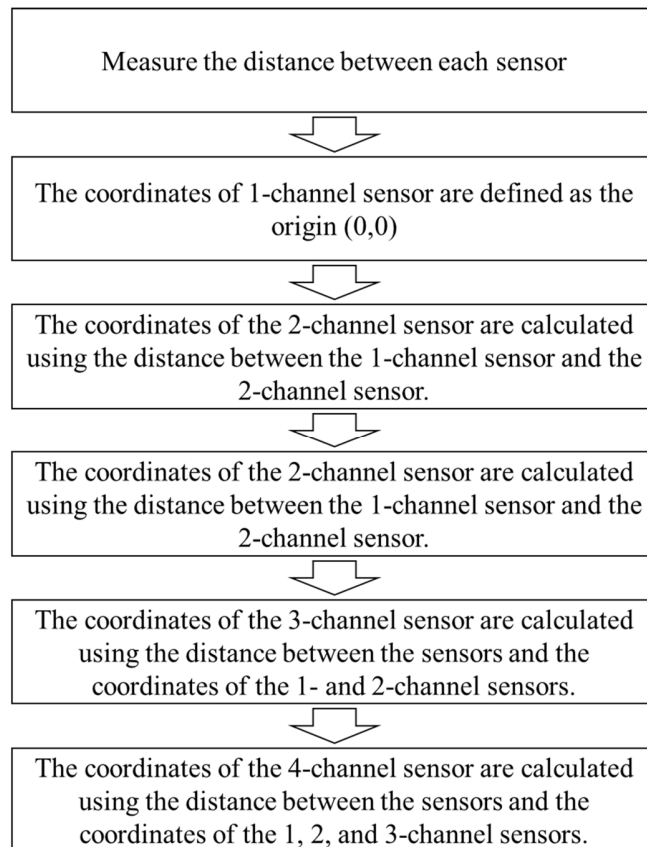


**Figure 7.1** A block diagram of sensor localization algorithm

The coordinates of the 1-channel sensor and 2-channel sensor are defined as in Equation (7.1).

$$S_1 = (0,0), \quad S_2 = (dist_{12}, 0). \quad (7.1)$$

The distance between the 1-channel sensor and the 3-channel sensor is calculated by Equation (7.2), and the distance between the 2-channel sensor and the 3-channel sensor is calculated by Equation (7.3).

$$(dist_{12})^2 = x_3^2 + y_3^2. \quad (7.2)$$

$$(dist_{23})^2 = x_2^2 - 2x_2x_3 + x_3^2 + y_3^2. \quad (7.3)$$

Through the system of Equations (7.2) and (7.3), the  $x$  and  $y$  coordinates of the 3-channel sensor can be calculated as in Equations (7.4) and (7.5), respectively.

$$x_3 = (x_2^2 + (dist_{13})^2 - (dist_{23})^2). \quad (7.4)$$

$$y_3 = \sqrt{(dist_{13})^2 - x_3^2}. \quad (7.5)$$

### 7.2.2 Leakage localization method using heatmap

Since the boiler water wall tube is welded between the membrane and the tube, the signal attenuation rate of the welded part and the non-welded part is different. After measuring the signal attenuation rate through an experiment, it is possible to calculate the amplitude weight for each position of the acoustic emission signal through Equation (7.6).

$$E_i(x, y) = \frac{(x - x_i)^2}{r_1} + \frac{(y - y_i)^2}{r_2}, i = 1, 2, 3, 4. \quad (7.6)$$

The heatmap can be calculated as the sum of the product of each sensor weight and the amplitude level of the signal collected from the corresponding sensor.

$$HW = \sum_{i=1}^4 E_i \cdot A_i \quad (7.7)$$

## 7.3 Experimental Setup

To verify the technology proposed in this study, a circulating fluidized bed boiler simulation

testbed was used. An artificial pinhole simulation system that can be opened and closed using a solenoid valve was used to simulate the pores. Figure 7.2 is a conceptual diagram of the artificial pinhole simulation system used in the experiment.

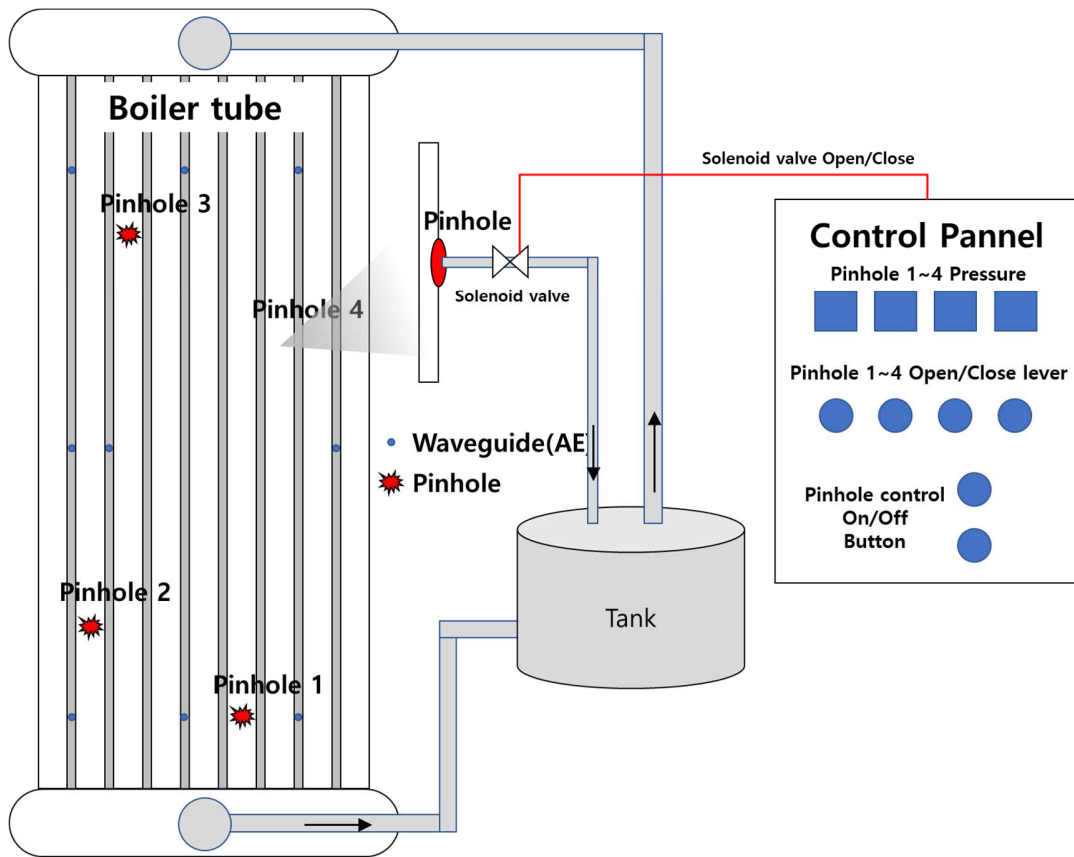


**Figure 7.2** A scheme of CFBC testbed for imitating tube leakage

The leakage of artificial pinholes in four different locations is connected to the tank through a pipe, and the leakage of the pinhole can be controlled through an electrically controlled solenoid valve and a control panel. Figure 7.3 shows a photograph of an artificial pinhole installed in a circulating fluidized bed boiler testbed.

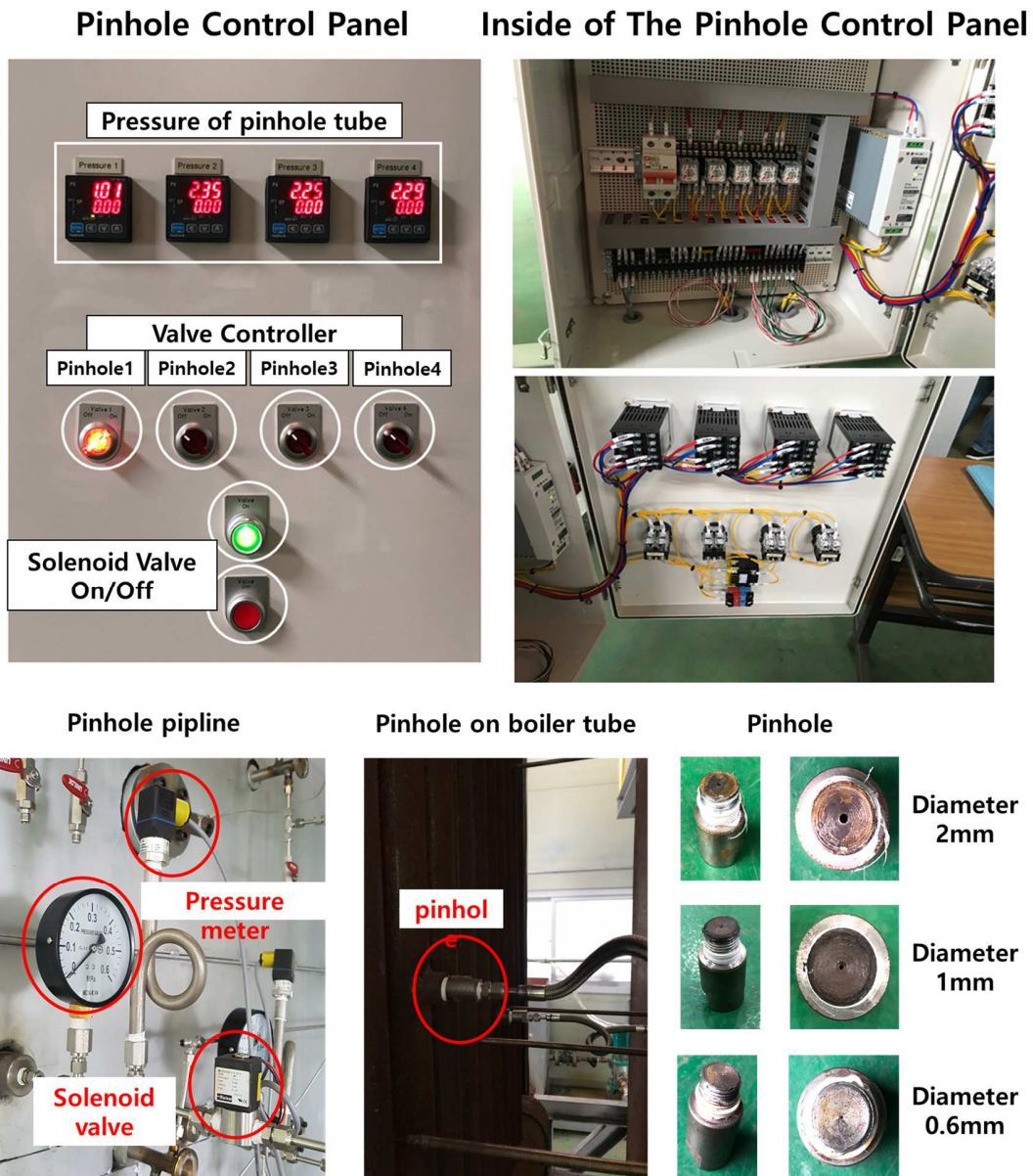


**Figure 7.3** Photographs of CFBC testbed for imitating tube leakage

### 7.4 Experimental Result

Figure 7.4 shows the heatmap according to the amplitude of the acoustic emission signal due to leakage of the 0.6mm pinhole located at the top and the upper left of the boiler tube. The part close to blue has low amplitude and the part close to red has high amplitude. The black dot means the sensor location for each channel. The blue circle marks a location near 99% of the maximum amplitude. As shown in Figure 7.4, all parts are marked with a color close to blue at the top, and a color close to red near the pinhole at 0.6mm pinholes.

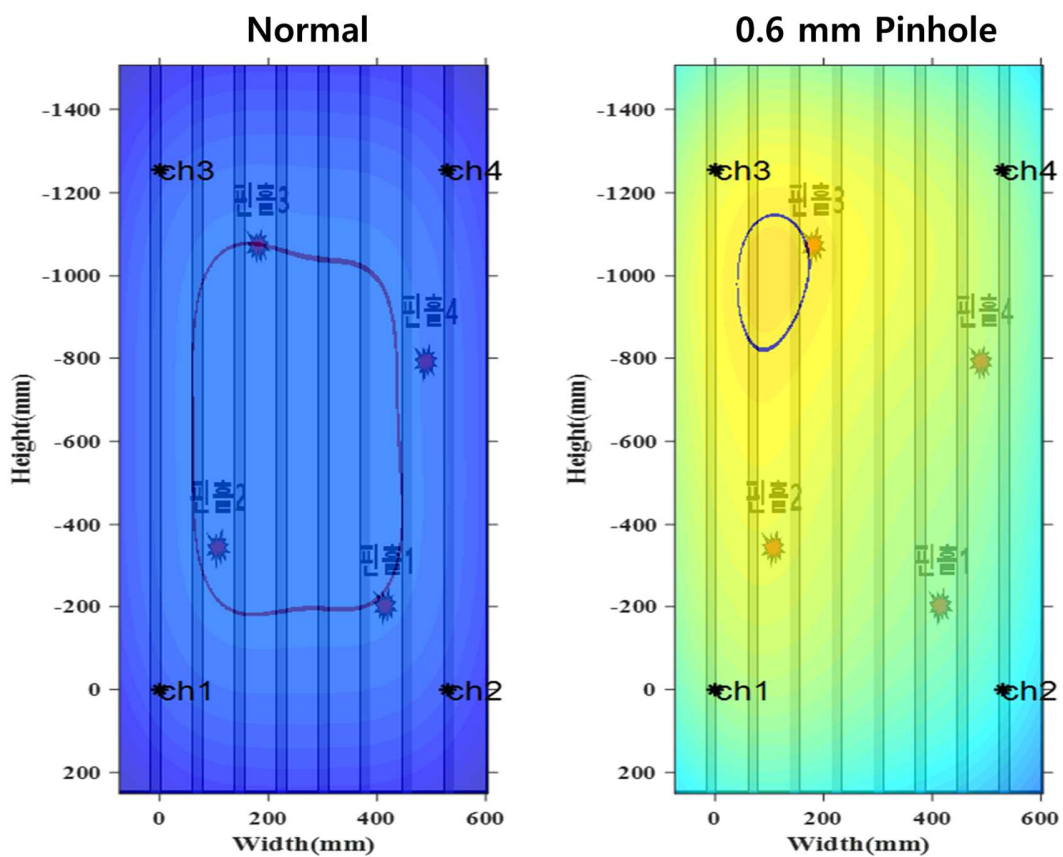


Figure 7.4 A concept of CFBC testbed for imitating tube leakage

## **7.5 Conclusions**

In this study, a heatmap-based location estimation algorithm is proposed using an acoustic emission sensor. The proposed algorithm consists of an algorithm for estimating sensor coordinates based on the distance between sensors and an algorithm for estimating the location of the leakage considering the damping rate of the membrane weld of the boiler water wall tube. The effectiveness of the algorithm was verified through an artificial leak experiment using a circulating fluidized bed boiler testbed.

## Chapter 8

### Summary of Contributions and Future Works

#### 8.1 Introduction

The main contributions of this dissertation and future aspects of the current work are given in this chapter. Section 8.2 highlights the main contributions of this dissertation whereas future research direction is given in section 8.3.

#### 8.2 Summary of Contributions

The dissertation has focused on deep-learning and machine-learning-based fault diagnosis of industrial equipment. It covers the fault diagnosis of three types of industrial equipment, i.e., rotary machine bearings, induction motors, and CFBC boiler tube. Chapter 2 to 4 are about the deep-learning-based fault diagnosis of bearings while chapter 5 and 6 focus on machine-learning-based fault diagnosis of bearings and induction motors, respectively. In chapter 7, CFBC boiler tube leakage detection and localization methods are introduced. The contributions of this dissertation to fault diagnosis are given below:

- A new CNN-based rolling element bearing fault diagnosis approach was presented in chapter 2. The Proposed algorithm performs reliable fault diagnosis of bearings by resolving two issues; The first issue is that the trained neural network, in general, can be only reliable on the specific machine since the patterns of the raw signals strongly depend on the operating conditions of the machinery such as load, installation, external vibration, etc. The second concern is that the trained feature representation is uninterpretable due to the black box-like operation of the neural networks. To address the first issue, the proposed method utilizes NBCC as the input data of CNN rather than raw AE signal itself. Since the bearing characteristic frequencies are induced by appearing bearing failures, NBCC is a more effective representation for diagnosing the bearing failure symptoms. To resolve the second issue, this research applies Grad-CAM to visualize important regions in NBCC.
- In chapter 3, a new method to find a 2D-representation of AE signal is proposed based on the defect characteristic frequencies of bearing. This methodology generates SESI.

The SESI, which is constructed from envelope spectrum of vibration signal and filtered by frequency range covering the bearing characteristic frequencies, is considered as the new signature for different type of faults in bearing and is used to input to the classifier. The author also proposed a structure of CNN for classification different type of bearing defect by learning and extracting the knowledge from the SESI. The proposed methods solved two issues: 1) relevant feature extractions, 2) generalization of feature representations. In experiment, this study compares the classification accuracy of proposed method and traditional methods using dataset measured on two different machines. To validate performance of feature learning, the method is trained for one machine and tested for the other machine without any retraining process. In the experiment of learning the dataset of the laboratory-designed testbed and classifying the dataset of the RK-4 testbed, the existing algorithm achieved 42.7%, while the proposed algorithm achieved 94.5%.

- In chapter 4, a novel 2-D representation method is created by combining CWT with filtering by the frequency range covering the bearing defect frequencies to generate DSWI. The constructed DSWI is considered as the new signature, which solves the modulation problem, reduces the nonstationary effect in the signal, demonstrates the distinct patterns for the different types of faults in bearings, and closely relates to the defect frequencies in the envelope spectrum. This study also introduces a specific architecture of CNN for classifying multiple fault types that occur in bearings by learning the specific features from the DSWI representations. To estimate the performance of the proposed approach, it has been evaluated using the laboratory dataset collected from the bearing testbed. Finally, the results of the proposed method are compared with other methods presented in the literature.
- In chapter 5, an improved feature extraction method is proposed to diagnose incipient bearing defects. The proposed method decomposes the raw AE signal into different sub-band signals using DWPT, which is more effective for the multiresolution analysis of non-stationary signals. A feature vector is extracted from each sub-band signal, resulting in multiple feature vectors from the raw AE signal. In contrast, traditional feature extraction methods extract a single feature vector from the raw AE signal. The feature vectors extracted from different sub-bands of the original AE signal result in

models of the fault data that are discriminatory, even under variations in the rotational speed. WCM, which is an ensemble of SVMs and ANNs, is employed to build discriminatory models of the feature vectors for different bearing defects.

- The study in chapter 6 aims to design and develop an effective method to generate different features to enhance the performance of a diagnosis system that will be able to learn new class signatures. Spectral envelopes and fast Fourier transforms was used to specify the harmonic components of a vibration signal. These signals model a particular motor failure signature such that the system can detect and classify comprehensive fault conditions in induction motors. With subsequent vibration readings taken under identical conditions, we can determine whether any deterioration that affects the vibration signatures has taken place in the machine's condition. In the classification task, Mahalanobis distances between a test sample and known faulty signatures was used to measure the similarity between the sample and the signatures, so that the minimum distance indicates the name of the fault.
- In chapter 7, a heatmap-based circulating fluidized bed boiler tube leakage location estimation algorithm was developed, which uses an acoustic emission sensor that can express the leakage location and degree of leakage in a heatmap of a circulating fluidized bed boiler for thermal power generation using an acoustic emission sensor. To verify the performance of the proposed algorithm, after attaching a 4-channel acoustic emission sensor to the testbed of the circulating fluidized bed boiler tube, the leakage location was estimated by collecting the acoustic emission signal of an artificial leakage.

### 8.3 Future Works

This dissertation presents and discusses deep-learning and machine-learning-based fault diagnosis of industrial equipment. Chapter 2 to 7 summarized contributions and the investigations carried out on the topics. Although, the study shows thoroughbred performance of fault diagnosis, some of these future topics are presented below:

- Although it is true that the deep learning-based fault diagnosis method has superior performance compared to the existing machine learning-based fault diagnosis method,

the deep learning-based fault diagnosis method requires a large amount of data. However, it is difficult to secure a large amount of equipment failure data in an actual industrial site. Therefore, there is a need for continuous research on deep learning algorithms that can provide sufficient diagnostic performance even when the amount of data is small.

- There is a limit to researching fault diagnosis technology through data collected using a testbed, and it is difficult to guarantee the reliability of the technology when applied to the field. Therefore, there is a need for a study on a technology that can generalize a deep learning model learned from data acquired in a specific environment, such as transfer learning.
- Furthermore, there is a need for research and development of software and platforms that can fully utilize data-driven fault diagnosis methods. For example, there are studies on the database structure, a framework for learning, updating, and utilizing AI-based fault diagnosis, and a framework for analyzing and managing big data.

## Publications

- [1] **J. Kim**, M. Kang, M. S. Islam, C.-H. Kim, and J.-M. Kim, “A fast and energy-efficient Hamming decoder for software-defined radio using graphics processing units,” *J Supercomput*, vol. 71, no. 7, pp. 2454–2472, Jul. 2015, doi: 10.1007/s11227-015-1396-x.
- [2] M. Kang, M. R. Islam, **J. Kim**, J. Kim, and M. Pecht, “A Hybrid Feature Selection Scheme for Reducing Diagnostic Performance Deterioration Caused by Outliers in Data-Driven Diagnostics,” *IEEE Transactions on Industrial Electronics*, vol. 63, no. 5, pp. 3299–3310, May 2016, doi: 10.1109/TIE.2016.2527623.
- [3] M. Kang, J. Kim, I. Jeong, **J. Kim**, and M. Pecht, “A Massively Parallel Approach to Real-Time Bearing Fault Detection Using Sub-Band Analysis on an FPGA-Based Multicore System,” *IEEE Transactions on Industrial Electronics*, vol. 63, no. 10, pp. 6325–6335, Oct. 2016, doi: 10.1109/TIE.2016.2574986.
- [4] J. Kim, H. N. Ngoc, and **J. Kim**, “A New Fault Classification Scheme Using Vibration Signal Signatures and the Mahalanobis Distance,” in *Integrated Uncertainty in Knowledge Modelling and Decision Making*, Cham, 2016, pp. 230–241, doi: 10.1007/978-3-319-49046-5\_20.
- [5] M.-G. Choi, **J.-Y. Kim**, I. Jeong, Y.-H. Kim, and J.-M. Kim, “A Real-Time Monitoring System for Boiler Tube Leakage Detection,” in *Hybrid Intelligent Systems*, Cham, 2020, pp. 106–114, doi: 10.1007/978-3-030-14347-3\_11.
- [6] V. Tra, S. Uddin, **J. Kim**, C.-H. Kim, and J. Kim, “Accelerating Envelope Analysis-Based Fault Diagnosis Using a General-Purpose Graphics Processing Unit,” in *Integrated Uncertainty in Knowledge Modelling and Decision Making*, Cham, 2016, pp. 409–420, doi: 10.1007/978-3-319-49046-5\_35.
- [7] **J. Kim**, I. Jeong, and J.-M. Kim, “Acoustic Emission based Early Fault Detection and Diagnosis Method for Pipeline,” *Asia-pacific Journal of Multimedia Services Convergent with Art, Humanities, and Sociology*, vol. 8, no. 3, pp. 571–578, Mar. 2018.
- [8] B. P. Duong, **J. Kim**, I. Jeong, C. H. Kim, and J.-M. Kim, “Acoustic Emission Burst Extraction for Multi-Level Leakage Detection in a Pipeline,” *Applied Sciences*, vol. 10, no. 6, Art. no. 6, Jan. 2020, doi: 10.3390/app10061933.
- [9] V. Tra, **J.-Y. Kim**, I. Jeong, and J. Kim, “An Acoustic Emission Technique for Crack Modes Classification in Concrete Structures,” *Sustainability*, vol. 12, p. 6724, Aug. 2020, doi: 10.3390/su12176724.
- [10] N. N. Hung, **J. Kim**, and J.-M. Kim, “An Effective Envelope Analysis Using Gaussian Windows for Evaluation of Fault Severity in Bearing,” in *Information Science and Applications 2018*, Singapore, 2019, pp. 457–464, doi: 10.1007/978-981-13-1056-0\_46.
- [11] M. Kang, **J. Kim**, and J. Kim, “An FPGA-Based Multicore System for Real-Time Bearing Fault Diagnosis Using Ultrasampling Rate AE Signals,” *IEEE Transactions on Industrial Electronics*, vol. 62, no. 4, pp. 2319–2329, Apr. 2015, doi: 10.1109/TIE.2014.2361317.
- [12] S.-J. Kang, **J.-Y. Kim**, I.-K. Jeong, M. M. M. Islam, K. Im, and J.-M. Kim, “An Improved Gas Classification Technique Using New Features and Support Vector Machines,” in *Proceedings of the Tenth International Conference on Soft Computing and Pattern Recognition (SoCPaR 2018)*, Cham, 2020, pp. 158–166, doi: 10.1007/978-3-030-17065-3\_16.

- [13] A. Prosvirin, **J. Kim**, and J.-M. Kim, “Bearing Fault Diagnosis Based on Convolutional Neural Networks with Kurtogram Representation of Acoustic Emission Signals,” in *Advances in Computer Science and Ubiquitous Computing*, Singapore, 2018, pp. 21–26, doi: 10.1007/978-981-10-7605-3\_4.
- [14] V. Tra, **J. Kim**, S. A. Khan, and J.-M. Kim, “Bearing Fault Diagnosis under Variable Speed Using Convolutional Neural Networks and the Stochastic Diagonal Levenberg-Marquardt Algorithm,” *Sensors (Basel)*, vol. 17, no. 12, Dec. 2017, doi: 10.3390/s17122834.
- [15] **J. Kim** and J.-M. Kim, “Bearing Fault Diagnosis Using Grad-CAM and Acoustic Emission Signals,” *Applied Sciences*, vol. 10, no. 6, Art. no. 6, Jan. 2020, doi: 10.3390/app10062050.
- [16] M. Islam, M. Sohaib, **J. Kim**, and J.-M. Kim, “Crack Classification of a Pressure Vessel Using Feature Selection and Deep Learning Methods,” *Sensors (Basel)*, vol. 18, no. 12, Dec. 2018, doi: 10.3390/s18124379.
- [17] B. P. Duong, **J. Kim**, C.-H. Kim, and J.-M. Kim, “Deep Learning Object-Impulse Detection for Enhancing Leakage Detection of a Boiler Tube Using Acoustic Emission Signal,” *Applied Sciences*, vol. 9, no. 20, Art. no. 20, Jan. 2019, doi: 10.3390/app9204368.
- [18] M. R. Islam, Y.-H. Kim, **J.-Y. Kim**, and J.-M. Kim, “Detecting and Learning Unknown Fault States by Automatically Finding the Optimal Number of Clusters for Online Bearing Fault Diagnosis,” *Applied Sciences*, vol. 9, no. 11, Art. no. 11, Jan. 2019, doi: 10.3390/app9112326.
- [19] Y.-H. Kim, I.-K. Jeong, **J.-Y. Kim**, J.-K. Ban, and J.-M. Kim, “Development of an Intelligent Diagnosis System for Detecting Leakage of Circulating Fluidized Bed Boiler Tubes,” in *Hybrid Intelligent Systems*, Cham, 2020, pp. 311–320, doi: 10.1007/978-3-030-14347-3\_30.
- [20] S. Uddin *et al*(**J. Kim**), “Distance and Density Similarity Based Enhanced k -NN Classifier for Improving Fault Diagnosis Performance of Bearings,” *Shock and Vibration*, vol. 2016, pp. 1–11, Jan. 2016, doi: 10.1155/2016/3843192.
- [21] A. Prosvirin, **J. Kim**, and J.-M. Kim, “Efficient Rub-Impact Fault Diagnosis Scheme Based on Hybrid Feature Extraction and SVM,” in *Advances in Computer Communication and Computational Sciences*, Singapore, 2019, pp. 405–415, doi: 10.1007/978-981-13-0341-8\_37.
- [22] Y.-J. Cho, **J. Kim**, and J.-M. Kim, “Efficient Transformer Dissolved Gas Analysis and Classification Method,” *Asia-pacific Journal of Multimedia Services Convergent with Art, Humanities, and Sociology*, vol. 8, no. 3, pp. 563–570, Mar. 2018.
- [23] I.-K. Jeong, M. Kang, **J. Kim**, J. Kim, J.-M. Ha, and B.-K. Choi, “Enhanced DET-Based Fault Signature Analysis for Reliable Diagnosis of Single and Multiple-Combined Bearing Defects,” *Shock and Vibration*, vol. 2015, pp. 1–10, Nov. 2015, doi: 10.1155/2015/814650.
- [24] M. Kang, **J. Kim**, B.-K. Choi, and J.-M. Kim, “Envelope analysis with a genetic algorithm-based adaptive filter bank for bearing fault detection,” *The Journal of the Acoustical Society of America*, vol. 138, no. 1, pp. EL65–EL70, Jul. 2015, doi: 10.1121/1.4922767.
- [25] V. Tra, **J. Kim**, and J.-M. Kim, “Fault Diagnosis of Bearings with Variable Rotational Speeds Using Convolutional Neural Networks,” in *Advances in Computer*

- Communication and Computational Sciences*, Singapore, 2019, pp. 71–81, doi: 10.1007/978-981-13-0341-8\_7.
- [26] M. J. Hasan, **J. Kim**, C. H. Kim, and J.-M. Kim, “Health State Classification of a Spherical Tank Using a Hybrid Bag of Features and K-Nearest Neighbor,” *Applied Sciences*, vol. 10, no. 7, Art. no. 7, Jan. 2020, doi: 10.3390/app10072525.
- [27] M. Kang, **J. Kim**, and J. Kim, “High-Performance and Energy-Efficient Fault Diagnosis Using Effective Envelope Analysis and Denoising on a General-Purpose Graphics Processing Unit,” *IEEE Transactions on Power Electronics*, vol. 30, no. 5, pp. 2763–2776, May 2015, doi: 10.1109/TPEL.2014.2356207.
- [28] V. Tra, B.-P. Duong, **J.-Y. Kim**, M. Sohaib, and J.-M. Kim, “Improving the Performance of Storage Tank Fault Diagnosis by Removing Unwanted Components and Utilizing Wavelet-Based Features,” *Entropy*, vol. 21, no. 2, Art. no. 2, Feb. 2019, doi: 10.3390/e21020145.
- [29] V. Tra, **J. Kim**, S. A. Khan, and J.-M. Kim, “Incipient fault diagnosis in bearings under variable speed conditions using multiresolution analysis and a weighted committee machine,” *J Acoust Soc Am*, vol. 142, no. 1, p. EL35, Jul. 2017, doi: 10.1121/1.4991329.
- [30] Y.-H. Kim, **J. Kim**, and J.-M. Kim, “Leakage Detection of a Boiler Tube Using a Genetic Algorithm-like Method and Support Vector Machines,” in *Proceedings of the Tenth International Conference on Soft Computing and Pattern Recognition (SoCPaR 2018)*, Cham, 2020, pp. 86–93, doi: 10.1007/978-3-030-17065-3\_9.
- [31] M. Sohaib, M. Islam, **J. Kim**, D.-C. Jeon, and J.-M. Kim, “Leakage Detection of a Spherical Water Storage Tank in a Chemical Industry Using Acoustic Emissions,” *Applied Sciences*, vol. 9, no. 1, Art. no. 1, Jan. 2019, doi: 10.3390/app9010196.
- [32] H. N. Nguyen, **J. Kim**, and J.-M. Kim, “Optimal Sub-Band Analysis Based on the Envelope Power Spectrum for Effective Fault Detection in Bearing under Variable, Low Speeds,” *Sensors*, vol. 18, no. 5, Art. no. 5, May 2018, doi: 10.3390/s18051389.
- [33] S.-B. Lee, **J. Kim**, C.-H. Kim, and J.-M. Kim, “Parameter Search Methodology of Support Vector Machines for Improving Performance,” *Asia-pacific Journal of Multimedia Services Convergent with Art, Humanities, and Sociology*, vol. 7, no. 3, pp. 329–337, Mar. 2017.
- [34] Y.-J. Cho, **J. Kim**, and J.-M. Kim, “Performance Improvement of Bearing Fault Diagnosis using a Real-Time Training Method,” *Asia-pacific Journal of Multimedia Services Convergent with Art, Humanities, and Sociology*, vol. 7, no. 4, pp. 551–559, Apr. 2017.
- [35] **J. Kim**, M. Kang, I. Jeong, H. Jun, J. Kim, and B. Choi, “Real-time and energy-efficient bearing fault diagnosis using discriminative wavelet-based fault features on a multi-core system,” in *2015 IEEE Conference on Prognostics and Health Management (PHM)*, Jun. 2015, pp. 1–11, doi: 10.1109/ICPHM.2015.7245019.
- [36] M. M. M. Islam, **J. Kim**, S. A. Khan, and J.-M. Kim, “Reliable bearing fault diagnosis using Bayesian inference-based multi-class support vector machines,” *The Journal of the Acoustical Society of America*, vol. 141, no. 2, pp. EL89–EL95, Feb. 2017, doi: 10.1121/1.4976038.
- [37] M. Kang, **J. Kim**, J.-M. Kim, A. C. C. Tan, E. Y. Kim, and B. Choi, “Reliable Fault Diagnosis for Low-Speed Bearings Using Individually Trained Support Vector Machines With Kernel Discriminative Feature Analysis,” *IEEE Transactions on Power Electronics*, vol. 30, no. 5, pp. 2786–2797, May 2015, doi: 10.1109/TPEL.2014.2358494.

- [38] A. E. Prosvirin, M. Islam, **J. Kim**, and J.-M. Kim, “Rub-Impact Fault Diagnosis Using an Effective IMF Selection Technique in Ensemble Empirical Mode Decomposition and Hybrid Feature Models,” *Sensors*, vol. 18, no. 7, Art. no. 7, Jul. 2018, doi: 10.3390/s18072040.
- [39] M. Kang, **J. Kim**, L. M. Wills, and J. Kim, “Time-Varying and Multiresolution Envelope Analysis and Discriminative Feature Analysis for Bearing Fault Diagnosis,” *IEEE Transactions on Industrial Electronics*, vol. 62, no. 12, pp. 7749–7761, Dec. 2015, doi: 10.1109/TIE.2015.2460242.

## References

- [1] D. J. Liu, “Application of risk based inspection (RBI), reliability centered maintenance (RCM) and risk based maintenance (RBM),” 2013, Accessed: Jan. 14, 2021. [Online]. Available: <https://uis.brage.unit.no/uis-xmlui/handle/11250/183648>.
- [2] E. Özcan, R. Yumuşak, and T. Eren, “Risk Based Maintenance in the Hydroelectric Power Plants,” *Energies*, vol. 12, no. 8, Art. no. 8, Jan. 2019, doi: 10.3390/en12081502.
- [3] F. Khan and M. Haddara, “Risk-Based Maintenance (RBM): A new approach for process plant inspection and maintenance,” *Process Safety Progress*, vol. 23, pp. 252–265, Dec. 2004, doi: 10.1002/prs.10010.
- [4] R. M. C. Ratnayake and K. Antosz, “Development of a Risk Matrix and Extending the Risk-based Maintenance Analysis with Fuzzy Logic,” *Procedia Engineering*, vol. 182, pp. 602–610, Jan. 2017, doi: 10.1016/j.proeng.2017.03.163.
- [5] M. Yazdi, A. Nedjati, and R. Abbassi, “Fuzzy dynamic risk-based maintenance investment optimization for offshore process facilities,” *Journal of Loss Prevention in the Process Industries*, vol. 57, pp. 194–207, Jan. 2019, doi: 10.1016/j.jlp.2018.11.014.
- [6] K. Patan, *Artificial Neural Networks for the Modelling and Fault Diagnosis of Technical Processes*, vol. 377. Springer-Verlag Berlin Heidelberg: Springer, Berlin, Heidelberg, 2008.
- [7] M. G. Pecht and M. Kang, *Prognostics and Health Management of Electronics: Fundamentals, Machine Learning, and the Internet of Things*. Wiley-IEEE Press, 2018.
- [8] Z. Gao, C. Cecati, and S. X. Ding, “A Survey of Fault Diagnosis and Fault-Tolerant Techniques—Part I: Fault Diagnosis With Model-Based and Signal-Based Approaches,” *IEEE Transactions on Industrial Electronics*, vol. 62, no. 6, pp. 3757–3767, Jun. 2015, doi: 10.1109/TIE.2015.2417501.
- [9] Z. Gao, C. Cecati, and S. X. Ding, “A Survey of Fault Diagnosis and Fault-Tolerant Techniques—Part II: Fault Diagnosis With Knowledge-Based and Hybrid/Active Approaches,” *IEEE Transactions on Industrial Electronics*, vol. 62, no. 6, pp. 3768–3774, Jun. 2015, doi: 10.1109/TIE.2015.2419013.
- [10] F. Piltan and J.-M. Kim, “Bearing Fault Diagnosis Using an Extended Variable Structure Feedback Linearization Observer,” *Sensors*, vol. 18, no. 12, Art. no. 12, Dec. 2018, doi: 10.3390/s18124359.
- [11] X. Yu, E. Ding, C. Chen, X. Liu, and L. Li, “A Novel Characteristic Frequency Bands Extraction Method for Automatic Bearing Fault Diagnosis Based on Hilbert Huang Transform,” *Sensors*, vol. 15, no. 11, Art. no. 11, Nov. 2015, doi: 10.3390/s151127869.
- [12] J. Seshadrinath, B. Singh, and B. K. Panigrahi, “Investigation of Vibration Signatures for Multiple Fault Diagnosis in Variable Frequency Drives Using Complex Wavelets,” *IEEE Transactions on Power Electronics*, vol. 29, no. 2, pp. 936–945, Feb. 2014, doi: 10.1109/TPEL.2013.2257869.
- [13] T. W. Rauber, F. de A. Boldt, and F. M. Varejão, “Heterogeneous Feature Models and Feature Selection Applied to Bearing Fault Diagnosis,” *IEEE Transactions on Industrial Electronics*, vol. 62, no. 1, pp. 637–646, Jan. 2015, doi: 10.1109/TIE.2014.2327589.
- [14] M. Kang, J. Kim, L. M. Wills, and J. Kim, “Time-Varying and Multiresolution Envelope Analysis and Discriminative Feature Analysis for Bearing Fault Diagnosis,” *IEEE*

- Transactions on Industrial Electronics*, vol. 62, no. 12, pp. 7749–7761, Dec. 2015, doi: 10.1109/TIE.2015.2460242.
- [15] E. Price, A. Lees, and M. Friswell, “Detection of severe sliding and pitting fatigue wear regimes through the use of broadband acoustic emission,” *Proceedings of The Institution of Mechanical Engineers Part J-journal of Engineering Tribology - PROC INST MECH ENG J-J ENG TR*, vol. 219, Apr. 2005, doi: 10.1243/135065005X9817.
- [16] H. Henao *et al.*, “Trends in Fault Diagnosis for Electrical Machines: A Review of Diagnostic Techniques,” *IEEE Industrial Electronics Magazine*, vol. 8, no. 2, pp. 31–42, Jun. 2014, doi: 10.1109/MIE.2013.2287651.
- [17] J. G. Ritchey and D. A. Wagner, “Electrical machines such as generators and motors.” Google Patents, Mar. 07, 2017.
- [18] N. Boro, H. Das, A. Ghosh, and G. Roy, “Vibrational signal analysis for bearing fault detection in mechanical systems,” in *Foundations and Frontiers in Computer, Communication and Electrical Engineering: Proceedings of the 3rd International Conference on Foundations and Frontiers in Computer, Communication and Electrical Engineering, 2016 (C2E2-2016)*, 2016, pp. 63–67.
- [19] M. Grujicic, S. Ramaswami, R. Yavari, R. Galgalikar, V. Chenna, and J. S. Snipes, “Multiphysics computational analysis of white-etch cracking failure mode in wind turbine gearbox bearings,” *Proceedings of the Institution of Mechanical Engineers, Part L: Journal of Materials: Design and Applications*, vol. 230, no. 1, pp. 43–63, 2016.
- [20] S. A. Khan and J.-M. Kim, “Rotational speed invariant fault diagnosis in bearings using vibration signal imaging and local binary patterns,” *The Journal of the Acoustical Society of America*, vol. 139, no. 4, pp. EL100–EL104, 2016.
- [21] C. Vilcu, F. Niculescu, A. Mitru, C. Nechifor, C.-I. Borzea, and C. Cornea, “‘HolderCPS’-A new type data recorder system for proactive maintenance to rotary blade machines,” in *2017 10th International Symposium on Advanced Topics in Electrical Engineering (ATEE)*, 2017, pp. 655–660.
- [22] D. K. Appana, M. R. Islam, and J.-M. Kim, “Reliable fault diagnosis of bearings using distance and density similarity on an enhanced k-NN,” in *Australasian Conference on Artificial Life and Computational Intelligence*, 2017, pp. 193–203.
- [23] M. M. M. Islam, J. Kim, S. A. Khan, and J.-M. Kim, “Reliable bearing fault diagnosis using Bayesian inference-based multi-class support vector machines,” *The Journal of the Acoustical Society of America*, vol. 141, no. 2, pp. EL89–EL95, 2017.
- [24] B. Samanta and K. R. Al-Balushi, “Artificial neural network based fault diagnostics of rolling element bearings using time-domain features,” *Mechanical systems and signal processing*, vol. 17, no. 2, pp. 317–328, 2003.
- [25] J. Yu, X. Yang, F. Gao, and D. Tao, “Deep multimodal distance metric learning using click constraints for image ranking,” *IEEE transactions on cybernetics*, vol. 47, no. 12, pp. 4014–4024, 2017.
- [26] M. Gharbi, J. Chen, J. T. Barron, S. W. Hasinoff, and F. Durand, “Deep bilateral learning for real-time image enhancement,” *ACM Transactions on Graphics (TOG)*, vol. 36, no. 4, p. 118, 2017.
- [27] Y. Zhang, M. Pezeshki, P. Brakel, S. Zhang, C. L. Y. Bengio, and A. Courville, “Towards end-to-end speech recognition with deep convolutional neural networks,” *arXiv preprint arXiv:1701.02720*, 2017.

- [28] G. Brunner, Y. Wang, R. Wattenhofer, and M. Weigelt, "Natural Language Multitasking: Analyzing and Improving Syntactic Saliency of Hidden Representations," *arXiv preprint arXiv:1801.06024*, 2018.
- [29] S. Poornachandra and C. Naveena, "Pre-processing of MR Images for Efficient Quantitative Image Analysis using Deep Learning Techniques," in *2017 International Conference on Recent Advances in Electronics and Communication Technology (ICRAECT)*, 2017, pp. 191–195.
- [30] S. Nandi and H. A. Toliyat, "Condition monitoring and fault diagnosis of electrical machines-a review," in *Conference Record of the 1999 IEEE Industry Applications Conference. Thirty-Forth IAS Annual Meeting (Cat. No.99CH36370)*, Oct. 1999, vol. 1, pp. 197–204 vol.1, doi: 10.1109/IAS.1999.799956.
- [31] M. Elforjani and D. Mba, "Accelerated natural fault diagnosis in slow speed bearings with Acoustic Emission," *Eng. Fract. Mech.*, vol. 77, no. 1, pp. 112–127, Jan. 2010, doi: 10.1016/j.engfracmech.2009.09.016.
- [32] V. Tra, S. A. Khan, and J.-M. Kim, "Diagnosis of bearing defects under variable speed conditions using energy distribution maps of acoustic emission spectra and convolutional neural networks," *The Journal of the Acoustical Society of America*, vol. 144, no. 4, pp. EL322–EL327, Oct. 2018, doi: 10.1121/1.5065071.
- [33] A. Prosvirin, J. Kim, and J.-M. Kim, "Bearing Fault Diagnosis Based on Convolutional Neural Networks with Kurtogram Representation of Acoustic Emission Signals," in *Advances in Computer Science and Ubiquitous Computing*, Singapore, 2018, pp. 21–26, doi: 10.1007/978-981-10-7605-3\_4.
- [34] M. R. Islam, J. Uddin, and J.-M. Kim, "Acoustic emission sensor network based fault diagnosis of induction motors using a gabor filter and multiclass support vector machines," *Ad hoc Sens. Wirel. Ne.*, 2016, Accessed: Feb. 23, 2020. [Online]. Available: <http://dspace.bracu.ac.bd/xmlui/handle/10361/9576>.
- [35] H. Sun, C. Wu, X. Liang, and Q. Zeng, "Identification of Multiple Faults in Gearbox Based on Multipoint Optional Minimum Entropy Deconvolution Adjusted and Permutation Entropy," *Entropy*, vol. 20, no. 11, p. 850, Nov. 2018, doi: 10.3390/e20110850.
- [36] Z. Li, J. Ma, X. Wang, and J. Wu, "MVMD-MOMEDA-TEO Model and Its Application in Feature Extraction for Rolling Bearings," *Entropy*, vol. 21, no. 4, p. 331, Apr. 2019, doi: 10.3390/e21040331.
- [37] W. Cai and Z. Wang, "Application of an Improved Multipoint Optimal Minimum Entropy Deconvolution Adjusted for Gearbox Composite Fault Diagnosis," *Sensors*, vol. 18, no. 9, Art. no. 9, Sep. 2018, doi: 10.3390/s18092861.
- [38] K. Wasmer, F. Saeidi, B. Meylan, T. Le Quang, and S. Shevchik, "When AE (Acoustic Emission) meets AI (Artificial Intelligence) II," Sep. 2018.
- [39] M. M. M. Islam and J.-M. Kim, "Automated bearing fault diagnosis scheme using 2D representation of wavelet packet transform and deep convolutional neural network," *Comput. Ind.*, vol. 106, pp. 142–153, Apr. 2019, doi: 10.1016/j.compind.2019.01.008.
- [40] M. J. Hasan, M. M. M. Islam, and J.-M. Kim, "Acoustic spectral imaging and transfer learning for reliable bearing fault diagnosis under variable speed conditions," *Measurement*, vol. 138, pp. 620–631, May 2019, doi: 10.1016/j.measurement.2019.02.075.

- [41] D. K. Appana, A. Prosvirin, and J.-M. Kim, “Reliable fault diagnosis of bearings with varying rotational speeds using envelope spectrum and convolution neural networks,” *Soft Comput*, vol. 22, no. 20, pp. 6719–6729, Oct. 2018, doi: 10.1007/s00500-018-3256-0.
- [42] V. Tra, J. Kim, and J.-M. Kim, “Fault Diagnosis of Bearings with Variable Rotational Speeds Using Convolutional Neural Networks,” in *Advances in Computer Communication and Computational Sciences*, Singapore, 2019, pp. 71–81, doi: 10.1007/978-981-13-0341-8\_7.
- [43] B. P. Duong and J.-M. Kim, “Fault Diagnosis of Multiple Combined Defects in Bearings Using a Stacked Denoising Autoencoder,” in *Advances in Computer Communication and Computational Sciences*, Singapore, 2019, pp. 83–93, doi: 10.1007/978-981-13-0341-8\_8.
- [44] V. Tra, J. Kim, S. A. Khan, and J.-M. Kim, “Bearing Fault Diagnosis under Variable Speed Using Convolutional Neural Networks and the Stochastic Diagonal Levenberg-Marquardt Algorithm,” *Sensors*, vol. 17, no. 12, Art. no. 12, Dec. 2017, doi: 10.3390/s17122834.
- [45] D. K. Appana, W. Ahmad, and J.-M. Kim, “Speed Invariant Bearing Fault Characterization Using Convolutional Neural Networks,” in *Multi-disciplinary Trends in Artificial Intelligence*, Cham, 2017, pp. 189–198, doi: 10.1007/978-3-319-69456-6\_16.
- [46] R. R. Selvaraju, M. Cogswell, A. Das, R. Vedantam, D. Parikh, and D. Batra, “Grad-CAM: Visual Explanations from Deep Networks via Gradient-Based Localization,” in *2017 IEEE International Conference on Computer Vision (ICCV)*, Oct. 2017, pp. 618–626, doi: 10.1109/ICCV.2017.74.
- [47] N. Wang and X. Liu, “Bearing Fault Diagnosis Method Based on Hilbert Envelope Demodulation Analysis,” *IOP Conference Series: Materials Science and Engineering*, vol. 436, p. 012009, Oct. 2018, doi: 10.1088/1757-899X/436/1/012009.
- [48] R. B. Randall and J. Antoni, “Rolling element bearing diagnostics—A tutorial,” *Mechanical Systems and Signal Processing*, vol. 25, no. 2, pp. 485–520, Feb. 2011, doi: 10.1016/j.ymsp.2010.07.017.
- [49] R. B. Randall and J. Antoni, “Rolling element bearing diagnostics—A tutorial,” *Mechanical Systems and Signal Processing*, vol. 25, no. 2, pp. 485–520, Feb. 2011, doi: 10.1016/j.ymsp.2010.07.017.
- [50] T. N. Sainath, A. Mohamed, B. Kingsbury, and B. Ramabhadran, “Deep convolutional neural networks for LVCSR,” in *2013 IEEE International Conference on Acoustics, Speech and Signal Processing*, May 2013, pp. 8614–8618, doi: 10.1109/ICASSP.2013.6639347.
- [51] Z. Zhang and M. R. Sabuncu, “Generalized cross entropy loss for training deep neural networks with noisy labels,” in *the 32nd International Conference on Neural Information Processing Systems*, Montréal, Canada, Dec. 2018, pp. 8792–8802, Accessed: Feb. 23, 2020. [Online].
- [52] R. R. Selvaraju, M. Cogswell, A. Das, R. Vedantam, D. Parikh, and D. Batra, “Grad-CAM: Visual Explanations from Deep Networks via Gradient-based Localization,” *Int. J. Comput. Vis.*, vol. 128, no. 2, pp. 336–359, Feb. 2020, doi: 10.1007/s11263-019-01228-7.

- [53] A. Kr. Jalan and A. R. Mohanty, "Model based fault diagnosis of a rotor-bearing system for misalignment and unbalance under steady-state condition," *Journal of Sound and Vibration*, vol. 327, no. 3, pp. 604–622, Nov. 2009, doi: 10.1016/j.jsv.2009.07.014.
- [54] M. Yu and D. Wang, "Model-Based Health Monitoring for a Vehicle Steering System With Multiple Faults of Unknown Types," *IEEE Transactions on Industrial Electronics*, vol. 61, no. 7, pp. 3574–3586, Jul. 2014, doi: 10.1109/TIE.2013.2281159.
- [55] F. Piltan, A. E. Prosvirin, M. Sohaib, B. Saldivar, and J.-M. Kim, "An SVM-Based Neural Adaptive Variable Structure Observer for Fault Diagnosis and Fault-Tolerant Control of a Robot Manipulator," *Applied Sciences*, vol. 10, no. 4, Art. no. 4, Jan. 2020, doi: 10.3390/app10041344.
- [56] L. Frosini, C. Harlişca, and L. Szabó, "Induction Machine Bearing Fault Detection by Means of Statistical Processing of the Stray Flux Measurement," *IEEE Transactions on Industrial Electronics*, vol. 62, no. 3, pp. 1846–1854, Mar. 2015, doi: 10.1109/TIE.2014.2361115.
- [57] M. Kang, J. Kim, J. Kim, A. C. C. Tan, E. Y. Kim, and B. Choi, "Reliable Fault Diagnosis for Low-Speed Bearings Using Individually Trained Support Vector Machines With Kernel Discriminative Feature Analysis," *IEEE Transactions on Power Electronics*, vol. 30, no. 5, pp. 2786–2797, May 2015, doi: 10.1109/TPEL.2014.2358494.
- [58] M. M. Manjurul Islam and J.-M. Kim, "Reliable multiple combined fault diagnosis of bearings using heterogeneous feature models and multiclass support vector Machines," *Reliability Engineering & System Safety*, vol. 184, pp. 55–66, Apr. 2019, doi: 10.1016/j.res.2018.02.012.
- [59] B. P. Duong and J.-M. Kim, "Non-Mutually Exclusive Deep Neural Network Classifier for Combined Modes of Bearing Fault Diagnosis," *Sensors*, vol. 18, no. 4, Art. no. 4, Apr. 2018, doi: 10.3390/s18041129.
- [60] N. Tandon and A. Choudhury, "A review of vibration and acoustic measurement methods for the detection of defects in rolling element bearings," *Tribology International*, vol. 32, no. 8, pp. 469–480, Aug. 1999, doi: 10.1016/S0301-679X(99)00077-8.
- [61] J. Xie, R. Girshick, and A. Farhadi, "Unsupervised Deep Embedding for Clustering Analysis," *Proceedings of The 33rd International Conference on Machine Learning*, vol. 48, pp. 478–487, May 2016.
- [62] L. Wen, X. Li, L. Gao, and Y. Zhang, "A New Convolutional Neural Network-Based Data-Driven Fault Diagnosis Method," *IEEE Transactions on Industrial Electronics*, vol. 65, no. 7, pp. 5990–5998, Jul. 2018, doi: 10.1109/TIE.2017.2774777.
- [63] L. Guo, Y. Lei, S. Xing, T. Yan, and N. Li, "Deep Convolutional Transfer Learning Network: A New Method for Intelligent Fault Diagnosis of Machines With Unlabeled Data," *IEEE Transactions on Industrial Electronics*, vol. 66, no. 9, pp. 7316–7325, Sep. 2019, doi: 10.1109/TIE.2018.2877090.
- [64] M. J. Hasan and J.-M. Kim, "Bearing Fault Diagnosis under Variable Rotational Speeds Using Stockwell Transform-Based Vibration Imaging and Transfer Learning," *Applied Sciences*, vol. 8, no. 12, Art. no. 12, Dec. 2018, doi: 10.3390/app8122357.
- [65] M. Sohaib and J. Kim, "Fault Diagnosis of Rotary Machine Bearings Under Inconsistent Working Conditions," *IEEE Transactions on Instrumentation and Measurement*, vol. 69, no. 6, pp. 3334–3347, Jun. 2020, doi: 10.1109/TIM.2019.2933342.

- [66] R. B. Randall and J. Antoni, "Rolling element bearing diagnostics—A tutorial," *Mechanical Systems and Signal Processing*, vol. 25, no. 2, pp. 485–520, Feb. 2011, doi: 10.1016/j.ymssp.2010.07.017.
- [67] S. Khan and J. Kim, "Automated Bearing Fault Diagnosis Using 2D Analysis of Vibration Acceleration Signals under Variable Speed Conditions," *Shock and Vibration*, vol. 2016, Dec. 2016, doi: 10.1155/2016/8729572.
- [68] Y. Lecun, L. Bottou, Y. Bengio, and P. Haffner, "Gradient-based learning applied to document recognition," *Proceedings of the IEEE*, vol. 86, no. 11, pp. 2278–2324, Nov. 1998, doi: 10.1109/5.726791.
- [69] J. Redmon, S. Divvala, R. Girshick, and A. Farhadi, "You Only Look Once: Unified, Real-Time Object Detection," in *2016 IEEE Conference on Computer Vision and Pattern Recognition (CVPR)*, Jun. 2016, pp. 779–788, doi: 10.1109/CVPR.2016.91.
- [70] B. P. Duong, J. Kim, C.-H. Kim, and J.-M. Kim, "Deep Learning Object-Impulse Detection for Enhancing Leakage Detection of a Boiler Tube Using Acoustic Emission Signal," *Applied Sciences*, vol. 9, no. 20, Art. no. 20, Jan. 2019, doi: 10.3390/app9204368.
- [71] "NI-9223 - National Instruments." <https://www.ni.com/en-ca/support/model.ni-9223.html> (accessed Dec. 02, 2020).
- [72] "R15I-AST - 150 kHz Integral Preamp AE Sensor." <https://www.physicalacoustics.com/by-product/sensors/R15I-AST-150-kHz-Integral-Preamp-AE-Sensor> (accessed Dec. 02, 2020).
- [73] "PCB Model 622B01." [https://www.pcb.com/products?model=622B01&item\\_id=Products&m=052BR030BZ](https://www.pcb.com/products?model=622B01&item_id=Products&m=052BR030BZ) (accessed Dec. 02, 2020).
- [74] E. C. C. Lau and H. W. Ngan, "Detection of Motor Bearing Outer Raceway Defect by Wavelet Packet Transformed Motor Current Signature Analysis," *IEEE Transactions on Instrumentation and Measurement*, vol. 59, no. 10, pp. 2683–2690, Oct. 2010.
- [75] R. Nishat Toma and J.-M. Kim, "Bearing Fault Classification of Induction Motors Using Discrete Wavelet Transform and Ensemble Machine Learning Algorithms," *Applied Sciences*, vol. 10, no. 15, Art. no. 15, Jan. 2020.
- [76] Z. Gao, C. Cecati, and S. X. Ding, "A Survey of Fault Diagnosis and Fault-Tolerant Techniques—Part I: Fault Diagnosis With Model-Based and Signal-Based Approaches," *IEEE Transactions on Industrial Electronics*, vol. 62, no. 6, pp. 3757–3767, Jun. 2015.
- [77] Z. Gao, C. Cecati, and S. X. Ding, "A Survey of Fault Diagnosis and Fault-Tolerant Techniques—Part II: Fault Diagnosis With Knowledge-Based and Hybrid/Active Approaches," *IEEE Transactions on Industrial Electronics*, vol. 62, no. 6, pp. 3768–3774, Jun. 2015.
- [78] A. E. Prosvirin, F. Piltan, and J.-M. Kim, "Hybrid Rubbing Fault Identification Using a Deep Learning-Based Observation Technique," *IEEE Transactions on Neural Networks and Learning Systems*, pp. 1–12, 2020.
- [79] F. Piltan and J.-M. Kim, "Bearing Fault Diagnosis Using an Extended Variable Structure Feedback Linearization Observer," *Sensors*, vol. 18, no. 12, Art. no. 12, Dec. 2018.
- [80] F. Piltan, A. E. Prosvirin, I. Jeong, K. Im, and J.-M. Kim, "Rolling-Element Bearing Fault Diagnosis Using Advanced Machine Learning-Based Observer," *Applied Sciences*, vol. 9, no. 24, Art. no. 24, Jan. 2019.

- [81] M. Kang, J. Kim, L. M. Wills, and J.-M. Kim, "Time-Varying and Multiresolution Envelope Analysis and Discriminative Feature Analysis for Bearing Fault Diagnosis," *IEEE Transactions on Industrial Electronics*, vol. 62, no. 12, pp. 7749–7761, Dec. 2015.
- [82] M. M. Manjurul Islam and J.-M. Kim, "Reliable multiple combined fault diagnosis of bearings using heterogeneous feature models and multiclass support vector Machines," *Reliability Engineering & System Safety*, vol. 184, pp. 55–66, Apr. 2019.
- [83] V. T. Do and U.-P. Chong, "Signal Model-Based Fault Detection and Diagnosis for Induction Motors Using Features of Vibration Signal in Two- Dimension Domain," *Journal of Mechanical Engineering*, vol. 57, no. 9, pp. 655–666, Jul. 2011.
- [84] L. Wen, X. Li, L. Gao, and Y. Zhang, "A New Convolutional Neural Network-Based Data-Driven Fault Diagnosis Method," *IEEE Transactions on Industrial Electronics*, vol. 65, no. 7, pp. 5990–5998, Jul. 2018.
- [85] V. Tra, S. A. Khan, and J.-M. Kim, "Diagnosis of bearing defects under variable speed conditions using energy distribution maps of acoustic emission spectra and convolutional neural networks," *The Journal of the Acoustical Society of America*, vol. 144, no. 4, pp. EL322–EL327, Oct. 2018.
- [86] M. Sohaib and J.-M. Kim, "Fault Diagnosis of Rotary Machine Bearings Under Inconsistent Working Conditions," *IEEE Transactions on Instrumentation and Measurement*, vol. 69, no. 6, pp. 3334–3347, Jun. 2020.
- [87] M. J. Hasan and J.-M. Kim, "Bearing Fault Diagnosis under Variable Rotational Speeds Using Stockwell Transform-Based Vibration Imaging and Transfer Learning," *Applied Sciences*, vol. 8, no. 12, Art. no. 12, Dec. 2018.
- [88] J. Cai and Y. Xiao, "Time-frequency analysis method of bearing fault diagnosis based on the generalized S transformation," *Journal of Vibroengineering*, vol. 19, no. 6, pp. 4221–4230, 2017.
- [89] M. T. Pham, J.-M. Kim, and C. H. Kim, "Accurate Bearing Fault Diagnosis under Variable Shaft Speed using Convolutional Neural Networks and Vibration Spectrogram," *Applied Sciences*, vol. 10, no. 18, Art. no. 18, Jan. 2020.
- [90] W. Huang, G. Gao, N. Li, X. Jiang, and Z. Zhu, "Time-Frequency Squeezing and Generalized Demodulation Combined for Variable Speed Bearing Fault Diagnosis," *IEEE Transactions on Instrumentation and Measurement*, vol. 68, no. 8, pp. 2819–2829, Aug. 2019.
- [91] P. W. Tse, W. Yang, and H. Y. Tam, "Machine fault diagnosis through an effective exact wavelet analysis," *Journal of Sound and Vibration*, vol. 277, no. 4, pp. 1005–1024, Nov. 2004.
- [92] N. Bessous, S. E. Zouzou, W. Bentrach, S. Sbaa, and M. Sahraoui, "Diagnosis of bearing defects in induction motors using discrete wavelet transform," *Int J Syst Assur Eng Manag*, vol. 9, no. 2, pp. 335–343, Apr. 2018.
- [93] X. Zhang, Z. Liu, J. Wang, and J. Wang, "Time–frequency analysis for bearing fault diagnosis using multiple Q-factor Gabor wavelets," *ISA Transactions*, vol. 87, pp. 225–234, Apr. 2019.
- [94] R. B. Randall and J. Antoni, "Rolling element bearing diagnostics—A tutorial," *Mechanical Systems and Signal Processing*, vol. 25, no. 2, pp. 485–520, Feb. 2011.
- [95] J. Ben Ali, N. Fnaiech, L. Saidi, B. Chebel-Morello, and F. Fnaiech, "Application of empirical mode decomposition and artificial neural network for automatic bearing fault diagnosis based on vibration signals," *Applied Acoustics*, vol. 89, pp. 16–27, Mar. 2015.

- [96] O. Janssens *et al.*, “Convolutional Neural Network Based Fault Detection for Rotating Machinery,” *Journal of Sound and Vibration*, vol. 377, pp. 331–345, Sep. 2016.
- [97] B. P. Duong and J.-M. Kim, “Non-Mutually Exclusive Deep Neural Network Classifier for Combined Modes of Bearing Fault Diagnosis,” *Sensors*, vol. 18, no. 4, Art. no. 4, Apr. 2018.
- [98] D. Wang, Q. Miao, X. Fan, and H.-Z. Huang, “Rolling element bearing fault detection using an improved combination of Hilbert and wavelet transforms,” *J Mech Sci Technol*, vol. 23, no. 12, pp. 3292–3301, Dec. 2009, doi: 10.1007/s12206-009-0807-4.
- [99] M. Kang, J. Kim, and J. Kim, “High-Performance and Energy-Efficient Fault Diagnosis Using Effective Envelope Analysis and Denoising on a General-Purpose Graphics Processing Unit,” *IEEE Transactions on Power Electronics*, vol. 30, no. 5, pp. 2763–2776, May 2015, doi: 10.1109/TPEL.2014.2356207.
- [100] T. Ojala, M. Pietikainen, and T. Maenpaa, “Multiresolution gray-scale and rotation invariant texture classification with local binary patterns,” *IEEE Transactions on Pattern Analysis and Machine Intelligence*, vol. 24, no. 7, pp. 971–987, Jul. 2002.
- [101] A. Brandt, K. Ahlin, and T. Lagö, “Noise and vibration measurement system basics,” *Sound and Vibration*, vol. 40, no. 4, pp. 9–11, Apr. 2006.
- [102] ISO/TC 108, S, “Condition monitoring and diagnosis of machines—Acoustic emission.” ISO 22096:2007(E), 2007.
- [103] M. Kang, J. Kim, B.-K. Choi, and J.-M. Kim, “Envelope analysis with a genetic algorithm-based adaptive filter bank for bearing fault detection,” *The Journal of the Acoustical Society of America*, vol. 138, no. 1, pp. EL65–EL70, Jul. 2015, doi: 10.1121/1.4922767.
- [104] S. A. Khan and J.-M. Kim, “Rotational speed invariant fault diagnosis in bearings using vibration signal imaging and local binary patterns,” *The Journal of the Acoustical Society of America*, vol. 139, no. 4, pp. EL100–EL104, Apr. 2016, doi: 10.1121/1.4945818.
- [105] H. Yang, H. Jiang, Z. Yang, and J. Li, “Fault Diagnosis of Rolling Bearing Based on Wavelet Packet Transform and Support Vector Machine,” in *IEEE International Conference and Measuring Technology and Mechatronics Automation*, Apr. 2009, pp. 650–653, doi: 10.1109/ICMTMA.2009.331.
- [106] B. Liu and H. Pan, “Fault diagnosis of bearing using wavelet packet transform and PSO-DV based neural network,” in *2010 Sixth International Conference on Natural Computation*, Aug. 2010, vol. 3, pp. 1238–1242, doi: 10.1109/ICNC.2010.5583628.
- [107] Haodong Ma, Yi Xiong, Hongzheng Fang, and Lichao Gu, “Fault diagnosis of bearing based on fuzzy support vector machine,” in *2015 Prognostics and System Health Management Conference (PHM)*, Oct. 2015, pp. 1–4, doi: 10.1109/PHM.2015.7380059.
- [108] S. Avidan, “Support vector tracking,” *IEEE Transactions on Pattern Analysis and Machine Intelligence*, vol. 26, no. 8, pp. 1064–1072, Aug. 2004, doi: 10.1109/TPAMI.2004.53.
- [109] H. Liu, “On the Levenberg-Marquardt training method for feed-forward neural networks,” in *2010 Sixth International Conference on Natural Computation*, Aug. 2010, vol. 1, pp. 456–460, doi: 10.1109/ICNC.2010.5583151.
- [110] K. Hagiwara, “Regularization learning, early stopping and biased estimator,” *Neurocomputing*, vol. 48, no. 1, pp. 937–955, Oct. 2002, doi: 10.1016/S0925-2312(01)00681-6.

- [111] R. Isermann, "Supervision, fault-detection and fault-diagnosis methods — An introduction," *Control Engineering Practice*, vol. 5, no. 5, pp. 639–652, May 1997, doi: 10.1016/S0967-0661(97)00046-4.
- [112] R. Isermann, *Fault-Diagnosis Systems: An Introduction from Fault Detection to Fault Tolerance*. Berlin Heidelberg: Springer-Verlag, 2006.
- [113] F. Kimmich, A. Schwarte, and R. Isermann, "Fault detection for modern Diesel engines using signal- and process model-based methods," *Control Engineering Practice*, vol. 13, no. 2, pp. 189–203, Feb. 2005, doi: 10.1016/j.conengprac.2004.03.002.
- [114] A. Schwarte, F. Kimmich, and R. Isermann, "Model-based fault detection of a diesel engine with turbo charger - a case study," *IFAC Proceedings Volumes*, vol. 36, no. 5, pp. 293–306, Jun. 2003, doi: 10.1016/S1474-6670(17)36508-4.
- [115] R. Isermann, "Process fault detection based on modeling and estimation methods—A survey," *Automatica*, vol. 20, no. 4, pp. 387–404, Jul. 1984, doi: 10.1016/0005-1098(84)90098-0.
- [116] A. K. S. Jardine, D. Lin, and D. Banjevic, "A review on machinery diagnostics and prognostics implementing condition-based maintenance," *Mechanical Systems and Signal Processing*, vol. 20, no. 7, pp. 1483–1510, Oct. 2006, doi: 10.1016/j.ymssp.2005.09.012.
- [117] M. E. H. Benbouzid, "A review of induction motors signature analysis as a medium for faults detection," *IEEE Transactions on Industrial Electronics*, vol. 47, no. 5, pp. 984–993, Oct. 2000, doi: 10.1109/41.873206.
- [118] S. A. McInerny and Y. Dai, "Basic vibration signal processing for bearing fault detection," *IEEE Transactions on Education*, vol. 46, no. 1, pp. 149–156, Feb. 2003, doi: 10.1109/TE.2002.808234.
- [119] F. Li, G. Meng, L. Ye, and P. Chen, "Wavelet Transform-based Higher-order Statistics for Fault Diagnosis in Rolling Element Bearings," *Journal of Vibration and Control - J VIB CONTROL*, vol. 14, pp. 1691–1709, Nov. 2008, doi: 10.1177/1077546308091214.
- [120] A. Widodo, B.-S. Yang, and T. Han, "Combination of independent component analysis and support vector machines for intelligent faults diagnosis of induction motors," *Expert Systems with Applications*, vol. 32, no. 2, pp. 299–312, Feb. 2007, doi: 10.1016/j.eswa.2005.11.031.
- [121] Y. Lei, Z. He, and Y. Zi, "Application of an intelligent classification method to mechanical fault diagnosis," *Expert Systems with Applications*, vol. 36, no. 6, pp. 9941–9948, Aug. 2009, doi: 10.1016/j.eswa.2009.01.065.
- [122] B. Samanta, K. R. Al-Balushi, and S. A. Al-Araimi, "Artificial neural networks and support vector machines with genetic algorithm for bearing fault detection," *Engineering Applications of Artificial Intelligence*, vol. 16, no. 7, pp. 657–665, Oct. 2003, doi: 10.1016/j.engappai.2003.09.006.
- [123] M. D. Prieto, G. Cirrincione, A. G. Espinosa, J. A. Ortega, and H. Henao, "Bearing Fault Detection by a Novel Condition-Monitoring Scheme Based on Statistical-Time Features and Neural Networks," *IEEE Transactions on Industrial Electronics*, vol. 60, no. 8, pp. 3398–3407, Aug. 2013, doi: 10.1109/TIE.2012.2219838.
- [124] P. E. William and M. W. Hoffman, "Identification of bearing faults using time domain zero-crossings," *Mechanical Systems and Signal Processing*, vol. 25, no. 8, pp. 3078–3088, Nov. 2011, doi: 10.1016/j.ymssp.2011.06.001.

- [125] X. Wang, U. Kruger, G. W. Irwin, G. McCullough, and N. McDowell, "Nonlinear PCA With the Local Approach for Diesel Engine Fault Detection and Diagnosis," *IEEE Transactions on Control Systems Technology*, vol. 16, no. 1, pp. 122–129, Jan. 2008, doi: 10.1109/TCST.2007.899744.
- [126] P. Baranyi, Yeung Yam, A. R. Varkonyi-Koczy, and R. J. Patton, "SVD-based reduction to MISO TS models," *IEEE Transactions on Industrial Electronics*, vol. 50, no. 1, pp. 232–242, Feb. 2003, doi: 10.1109/TIE.2002.807673.
- [127] C. Prompubess, L. Mekasut, P. Piumsomboon, and P. Kuchontara, "Co-combustion of coal and biomass in a circulating fluidized bed combustor," *Korean J. Chem. Eng.*, vol. 24, no. 6, pp. 989–995, Nov. 2007, doi: 10.1007/s11814-007-0109-4.
- [128] T.-W. Kim *et al.*, "Tube Erosion Rate of Water Wall in a Commercial Circulating Fluidized Bed Combustor," *Korean Chemical Engineering Research*, vol. 43, no. 4, pp. 525–530, 2005.